TECHNISCHE UNIVERSITÄT WIEN

DIPLOMARBEIT

Design of Metal-Organic Frameworks containing Single-Metal-Site Cocatalysts for Photocatalytic Hydrogen Production

Ausgeführt am Institut für
Materialchemie
der Technischen Universität Wien

unter der Anleitung von
Univ.Prof. Mag.rer.nat. Dr.rer.nat. Dominik Eder
und
Assistant Prof. Dr.rer.nat. Alexey Cherevan

durch

Adrian Ertl, BSc

03.07.2023
Datum

[redacted]
Unterschrift

Abstract

The reliance of global energy production on fossil fuels leads to drastic changes in the world´s climate. Renewable energy derived from natural sources like sunlight or wind is abundantly available, but its intermittent nature requires new solutions for storing this energy. Hydrogen represents an interesting option as a sustainable energy carrier that can be generated from water upon irradiation with sunlight by means of photocatalysis. However, current photocatalytic systems do not meet the requirements for scalable hydrogen production, with heterogeneous systems lacking activity and selectivity and homogeneous catalysts degrading quickly under reaction conditions. The incorporation of single-metal sites onto heterogeneous support materials has the possibility to bridge the two concepts, creating catalysts with well-defined active sites and maximum atom utilization efficiency. Metal-organic frameworks (MOFs) are an ideal platform for integrating such single sites due to their large surface area and high structural tunability.

In this thesis, single-site cocatalysts were introduced into the MOF systems UiO-67 and COK-47 as organometallic complexes containing noble Pt or earth-abundant Ni that also function as MOF linkers. Two synthesis strategies were used to obtain such single-site-functionalized MOFs: direct one-pot synthesis where the functionalization occurs during the MOF synthesis and post-synthetic ligand exchange. The obtained materials were characterized carefully and their activity for photocatalytic hydrogen production was evaluated. Pt or Ni single-metal sites on UiO-67 showed excellent photocatalytic performances for already very low metal loadings below 0.5 wt-% and they were more active than their nanoparticle counterparts obtained by photodeposition. In contrast to this, the functionalization of COK-47 with Ni sites resulted in almost no photocatalytic activity and while Pt single sites on COK-47 did produce hydrogen, the performance was considerably worse than with Pt nanoparticles, highlighting that the concept of functionalization with single-site cocatalysts works better for UiO-67 than for COK-47. Compared to one-pot synthesis, ligand exchange increased flexibility for the synthesis and enabled more MOF-cocatalyst combinations. However, the ligand exchange procedure most likely introduced missing ligand defects in the MOF structure and electron trap states close to the conduction band which resulted in a decreased catalytic activity. This work highlights the importance of single-metal sites as cocatalyst in photocatalysis and also shows the strong influence of different implementation strategies, providing ground for future research.

Table of Contents

1 Abbreviations 1

2 Introduction 2

2.1 Global Energy Crisis 2

2.2 Photocatalysis 2

2.2.1 Heterogeneous Photocatalysis 2

2.2.1.1 Basics of Photocatalytic Water Splitting 3

2.2.1.2 Photocatalysts Based on Oxide Materials 5

2.2.1.3 Non-Oxide Photocatalysts 5

2.2.2 Homogeneous Photocatalysis 6

2.2.3 Bridging Homogeneous and Heterogeneous Catalysis 8

2.2.3.1 Comparison of the two Branches 8

2.2.3.2 Single-Site Photocatalysis 8

2.3 Metal-Organic Frameworks (MOFs) 9

2.3.1 MOFs as a Platform for Single-Site Photocatalysts 10

2.3.2 MOF Model Systems for Single-Site Photocatalysis 11

2.3.2.1 Zr-based MOFs 11

2.3.2.2 Ti-based MOFs 13

2.4 Synthesis Strategies for MOF-based Single-Site Catalysts 14

2.4.1 Post-Synthetic Metalation 15

2.4.2 One-Pot Synthesis 17

2.4.3 Post-Synthetic Ligand Exchange 18

3 Motivation and Aims 20

4 Materials and Methods 21

4.1 List of Chemicals 21

4.2 Characterization Methods 22

5 Experimental Part 25

5.1 Synthesis Procedures 25

5.1.1 Organometallic Complexes 25

5.1.1.1 [Pt(H_2bpydc)Cl_2] ... 25
5.1.1.2 [Ni(H_2bpydc)Cl_2] ... 25
5.1.2 MOF synthesis ... 25
5.1.2.1 UiO-67: One-Pot Synthesis and non-functionalized MOFs ... 25
5.1.2.2 COK-47: One-Pot Synthesis and non-functionalized MOFs ... 26
5.1.2.3 COK-47$_S$ ... 26
5.1.2.4 Post-Synthetic Ligand Exchange of UiO-67, COK-47 and COK-47$_S$ ... 26
5.2 Evaluation of the Photocatalytic Activity ... 27
6 Results and Discussion ... 28
6.1 Organometallic Complexes ... 28
6.2 UiO-67-based MOFs ... 35
6.2.1 Influence of the Cocatalyst ... 35
6.2.2 Influence of the Synthesis Method ... 42
6.3 COK-47-based MOFs ... 47
6.3.1 One-Pot Synthesis ... 48
6.3.2 Post-Synthetic Ligand Exchange ... 53
6.3.2.1 Post-Synthetic Ligand Exchange with Porous COK-47 ... 55
7 Conclusions ... 57
8 Outlook ... 59
9 List of References ... 60
Acknowledgements ... 66

1 Abbreviations

ATR ..... attenuated total reflectance
bdc benzene-1,4-dicarboxylate
bpdc ..... 4,4'-biphenyldicarboxylate
bpy ..... 2,2'-bipyridine
bpydc ..... 2,2'-bipyridine-5,5'-dicarboxylate
DMF ..... N,N-dimethylformamide
DMSO ..... dimethyl sulfoxide
DRS ..... diffuse reflectance spectroscopy
FTIR ..... fourier-transform infrared spectroscopy
GC ..... gas chromatography
HER ..... hydrogen evolution reaction
HOMO ..... highest occupied molecular orbital
LED ..... light-emitting diode
LUMO ..... lowest uncopied molecular orbital
M ..... metal (general) or mol/L
Me ..... methyl group
MOF ..... metal-organic framework
NHE ..... normal hydrogen electrode
NMR ..... nuclear magnetic resonance spectroscopy
OER ..... oxygen evolution reaction
PL ..... photoluminescence spectroscopy
ppy 2-phenylpyridine
PS ..... photosensitizer
PSM ..... post-synthetic metalation
SBU ..... secondary building unit
TGA ..... thermogravimetric analysis
TXRF ..... total-reflection x-ray fluorescence spectroscopy
UV ..... ultraviolet radiation
Vis ..... visible light
XPS ..... x-ray photoelectron spectroscopy
XRD ..... x-ray diffraction

2 Introduction

2.1 Global Energy Crisis

Climate change is one of the main issues our society is facing today. In the Paris Agreement from 2015, 196 parties agreed to limit global warming to less than 2°C compared to pre-industrial levels, ideally even 1.5°C.[1] The average global temperature has already increased by 1°C, so quick and efficient solutions are necessary. Climate change is mainly caused by CO_2 emissions, to which burning of fossil fuels represents a primary player. What makes the issue even more difficult is an increasing energy demand which is progressing faster than the decarbonization of energy production.[2] Solar energy constitutes an abundant renewable energy source, as the sun provides almost $4 \cdot 10^{24}$ J of energy per year, of which approximately $5 \cdot 10^{22}$ J are considered easily harvestable, which is, in theory, more than enough to satisfy humanity´s demands. One issue with solar energy is its fluctuating availability depending on time and season.[3] Therefore, the development of emission free energy carriers is essential. Hydrogen offers an exciting and efficient alternative to conventional fuels, as its combustion only produces water, and it can be obtained renewably from water by electrolysis. However, electrolysis requires a high energy input to split water.[4] Today, hydrogen is mainly produced by steam reforming of natural gas, which again produces high emissions of CO_2.[5] An important scientific breakthrough were the experiments of Fujishima and Honda, where they reported the photoelectrochemical splitting of water under visible light irradiation. The use of the light´s energy can significantly reduce the required bias voltage, which is 1.23 V for the electrolysis of water.[6] Besides photoelectrocatalysis and a combination of photovoltaics and electrolysis, photocatalysis is another method for using solar energy for hydrogen production from water. Of these techniques, photocatalysis stands out as the one with the lowest complexity, as only the photocatalyst dispersed in water, a source of light and a system for separating the formed oxygen and hydrogen are required.[7]

2.2 Photocatalysis

2.2.1 Heterogeneous Photocatalysis

Heterogeneous catalysis is one of the two main branches of catalysis. Its definition is that the catalyst is not in the same phase as reactants and products. In heterogeneous photocatalysis, solid semiconductors are used as catalyst. When irradiated with light of a wavelength smaller than the band gap of the semiconductor, a photon is absorbed which leads to the excitation of an electron from the valence band to the conduction band of the semiconductor. This creates a negatively charged electron and a positively charged electron hole as charge carriers. When these charge carriers are separated, they can migrate to the catalyst surface. Species that are adsorbed on the surface can then be reduced or oxidized by the electrons or

holes, respectively.[8–10] Applications of heterogeneous catalysis are for example water treatment and air purification, also for low concentration of pollutants. Another possible prominent application is photocatalytic water splitting. Different reaction setups are possible. On a laboratory scale, the photocatalyst is often dispersed in a liquid. However, for industrial scale applications, it is desirable to immobilize the catalyst on a support material, as this does not require energy intensive dispersing and enables elaborate light harvesting techniques by following the movement of the sun.[10,11] The potential scalability of photocatalytic water splitting was demonstrated by Nishiyama et al. in 2021, when they reported a 100 m^2 large array of reactors containing photocatalyst sheets that was operated for several months.[12] In the following chapters, the basics of photocatalytic water splitting and material requirements for such catalysts will be discussed.

2.2.1.1 Basics of Photocatalytic Water Splitting

Water splitting is a thermodynamically unfavorable reaction, exhibiting a Gibbs free energy of around +237 kJ/mol. It can be divided into two half-reactions, the hydrogen evolution reaction (HER) and the oxygen evolution reaction (OER):

$$2\,H^+ + 2\,e^- \rightarrow H_2 \qquad \text{HER} \qquad (1)$$

$$H_2O \rightarrow \frac{1}{2}\,O_2 + 2\,H^+ + 2\,e^- \qquad \text{OER} \qquad (2)$$

In order to accomplish photocatalytic water splitting, the band gap of the semiconductor needs to encompass both the oxidation and the reduction potential of water, which lie at 1.23 V and 0 V vs the normal hydrogen electrode (NHE) at pH 0. Therefore, the minimum band gap is 1.23 eV when neglecting additional overpotentials for enhancing the reaction kinetics. This would correspond to electromagnetic radiation with a wavelength of approximately 1000 nm, which is already in the near-infrared region. Small band gaps are preferred to absorb a high portion of the solar spectrum, but too narrow band gaps are detrimental for the process as well as they limit the reaction pace. Difficulties in actually achieving even visible-light-active photocatalysts for water splitting will be discussed in the next chapter. A scheme of the processes behind photocatalytic water splitting can be seen in Figure 1. After absorption of a photon, the formed charge carriers need to be separated without recombining or being trapped. One phenomenon that can facilitate charge separation is band bending which occurs when the semiconductor is immersed into a solution due to the alignment of the fermi level of the semiconductor and the redox potential of the solution at the interface by electron transfer between the two. The resulting electric field can facilitate separation of the charge carriers after excitation. This effect is especially important for semiconductor electrodes and less for nanoparticles because the space charge region can be larger than the nanoparticle itself,

nevertheless it can still have an important influence on charge separation within a single nanoparticle.[9] High crystallinity is desired for successful charge migration to the surface as this reduces the number of recombination sites. Small nanoparticles can be beneficial because they exhibit a shorter migration path for the charge carriers to the surface.[8] The final step of photocatalytic water splitting are the redox reactions on the surface. HER requires a two-electron transfer process, whereas OER requires a four-electron transfer process. Therefore, OER is generally considered to be the bottleneck of water splitting,[13] despite the fact that many pure oxide semiconductors are less active for photocatalytic hydrogen evolution than oxygen evolution.[9]

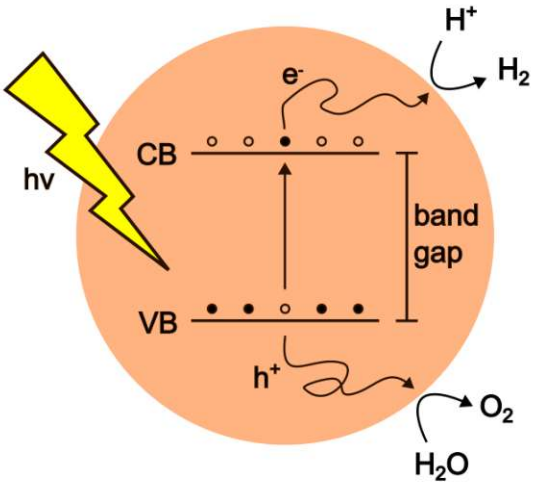

Figure 1: Fundamental steps of photocatalytic water splitting

One way to optimize the catalytic reactions on the surface is the addition of cocatalysts. These show a lower activation barrier for the corresponding reaction and consequently decrease the required overpotentials to drive the reaction. Besides the improved kinetics, the introduction of a cocatalyst also leads to an electrical field due to the formed Schottky or p-n junction at the interface for metal or semiconductor cocatalysts, respectively. This electrical field can enhance charge carrier separation. In some cases, even better light absorption can be obtained due to a plasmonic enhancement effect.[8] On the other hand, a cocatalyst can sometimes also show unwanted side effects like trapping of charge carriers at the interface.[8] Common cocatalysts for hydrogen evolution are metals like Pt, Rh, Ru, Ir and Ni. For oxygen evolution, oxides of Co, Fe, Ni, Mn, Ru and Ir are often used. HER cocatalysts are usually necessary to achieve efficient water splitting, while OER cocatalysts alone have a smaller effect on the overall catalytic activity. Best results can be obtained by introducing both types of cocatalysts. It should be noted that cocatalysts can not only catalyze the desired reaction, but can also promote the backward reaction, namely water formation. This can be addressed by using bimetallic promoters.[10]

2.2.1.2 *Photocatalysts Based on Oxide Materials*

Semiconductor oxides like TiO_2 are the most typical photocatalysts used for water splitting. This is mainly attributed to their high stability under both oxidative and reductive conditions. Unfortunately, the frequently used oxides have a large band gap which prevents efficient utilization of the solar spectrum, but oxides with a smaller band gap like WO_3, $BiVO_4$ and Fe_2O_3 are not active for water splitting, due to unsuitable band positions.[10] This can be explained by looking at the composition of the conduction and the valence band. The conduction band of oxide semiconductors mainly consists of empty d orbitals in the case of d^0 transition metal-based semiconductors or sp hybridized orbitals for d^{10} metal semiconductors. The position of the conduction band can thus be tuned by changing the metal cation and it is too low in the case of narrow band gap oxides like WO_3. The valence band is mainly made up of oxygen 2p orbitals and is therefore more or less fixed at a reduction potential of around +3 V vs NHE (at pH 0). This is a lot deeper than it would be needed for OER which explains the large band gap needed to achieve overall water splitting on an oxide-based photocatalyst.[9]

One possibility to achieve visible light photoactivity is the so-called Z-scheme, which is inspired by photosynthesis in plants. Here, two photocatalysts are used, one for the oxidation reaction and the other for the reduction reaction. The two catalysts are connected by a redox mediator, of which the oxidized form gets reduced on the oxidation catalyst and the reduced form oxidized on the reduction catalyst. This setup leads to a two-step photoexcitation, whereby each step requires absorption of a photon with lower energy compared to a single photocatalyst. That enables the use of oxide semiconductors with narrow band gaps and a better utilization of the solar spectrum. However, it needs to be considered that two photons are required to generate a single electron-hole pair that can be used to conduct the water splitting reaction. Still, due to the low quantity of UV radiation in sunlight (around 4 %), Z-scheme photocatalysis can significantly enhance sunlight absorption and overall reaction quantum yields. In some cases, it was possible to perform the same process without the use of a redox mediator. Electron transfer then takes place via direct contact between the two photocatalysts.[9,10]

2.2.1.3 *Non-Oxide Photocatalysts*

As discussed in the previous chapter, the oxygen orbitals forming the valence band are limiting for visible-light-driven water splitting. This makes non-oxide semiconductors very interesting candidates for visible light activity. N 2p as well as S 3p orbitals form a valence band with a suitable position for visible light water splitting as it is higher than a valence band consisting of O 2p orbitals, but still low enough to drive water oxidation. Nitrides and oxynitrides, as well as sulfides and oxysulfides therefore have received increasing attention.[9] An illustrative example is the comparison of Ta_2O_5, TaON and Ta_3N_5. The conduction band lies at a similar

redox potential for all three semiconductors, between -0.3 V and -0.5 V vs NHE (at pH 0). The band gap, however decreases from 3.9 eV for Ta_2O_5 to 2.4 eV for TaON or 2.1 eV for Ta_3N_5, with the valence band stills staying below the +1.23 V necessary for water oxidation. These band gaps correspond to electromagnetic radiation of 520 or 600 nm, respectively, well within the region of visible light.[14] As a drawback, non-oxide semiconductors are usually catalytically less active for water splitting and less stable for oxidation than oxide photocatalysts.[9]

2.2.2 Homogeneous Photocatalysis

In homogeneous catalysis, the other main branch of catalysis, reactants and products are in the same phase as the catalyst, usually the liquid phase. Applications of homogeneous photocatalysis include wastewater treatment, gas purification as well as water splitting and CO_2 reduction. Excitation of a molecular photocatalyst with light leads to the transfer of an electron from the highest occupied molecular orbital (HOMO) to the lowest unoccupied molecular orbital (LUMO) in contrast to an excitation from the valence band to the conduction band in heterogeneous photocatalysts. The LUMO can then donate an electron to reduce a reactant, whereas the HOMO can accept an electron to drive an oxidation reaction.[15] In many instances, however, a photosensitizer (PS) is used to account for light absorption. In this case, an additional redox cycle is established between the PS and the molecular catalyst, which, after being reduced or oxidized by PS*, is able to drive the process of interest.

A prevalent group of compounds used for homogeneous photocatalytic water spitting are organometallic complexes. Here, the first fundamental step is the coordination of water, instead of surface adsorption of water as it is the case for heterogeneous photocatalysts. This requires sufficient thermodynamics, so strong bonds need to be formed. Possible modes of water coordination include a dative bond via the free electron pairs of oxygen, hydrogen bonding between another ligand and H of the water molecule, side-on coordination of water at the metal center, addition of H or OH ligands, formation of an ion pair or the oxidative addition of both H and OH ligands. The coordination via a free electron pair of oxygen represents the simplest coordination and also the most important one in water splitting. An early, prominent example where such coordination takes place is the so-called blue dimer, a μ-oxo-briged ruthenium(III) complex for water oxidation with the formula cis-cis-$[(bpy)_2(H_2O)Ru(\mu\text{-}O)Ru(H_2O)(bpy)_2]^{4+}$ (bpy = 2,2'-bipyridine).[16] The stability of such aqua complexes is heavily dependent on the other ligands present. Oxidative addition predominantly takes place at electron-deficient complexes. Most examples where oxidative addition is the water coordination mode are based on late transition metal complexes, especially iridium complexes like $[Ir(PMe_3)_4]$ or $[IrCl(PMe_3)_3]$.[16] The addition products are often very reactive in these cases. Reaction mechanisms for water splitting after the successful coordination of water vary from case to case. Intermediates during the catalytic cycle include

besides hydroxide and aqua complexes also metal-oxo and metal-peroxide species as well as oxyl radicals.[16]

A typical design for a homogeneous photocatayst is a combination of a water oxidation catalyst, a proton reduction catalyst and a photosensitizer. The components can be linked for example via covalent bonding or form supramolecular complexes.[16] In this three-species design, the photosensitizer absorbs light which leads to photoexcitation. The excited electron is transferred to the reduction catalyst and the photosensitizer receives an electron from the oxidation catalyst to fill the formed electron hole. A typical photosensitizer is the $[Ru(bpy)_3]^{2+}$ complex which shows visible light absorption centered at 450 nm. When irradiated with this wavelength, an electron is excited from a t_{2g} orbital of the metal to a π* orbital of a ligand. This process is called a metal-to-ligand charge transfer and results in the oxidation of Ru(II) to Ru(III) and the reduction of the ligand. The initial excited state of the complex undergoes intersystem crossing to a triplet state. This triplet state exhibits a long lifetime of around 1 µs due to the spin selection rule. The excited state can then be oxidized or reduced rather easily compared to the ground state.[17] For hydrogen evolution at the proton reduction catalyst, a two-electron process needs to take place. However, the photosensitizer can only offer one electron at a time. A possible solution is the disproportionation of the one-electron reduced catalyst to the original catalyst and a two-electron reduced species.[16] Examples of homogeneous catalysts for hydrogen evolution include Pt-complexes, but also complexes based on abundant elements like Ni or Co can be used. The water oxidation catalyst needs to be able to perform a four-electron process. An efficient catalytic reaction therefore requires special properties, like complexes based on metals with many possible oxidation states or the use of multinuclear complexes. An example for the first is presented by nature, namely by the oxygen-evolving complex (OEC) for photosynthesis in plants. The OEC includes a Mn_4Ca cluster where Mn can show oxidation states from +3 to +5.[16,17] For research purposes, Ru-complexes are prominent water oxidation catalysts because of their large range of possible oxidation states.[18] One important thing to consider when performing the water oxidation reaction with a homogeneous photocatalysis is whether the active species is actually a homogeneous one. In oxidizing conditions, complexes often tend to form metal oxides or hydroxides that can catalyze water oxidation as well. Elaborate spectroscopy techniques need to be employed to be sure about the nature of the active species. An early example of a working water oxidation catalyst is the aforementioned blue dimer, a dinuclear Ru(III) complex where high oxidation states are stabilized by electron coupling via the oxo-bridge. The structure allows for a concerted proton and electron transfer, called proton-coupled electron transfer (PCET), which enables the charge of the complex to remain unchanged.[17]

2.2.3 Bridging Homogeneous and Heterogeneous Catalysis

2.2.3.1 Comparison of the two Branches

Homogeneous catalysts generally show higher activity and selectivity than their heterogeneous counterparts. However, such catalysts are rather hard to recover, as they are in the same phase as the reactants and products, and are relatively unstable. Additionally, homogeneous catalysts are often expensive, toxic and based on scarce elements. Heterogeneous catalysts exhibit higher stability and can be separated easier and therefore have better recyclability, but they are lacking behind in activity, often due to low visible light absorption.[15] For industrial applications, heterogeneous catalysts are preferred because of their practicability, but the small number of active sites needs to be compensated by high temperatures and the lower selectivity leads to a large number of side products which hampers their economic profitability. An important drawback of heterogeneous catalysts for research is the difficulty to properly characterize and study them because of their less defined nature. This makes it hard to systematically develop better catalysts compared to homogeneous catalysts, whose structure and reaction mechanisms are better understood.[19] It is therefore desirable to find catalysts that combine both worlds and exhibit the high activity, selectivity and defined structure on an atomic scale of homogeneous catalysts and the stability and recyclability of heterogeneous ones. A prominent approach to achieve these properties is the design of single-site catalysts.

2.2.3.2 Single-Site Photocatalysis

Instead of using nanoparticles for facilitating charge separation and providing catalytically active surfaces, single-site photocatalysis relies on single metal atoms. This makes it possible to study and understand the catalyst on the atomic scale. Furthermore, such single-site catalysts provide more active centers, as potentially all metal atoms can be utilized, but also every active site has the potential to be more active due to different geometric and electronic properties of single metal atoms compared to nanoparticles. The electronic properties of small particles heavily depend on the exact number of atoms. A typical example is the oscillation of the work function of gold particles of less than 30 atoms when plotted against the number of atoms. A decrease in particle size also leads to an increase in the ratio of unsaturated surface atoms to bulk atoms, resulting in a changed catalytic reactivity.[20]

The surface energy of single metal atoms is very high. Accordingly, they tend to agglomerate to form nanoparticles. This makes stabilization of such particles necessary by immobilizing them on a support material. The interaction of the support and the single metal atoms is of high importance, as they mutually change the electronic properties of each other, which influences the adsorption of reactants and can reduce the activation barrier for the catalytic reaction. Another difference between nanoparticles and single metal atoms on a support is

that the latter are usually charged.[20] It was shown that photocatalytic reactions can be enhanced by introducing single-site cocatalysts. As an example, single Pt atoms on TiO_2 showed activity 6-13 times higher than larger Pt particles.[21]

Strategies for obtaining single-site catalysts include physical procedures like atomic layer deposition (ALD), chemical techniques like impregnation and co-precipitation, and other methods like pyrolysis of precursors. Surface defects or functional groups on the surface of the support can act as binding sites for stabilization of the single metal atoms. An interesting class of materials that is also labeled single-site catalysts involves organometallic complexes anchored on a support surface.[22] In addition, they can be immobilized within porous materials like zeolites, mesoporous silica or metal-organic frameworks (MOFs). Anchoring to the surface can take place via chemical bonding, for example when functional groups on the support surface act as ligands, or via spatial confinement, among others.[23] Considering the special nature of MOFs as organic-inorganic hybrids and their unique properties, the following chapter will explore MOFs as a platform for single-site photocatalysis.

2.3 Metal-Organic Frameworks (MOFs)

MOFs are a class of materials that generated a lot of interest in the last years due to their high stability and high microporosity with tunable pore size. They are also often relatively easy to synthesize and made of cheap precursors. MOFs are coordination polymers with metal-containing clusters as building blocks, the so-called called secondary building units (SBUs), connected by organic ligands in a defined fashion. There are many ways of tuning their structure by changing either the metal in the clusters or the ligand. Possible applications of MOFs are energy storage, gas storage and separation, gas sensors or photocatalysis. Methods for preparing them include solvothermal or hydrothermal synthesis, precipitation from solution or synthesis in the microwave.[24–26] MOF synthesis is usually considered to be thermodynamically controlled, although kinetic products are also known when the formation of the thermodynamic product is sterically hindered.[27]

Light absorption of MOF photocatalysts is usually achieved by the organic ligand. The electrons are then transferred to the metal clusters, in a so-called ligand-to-metal charge transfer (LMCT). This leads to the reduction of the metal which can often be observed as a (transient) color change of the catalyst. The reduced metal species can then further reduce the reactants. Changing the ligand can enhance light absorption, for example by using NH_2-functionalized ligands. In MOFs that are built of Fe-O-based clusters light absorption does not solely take place via the ligands. Here, the clusters themselves are able to absorb light.[25]

There are many photocatalytic reactions that can be driven by MOF-based catalysts like HER, OER, overall water splitting, nitrogen reduction, CO_2 reduction or degradation of organic

pollutants. However, there are still many challenges for photocatalysis with MOFs. Poor electronic conductivity, rapid recombination of free charge carriers and insufficient long-term recyclability, related to the degradation of the framework, have prevented an application outside of research so far. To overcome these drawbacks, composites of MOFs with other materials are often created. The integration of carbon materials like graphitic carbon nitride, carbon nanotubes or graphene can improve conductivity. Metal or metal oxide cocatalysts can be introduced to enhance charge carrier separation and catalytic activity, with noble metals like Pt being a typical cocatalyst for HER. Defect engineering of the catalysts is another possibility, which can be achieved by controlling the number of defects using a modulator (molecules competing for the binding sites) to slow down or regulate the MOF synthesis. In OER, the most effective cocatalysts are also noble-metal-based.[24] Overall water splitting can be achieved by simultaneously immobilizing an oxidation and a reduction cocatalyst. Zhang et al. reported the photocatalyst Pt@NH_2-UiO-66@MnO_x consisting of Pt and MnO_x nanoparticles and the MOF NH_2-UiO-66. The Pt particles act as the proton reduction catalyst, while MnO_x drives the water oxidation. In this case, they were also able to spatially separate the two cocatalysts by embedding the Pt nanoparticles into the MOF structure and photodepositing MnO_x on its surface.[28] This example stresses the importance of controlling the location of the cocatalyst which shifts the focus again to single-site catalysis.

2.3.1 MOFs as a Platform for Single-Site Photocatalysts

Considering their defined nature, high surface area and ample options for tuning the structure, MOFs represent an ideal platform for attaching single-site catalysts. The uniform structure of MOFs and the atomically defined structure of single-site catalysts provide excellent conditions for carrying out mechanistic studies of photocatalytic reactions. High surface area enables the introduction of many catalytically active sites. High tunability can be useful for achieving selectivity towards reactants with different size by controlling the pore diameter. In comparison, zeolites can perform size-selective reactions as well. However, their small pore size of often less than 1 nm drastically reduces the number of possible catalysts. Mesoporous silica has larger pores of usually between 2 and 50 nm. This results in multiple catalyst species being in the same pore and therefore close proximity to each other, which can amplify aggregation and leaching. With MOFs, on the other hand, it is possible to design a desired intermediate pore size which can facilitate better catalytic performance.[29]

Obtaining single-site photocatalysts on a MOF can be achieved in various ways. One possibility is the incorporation of metal ions at the nodes of the framework. This can be performed by exchanging the original cluster ions with others pre- or post-synthesis, but also by attaching metal atoms to linker vacancies on the node surface. Another way is the immobilization of single-site catalysts or single atoms via spatial confinement in the MOF

cavities.[30] The most prominent functionalization of MOFs with single-site catalysts is via linker design. Some MOF ligands exhibit coordination sites for external metal atoms in addition to the functional groups binding to the nodes. Porphyrins show a pocket ideal for forming a complex with several metals. When properly functionalized, such porphyrins can be used as linkers in MOFs. MOF-525 is a Zr-based MOF with TCPP (4,4',4'',4'''-(porphyrin)-(5,10,15,20-tetrayl)tetrabenzoate) as a linker, that can incorporate many metal atoms. As an example, complexation of Co yields an efficient, visible-light-active photocatalyst for CO_2 reduction.[31] 2,2'-Bipyridine-5,5'-dicarboxylate (bpydc) is another MOF linker that can form stable complexes. NH_2 groups, which exist on some linkers can act as a monodentate ligand. More stable complexes can be obtained when the NH_2 group is further functionalized, usually with an aldehyde, to introduce another binding site.[32] A more exotic but still frequently encountered group of ligands are N-heterocyclic carbenes (NHCs). They are derived from imidazole and are functionalized with groups to bind to the metal nodes. The free electron pair of the carbene C enables complex formation with metals like Ir, as reported by Carson et al. in a Zr-based MOF.[33]

2.3.2 MOF Model Systems for Single-Site Photocatalysis

2.3.2.1 Zr-based MOFs

The prototypical Zr-based MOF is UiO-66, named after the University of Oslo where it was first synthesized. Its SBU consists of zirconium oxide clusters with the formula $Zr_6O_4(OH)_4$. In this structure, the Zr^{4+} ions form octahedra, while O^{2-} and OH^- are located at the facets of these octahedra and every cluster is connected to 12 others by terephthalate linkers.[34] This coordination results in crystals with a face-centered-cubic structure (fcc) containing tetrahedron and octahedron cages and a high porosity with surface areas often exceeding 1000 m^2/g.[35] This high surface area and its thermal, mechanical and chemical stability explain the great interest in UiO-66. Its high stability can be attributed to the strong Zr-O bond, which actually breaks only after the C-C bonds of the ligands. When heating to 300°C, the initially hydroxylated form $Zr_6O_4(OH)_4(bdc)_6$ (bdc = benzene-1,4-dicarboxylate) can be dehydroxylated reversibly under elimination of two water molecules to result $Zr_6O_6(bdc)_6$. The synthesis of UiO-66 is most of the time performed in N,N-dimethylformamide (DMF) as a solvent, terephthalic acid and a metal precursor, with the most typical being $ZrCl_4$. In addition, a modulator is usually used as well, which binds reversibly to the SBU as a competitive ligand and therefore slows down the reaction. Single carboxylic acids like acetic acid, formic acid, benzoic acid or trifluoroacetic acid are often used for this purpose, as they prevent the propagation of the crystal formation. When no modulator is used, the MOF will form very quick, which often yields gel like products instead of highly ordered crystals. By using a modulator,

a higher surface area, as well as a larger particle size and more uniform particle size distribution can be obtained.[35]

While ideal UiO-66 is a very nice model system, it is often not preferred for photocatalysis due to its low conductivity and poor visible-light-absorption. One way how the catalytic properties can be improved is the introduction of defects, which can be divided into two sub groups: missing linker and missing cluster defects.[36] Owing to the high coordination number of 12 of every SBU, the structure of UiO-66 can remain stable even after removing some ligands or nodes. The presence and type of defects can be influenced by many factors, like the type of metal precursor, the linker-to-metal ratio or the temperature during synthesis. For example, high temperature or high linker-to-metal ratio leads to fewer missing linker defects. Using more modulator increases the amount of missing linker defects, as the modulator blocks the binding sites for bdc on the nodes. Modulators with a pK_a value similar to the linkers leads to more ideal UiO-66, while ones with low pK_a result in many defects in the final MOF. In photocatalysis, defects can be beneficial by lowering the energy of empty d orbitals of Zr and therefore improving light absorption by decreasing the band gap. Missing cluster defects can have an additional effect as they enlarge the pores and facilitate access of reactants to the active sites.[36]

Another aspect that makes UiO-66 interesting is the large number of isoreticular structures. These are MOFs with the same topology (the same SBU and the same coordination) as UiO-66 that often differ in the ligand connecting the SBUs. UiO-67, which structure is shown in Figure 2, contains 4,4'-biphenyl dicarboxylate (bpdc) instead of bdc, leading to an increase in the pore aperture from 6 to 8 Å due to the larger ligand.[35] Furthermore, Fei and Cohen reported the synthesis of UiO-67-bpydc with bipyridine sites via direct MOF synthesis using H_2bpydc instead of H_2bpdc or post-synthetic ligand exchange of UiO-67. Introducing bipyridine sites enabled complexation of $PdCl_2$, which turned the MOF into an active catalyst for the Suzuki-Miyaura cross-coupling reaction.[37]

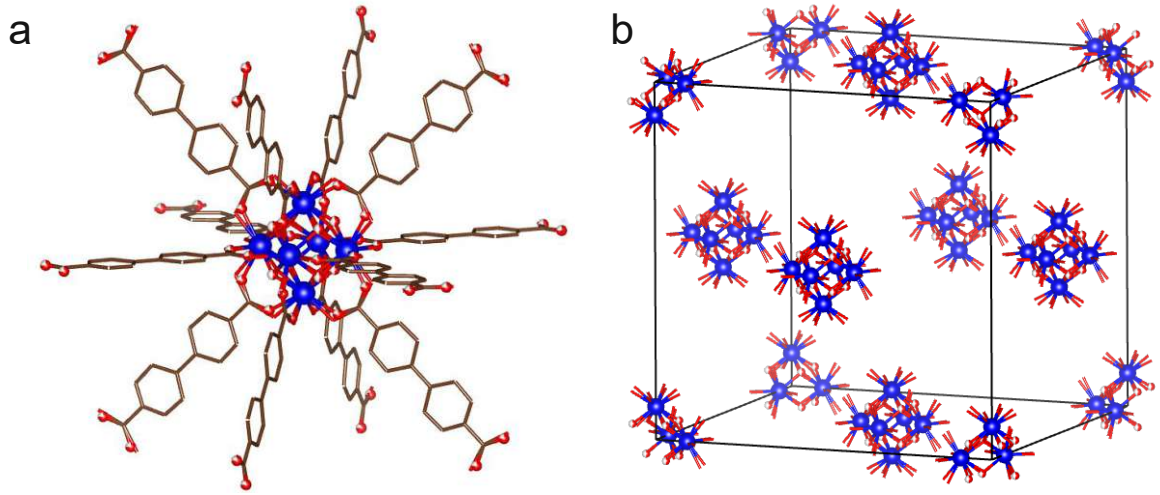

Figure 2: (a) coordination environment of $Zr_6O_4(OH)_4$ clusters in UiO-67 and (b) fcc unit cell of the clusters (blue: Zr, red: O) from cif [38]

2.3.2.2 *Ti-based MOFs*

Ti, like Zr, is also a metal that forms tetravalent ions and is therefore another candidate for the formation of MOFs with high stability. The most prominent example is MIL-125, that is constructed of $Ti_8O_8(OH)_4$ clusters and terephthalate linkers and stands out due to its high chemical and water stability, as well as photocatalytic activity.[39] The SBU is composed of TiO_6 octahedra that form cyclic octamers by corner- and edge-sharing of O. Each SBU is connected to 12 other SBUs via the terephthalate linkers, whereby 4 linkers each are on the top, on the side and on the bottom of a cyclic octamer. The resulting structure is a body-centered tetragonal lattice with both tetrahedron and octahedron cages. Surface areas of MIL-125 usually lie between 1350 and 1550 m^2/g. The synthesis is mostly performed solvothermally, with titanium chloride or more often titanium alkoxides as a precursor, DMF as a solvent and terephthalic acid as a linker. One major drawback for the application of MIL-125 as a photocatalyst is that due to the relatively large band gap of 3.69 eV, it is only photoactive under UV irradiation. When functionalizing the ligand with an amino group and using 2-aminoterephthalic acid instead of terephthalic acid, the resulting material MIL-125-NH_2 shows a decreased band gap with light absorption up to 550 nm instead of 350 nm.[39] This MOF is active for CO_2 reduction to $HCOO^-$ under visible light illumination. When performing this reaction, Ti^{4+} in clusters will be reduced to Ti^{3+} upon illumination, which acts as the active species for the redox reaction. When no CO_2 or O_2 is provided to consume the reduced Ti species, a reversible color change from yellow to green is observed.[40]

Besides MOFs with Ti_8 clusters like MIL-125, others with Ti_6 or Ti_3 clusters were also reported, as well as single Ti atoms as SBUs. However, MOFs with such 0D SBUs exhibit poor charge carrier migration, as the orbitals of the individual Ti clusters or atoms cannot overlap sufficiently. This problem can be overcome by increasing the dimensionality of the SBUs which

enables direct contact of the Ti species.[41] As an example, the SBU of MIL-177-HT is built of 1D nanowires of edge-sharing Ti_6O_9 clusters with trigonal pyramidal shape. This material can be obtained by calcination of MIL-177-LT, made of $Ti_{12}O_{15}$ clusters and 3,3',5,5'-tetracarboxydiphenylmethane (mdip) as a ligand. The formation of a 1D SBU leads to a pronounced increase in photoconductivity of the material.[42] In 2019, Smolders et al. developed a Ti-based MOF with a 2D SBU. In this new material, called COK-47, edge-sharing TiO_6 octahedra form double chains and these double chains are connected to each other by corner sharing of the octahedra to form Ti-O sheets. The SBU sheets are interconnected by bpdc linkers, always binding to an edge-sharing octahedra on one end, and to a corner-sharing octahedra on the other end (see Figure 3). They synthesized two different materials, COK-47_L and COK-47_S, which differ in particle size (L and S indicate large and small), of which COK-47_S proved to contain a high amount of missing linker defects of 39 %. Those defects are capped by either bridging or terminal methoxide groups. As an application, they were able to show that COK-47_S is active for oxidative desulfurization of benzothiophene.[43]

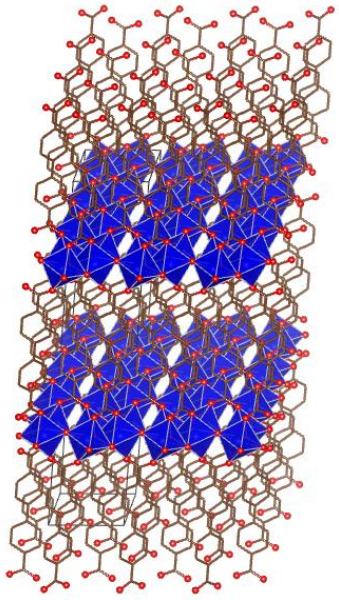

Figure 3: structure of COK-47 from cif [43]

2.4 Synthesis Strategies for MOF-based Single-Site Catalysts

Many different approaches to obtain single-site catalysts based on MOFs have been reported. This chapter will only discuss the introduction of single-site cocatalysts at binding sites of the MOF linkers. Other possibilities were briefly touched in chapter 2.3.1 and will not be further discussed here. The common strategies to achieve immobilization of single metal atoms on the MOF linkers are post-synthetic metalation, one-pot synthesis and post-synthetic ligand exchange as shown in Figure 4. These methods differ significantly in their synthetic procedures and each of them has its advantages and drawbacks. The following chapters will focus on them in detail to explain those differences.

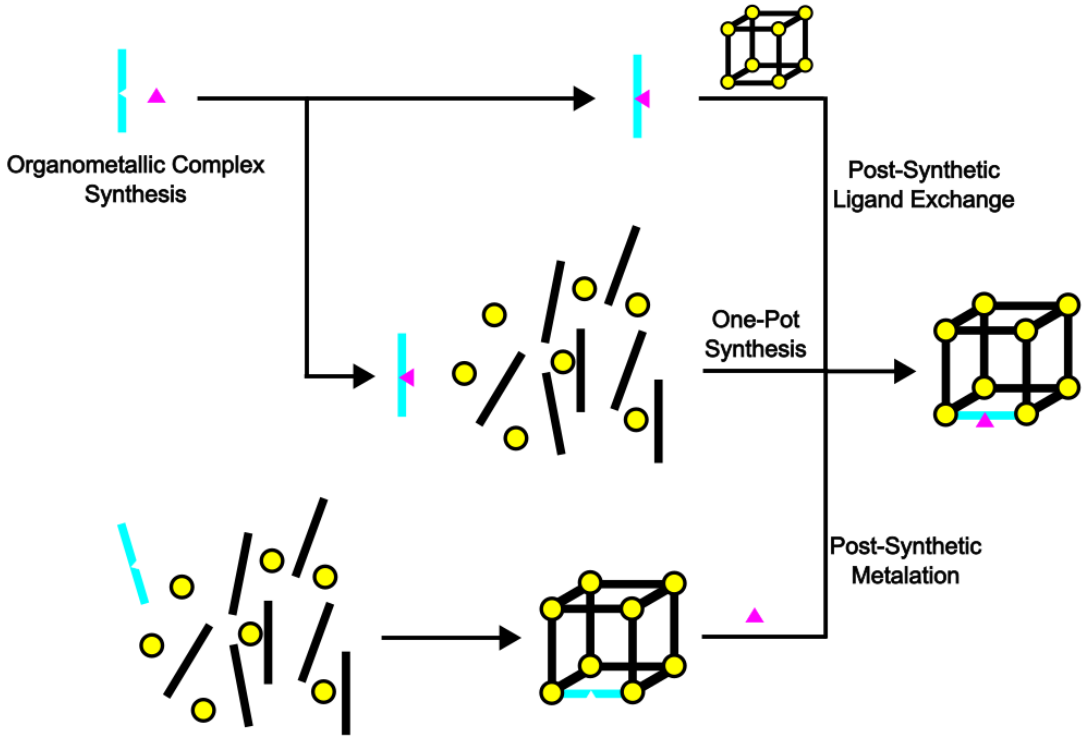

Figure 4: Common synthesis strategies to obtain single-site cocatalysts on MOF linkers

2.4.1 Post-Synthetic Metalation

Post-synthetic metalation, sometimes also referred to as metal insertion[44] or linker docking[45] is a form of post-synthetic modification of suitable MOFs. It starts with the pristine MOF that undergoes a reaction with a metal precursor, creating a metal complex at pre-existing binding sites on the MOF linker. This strategy enables high metal loadings and a wide range of linker-metal combinations is possible, as the resulting complex does not need to be pre-synthesized and isolated in molecular form. On the downside, one has little control over the metal distribution in the framework and diffusion of the precursors inside the micropores may become a limiting factor. It can happen that the precursors block the MOF pores, possibly resulting in outer-shell-only functionalization.[45] One example for such an approach was already mentioned in chapter 2.3.2.1, the complexation of $PdCl_2$ at the bipyridine sites of UiO-67-bpydc$_{0.5}$/bpdc$_{0.5}$, that Fei and Cohen reported together with the novel MOF UiO-67-bpydc. The presence of single Pd sites led to catalytic activity of the MOF in the Suzuki-Miyaura cross coupling reaction of aryl halides and arylboronic acids.[37] While noble metal-based catalysts often show good catalytic activity, the use of earth-abundant metal alternatives becomes increasingly important. It was shown that Cu single-sites can be as well incorporated into the same UiO-67-type MOF with 100 % bpydc as linker. Impregnating with $CuBr_2$ yields a Cu complex with square planar geometry on the linker sites. The prepared material proved to be an active catalyst for selective oxidation of cyclooctene to cyclooctene

oxide, showing no significant activity loss after threefold recycling, and being more active than the homogeneous counterpart [Cu(bpy)Br_2].[46] Similarly, metalation of UiO-67-bpydc with [$NiBr_2$(DME)] (DME = dimethoxyethane) yields the analogous [Ni(bpydc)Br_2] complex on the linkers. This functionalized MOF was able to catalyze the oligomerization of ethylene, where it was shown that the selectivity towards oligomers or polymers is influenced by the linker composition (bpydc or mixture of bpydc/bpdc) due to different pore environments.[47] An example where post-synthetic modification is obligatory for creating the structure is the metalation of the so-called Al-ATA MOF with Ni^{2+}. Al-ATA MOF is an Al-based MOF consisting of $AlO_4(OH)_2$ octahedra connected by 2-aminoterephthalate (ATA) linkers. The addition of the precursor $Ni(NO_3)_2 \cdot 6\ H_2O$ leads to the formation of a Ni^{2+} complex, whereby Ni not only binds to the amino group of the MOF linker, but to an SBU as well (see Figure 5a). The MOF framework is therefore necessary for the complex formation. As Al-ATA MOF itself is an active photocatalyst for water oxidation, and Ni^{2+} can promote photocatalytic hydrogen evolution, Al-ATA-Ni MOF proved to be a photocatalyst for overall water splitting.[48]

One possibility to strengthen the binding between the monodentate amino group and the metal cation and avoid coordination to an SBU is to react the amino group with an aldehyde to form the corresponding imine. If the aldehyde is properly functionalized with another electron pair donor, a bidentate ligand is created. This can be achieved either by functionalization of the metal precursor, as it was shown for $NiCl_2$-functionalization of 2-pyridine carboxaldehyde and reacting the resulting complex with the amino group of the MOF linker,[49] or by directly functionalizing the amino group, like in the case of the Zn-based MOF IRMOF-3 that was functionalized with salicylaldehyde to chelate Au^{3+} ions.[50]

While UiO-67 represents a popular starting material for single-site catalysts, Ti-based MOFs are encountered less frequent. Recently, during the work of this thesis, a Pt-functionalized derivative of COK-47 was reported (using bpydc as linker instead of bpdc) where Pt single sites were introduced by impregnation with H_2PtCl_6. This hybrid material then underwent pyrolysis at 400°C to form small amounts of TiO_2 on the surface (see Figure 5b), yielding a Z-scheme heterojunction that enabled photocatalytic hydrogen evolution under visible light illumination.[51]

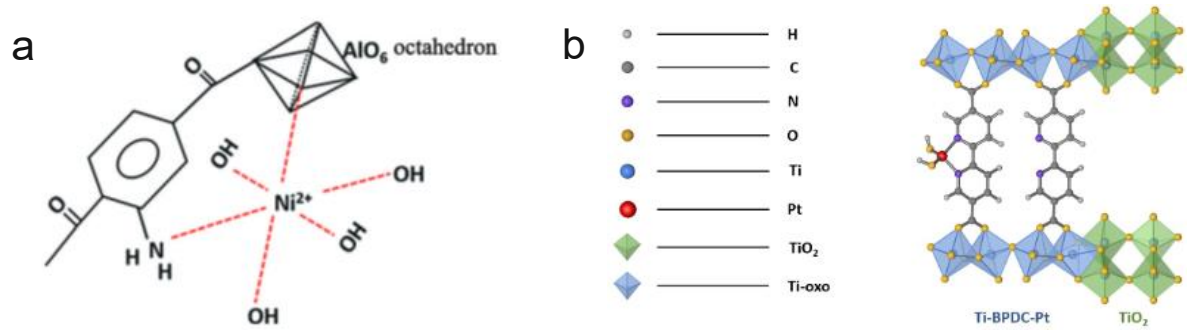

Figure 5: (a) Ni^{2+} coordination in Al-ATA MOF [48] and (b) structure of TiO_2/Ti-BPDC-Pt [51]

2.4.2 One-Pot Synthesis

In this strategy, metal-functionalized MOF linkers need to be prepared first, which are then used for a MOF synthesis (see Figure 4). It is a straightforward approach with good control over the metal position, as it is already bound to the linker beforehand. However, there are certain restrictions limiting the use of this synthetic approach. One needs to first prepare the derivatized ligand, which has to be stable during the MOF synthesis conditions and show sufficient solubility in the used solvent.[52] In most cases, this metalloligand does not make up all of the ligand used in the MOF synthesis due to steric hindrance. Instead, a mixture of the metalloligand and the original MOF linker is usually applied. When the ligands are not based on the same organic compound (for example bpdc and a bpydc-based organometallic linker), their lengths need to match in order to obtain a highly crystalline framework. This approach is called mix-and-match strategy.[30] Hou et al. applied this mix-and-match strategy to create Pt single sites in UiO-67 for hydrogen production by performing the MOF synthesis with the metalloligand [Pt(H_2bpydc)Cl_2] in addition to H_2bpdc. Furthermore, they also introduced [Ru(bpy)$_2$(H_2bpydc)]Cl_2 as photosensitizing centers in the same manner as shown in Figure 6a. The spatial proximity of the HER catalyst sites and the photosensitizer resulted in their material Ru-Pt@UiO-67 being an efficient visible light-active hydrogen evolution catalyst.[53] In another work, Kim et al. incorporated an Ir(III)-based photosensitizer into UiO-67-bpydc via the linker Na[Ir(bpydc)(ppy)$_2$] (ppy = 2-phenylpyridine). They afterwards performed post-synthetic metalation with the Pt(II) complex Zeise's salt to generate proton reduction sites (structure see Figure 6b). Introducing those in a one-pot synthesis with a Pt-containing linker produced Pt nanoparticles instead of single sites. The prepared MOF turned out to be active for photocatalytic hydrogen evolution from water, showing high stability in the process, which was ascribed to self-healing of the metal complexes: using bpydc instead of bpdc to construct the framework facilitated rebinding of leached metal ions. This is essential, since Pt nanoparticles can further autocatalyze their own formation, quickly consuming the remaining Pt(II) species. When the Pt-content was kept low with a resulting bpydc-to-Pt-ratio of 100, there was no Pt leaching observed even after 6.5 days of photocatalytic reaction.[54]

An example for a single-site-functionalized Ti-based MOF obtained by one-pot synthesis is a framework made of $Ti_3(OH)_2$ clusters linked with bpdc, combined with Ir- or Ru-based photosensitizers by performing the MOF synthesis with $[Ir(H_2bpydc)(ppy)_2]Cl$ or $[Ru(bpy)_2(H_2bpydc)]Cl_2$ in addition to the precursors H_2bpdc and $Ti_6O_6(O^iPr)_6(abz)_6$ (^{i}Pr = isopropyl, abz = 4-aminobenzoate). In both cases, the product could be used as an HER photocatalyst under visible light illumination. The mechanism of the catalytic reaction was studied in detail using 1,3-dimethyl-2-phenyl-2,3-dihydro-1H-benzo[d]imidazole (BIH) as sacrificial agent.[55] The so far listed studies on MOF-based single-site catalysts via one-pot synthesis focused on noble metal cocatalysts or photosensitizers. Reports on earth-abundant element-based cocatalysts are rare. In 2010, it was claimed in a research note that $[Ni(H_2bpydc)Cl_2]$ was used as a ligand for an Al-based MOF but no proof of the structure was presented.[56]

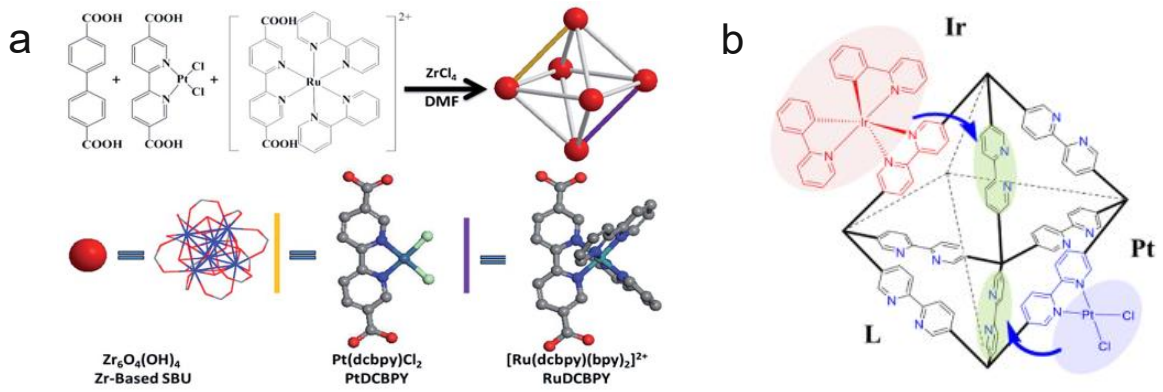

Figure 6: (a) synthesis of Ru-Pt@UiO-67 [53] and (b) structure of Pt_n_Ir_BUiO [54]

2.4.3 Post-Synthetic Ligand Exchange

Another strategy is post-synthetic ligand exchange (see Figure 4), which was first reported by Kim et al. in 2012 for UiO-66.[57] It has the benefit of the metal atom already being located at the desired linker binding site, but doesn´t require as harsh conditions as a one-pot synthesis. To perform post-synthetic ligand exchange, or sometimes also called solvent-assisted linker exchange (SALE), the pristine MOF is suspended in solution containing the new, derivatized linker which will then be incorporated into the original MOF. This exchange process favors the replacement of weaker with stronger bases. Additionally, ligand solubility and therefore the solvent plays a crucial role to guarantee diffusion into the framework interior.[52] The requirement of only mild conditions can be illustrated by UiO-67 doped with Rh single sites. Here, the original UiO-67 interchanged with the complex $[Rh(H_2bpydc)Cp^*Cl]Cl$ (Cp^* = pentamethylcyclopentadiene) in water at room temperature for 24 h, resulting in the structure shown in Figure 7a. When the resulting material was combined with the homogeneous photosensitizer $[Ru(bpy)_3]Cl_2$ the system became active for photocatalytic CO_2 reduction to formate, with activity comparable to a corresponding fully homogeneous system, but better

stability, selectivity and recyclability.[58] Another photocatalyst for CO_2 reduction prepared by post-synthetic ligand exchange is UiO-67 functionalized with the Re complex [Re(bpydc)$(CO)_3$Cl] that can serve both as photosensitizer and catalyst. This material was also synthesized at room temperature in an aqueous medium and with a reaction time of 5 days.[59] A method similar to solvent-assisted linker exchange is solvent-assisted ligand incorporation (SALI), first reported by Deria et al. in 2013. In this case, a bare or metallized monofunctionalized ligand is used instead of a bifunctionalized one, which binds to an SBU without linking it to another one. In their work, they used this method to attach perfluoroalkane carboxylates to the Zr-based MOF NU-1000.[60] SALI was then later also applied for introducing organometallic compounds into MOFs. The same MOF NU-1000, which is composed of Zr_6-based nodes and 1,3,6,8-tetrakis(p-benzoic acid)pyrene linkers, can be taken as a platform to attach fac-[Re(bpydc)Br$(CO)_3$] and [CoCl$(dmgH)_2$(4-COOH-py)] (dmgH = dimethylglyoxime, py = pyridine) as shown in Figure 7b for the Re complex. The reaction is in this case carried out in DMF at 65°C for 24 h. As the Re complex works as a CO_2 reduction catalyst and the Co complex as an HER catalyst, the composite is able to produce syngas (CO + H_2) by the means of photocatalysis. The ratio of CO to H_2 is adjustable by varying the ratio of the metalloligands.[61]

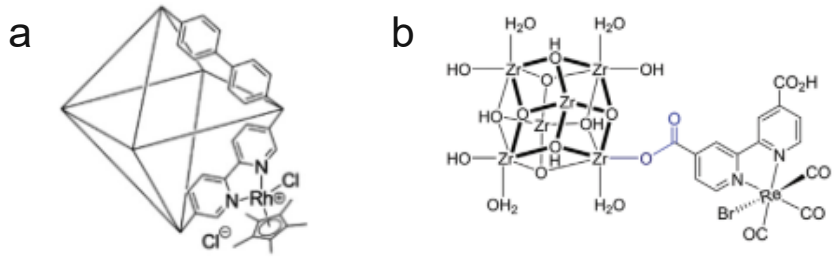

*Figure 7: structure of (a) Cp*Rh@UiO-67 obtained by post-synthetic ligand exchange [58] and (b) a NU-1000 node after solvent-assisted ligand incorporation of a monofunctionalized ligand [61]*

3 Motivation and Aims

As described in the introduction, single metal atoms as active sites show great benefits for photocatalysis compared to larger particles due to their defined nature and the possibility of maximum atom utilization efficiency, resulting in materials with new electronic and catalytic properties. Metal-organic frameworks represent an ideal platform for such single-site cocatalysts, as they exhibit a large surface area and their high tunability enables ample possibilities for stabilizing single metal atoms. Hereby, the usage of pre-functionalized organometallic complexes as MOF linkers allows the highest control over the structure of the catalytic sites compared to node functionalization or post-synthetic metalation of linker binding sites, as the metal atom is already sitting at the desired spot. Additionally, the scarcity and price of the most commonly used cocatalysts limit their economic utility, where earth-abundant metals are much preferred.

The aim of this thesis is therefore to use organometallic complexes to incorporate catalytically active single sites into MOF model systems via direct one-pot synthesis or post-synthetic ligand exchange. Another goal was to study, how the substitution of noble metals with cheaper alternatives effects the properties and catalytic activity for hydrogen evolution of such materials. For that purpose, single sites of Pt and Ni were selected as desired cocatalysts. UiO-67 and COK-47 were chosen as MOF model systems. UiO-67 is a widely-used and well-understood model system, for which a successful one-pot synthesis with a Pt-containing MOF linker has already been reported and HER activity was shown.[53] However, we believe that the influence of the synthesis strategy and the amount of cocatalyst loading can be further elucidated. The introduction of Ni single sites onto UiO-67 has, to our knowledge, so far only been reported by post-synthetic metalation and for other applications than photocatalytic water splitting.[47] The other chosen model system, COK-47, is a very interesting material with 2D SBUs, where previous experience in the group showed excellent activity for photocatalytic hydrogen evolution after photodeposition of Pt nanoparticles as active sites.[62] The immobilization of single site cocatalysts on COK-47 has, to our knowledge, not been reported before the start of this thesis. Recently however, post-synthetic metalation with Pt of a COK-47-derived material has been published.[51]

4 Materials and Methods

4.1 List of Chemicals

Information about the used chemicals is given in Table 1. All chemicals were used without further purification.

Table 1: List of used chemicals

Name	Molecular Formula	CAS Registry Number	Purity	Supplier
Acetic acid	CH_3COOH	7732-18-5	98 %	Fisher Scientific
Biphenyl-4,4′-dicarboxylic acid	$C_{14}H_{10}O_4$	787-70-2	98 %	abcr
2,2'-Bipyridine-5,5'-dicarboxylic acid	$C_{12}H_8N_2O_4$	1802-30-8	98.0 %	Tokyo Chemical Industry
Bis(cyclopentadienyl)titanium(IV) dichloride	$[Ti(C_5H_5)_2Cl_2]$	1271-19-8	98.0 %	Sigma-Aldrich
Deuterium oxide	D_2O	7789-20-0	99,9 atom-% D	Sigma-Aldrich
Dimethyl sulfoxide	$(CH_3)_2SO$	67-68-5	99.5 %	PanReac AppliChem ITW Reagents
Dimethyl sulfoxide, absolute	$(CH_3)_2SO$	67-68-5	Absolute (≤ 0.02 % water)	Sigma-Aldrich
Ethanol, absolute	C_2H_5OH	64-17-5	99.8 %	Chem-Lab
Hexachloroplatinic acid, 8 wt-% in water	H_2PtCl_6	16941-12-1		Fluka
Methanol	CH_3OH	67-56-1	Technical	Donau Chemie
Methanol, HPLC grade	CH_3OH	67-56-1	99.99 %	VWR Chemicals BDH

Methanol, absolute	CH_3OH	67-56-1	99.8 %	Thermo Scientific
Nickel(II)chloride	$NiCl_2$	7718-54-9	98 %	Sigma-Aldrich
Nickel(II)chloride hexahydrate	$NiCl_2 \cdot 6\ H_2O$	7791-20-0	98 %	Merck
N,N-Dimethylformamide	C_3H_7NO	68-12-2	98 %	VWR Chemicals BDH
N,N-Dimethylformamide, absolute	C_3H_7NO	68-12-2	99.8 %	Thermo Scientific
Potassium trichloro(ethylene)platinate(II) hydrate / Zeise´s salt	$K[Pt(C_2H_4)Cl_3] \cdot H_2O$	123334-22-5		Sigma-Aldrich
Propylene carbonate	$C_4H_6O_3$	108-32-7	99.0 %	Merck
Sodium hydroxide	NaOH	1310-73-2	98 %	Sigma-Aldrich
Titanium(IV) isopropoxide	$Ti[OCH(CH_3)_2]_4$	546-68-9	97 %	Sigma-Aldrich
Zirconium(IV) chloride	$ZrCl_4$	10026-11-6	99.5 %	Sigma-Aldrich

4.2 Characterization Methods

The band gap and the absorption profile of synthesized materials was determined by diffuse reflectance spectroscopy (DRS) with a JASCO V-670 spectrometer. The sample was pressed onto a quartz disc and the reflectance was measured in the range from 200 to 900 nm. Anhydrous $MgSO_4$ was used for baseline acquisition.

Fourier-transform infrared spectroscopy (FTIR) in attenuated total reflectance (ATR) mode was applied to analyze vibrations of chemical bonds. The measurements were acquired with a Perkin Elmer Spectrum Two from 4000 to 400 cm^{-1} by pressing the sample onto the ATR crystal.

Powder x-ray diffraction (XRD) allows phase identification for crystalline samples. An XPERT II: PANalytical Xpert Pro MPD was used in Bragg-Brentano geometry. Diffractograms were acquired from 5 to 90°, using Cu Kα radiation (1.5406 Å) as x-ray source and an X´Celerator (2.1°) semiconductor detector.

Structural information of synthesized organometallic complexes was carried out with proton nuclear magnetic resonance spectroscopy (^{1}H NMR) at 250 MHz. Samples were dissolved in 0.15 M KOH solution in 9:1 H_2O:D_2O and measured with a Bruker Advance 250 NMR spectrometer.

Elemental analysis of relevant elements was performed by total-reflection x-ray fluorescence spectroscopy (TXRF) with an ATOMIKA 8030C. Excitation was usually done with Mo Kα radiation (17.480 keV) with the exception being UiO-67 samples, where W bremsstrahlung (centered around 35 keV) was used because, as the Zr K lines overlap with Mo Kα. However, it needs to be considered that this excitation source is also not ideal, as its energy is already well above the elemental lines that are to be excited. The intensity of the emitted x-rays was measured with an energy dispersive Si(Li) detector. MOF samples were put on a quartz reflector and were covered with 5 µL of 1 % polyvinyl alcohol (PVA) solution, after which they were dried to fix the sample on the surface. Calculation of the cocatalyst loading was done via the ratio of the MOF metal (Zr or Ti) to the cocatalyst metal (Pt or Ni), initially assuming a defect-free MOF structure. MOF linkers were analyzed as 1 mg/mL solutions/suspensions in 0.3 M NaOH or KOH. 10 ppm of Y were added as internal standard to calculate the concentration of the cocatalyst metal. 5 µL of this sample solution were put on a quartz reflector and dried.

UiO-67 shows fluorescence in the UV region. To observe its quenching by the cocatalyst and changes in the relaxation mechanism, photoluminescence spectroscopy (PL) measurements were performed, using a FluoTime 300 spectrometer. Steady state measurements were carried out with a Coaxial UV-Xenon arc lamp with a high resolution excitation double monochromator, where an excitation wavelength of 315 nm was selected. This is below the excitation maximum of UiO-67 as a 320 nm low-pass filter was needed to cut off the excitation wavelength. For time-resolved measurements, a PDL 820 diode laser driver with an LDH-P-C-375 laser head was used (emission at 375 nm), with a 395 nm low-pass filter eliminating the laser wavelength after interaction with the sample. A PMA Hybrid 07 detector with a high resolution emission double monochromator was used for detection. A detection wavelength of 400 nm was selected for time-resolved measurements, which is higher than the emission maximum, again due to constraints with available filters.

X-ray photoelectron spectroscopy (XPS) was measured for the functionalized MOF linkers to observe oxidation state changes upon binding of the metal cation. Measurements were performed on a SPECS XPS spectrometer with monochromatized Al Kα radiation (µFocus 350) for excitation and a hemispherical WAL-150 analyzer for detecting the emitted

photoelectrons. Samples were immobilized on the sample holder with double-sided carbon tape.

The amount of missing ligands in the MOF structures was determined by means of thermogravimetric analysis (TGA) with a PerkinElmer TGA 8000. Samples were put into Al_2O_3 crucibles and heated from 30 to 600°C with 5°C/min in N_2 or synthetic air atmosphere.

5 Experimental Part

5.1 Synthesis Procedures

5.1.1 Organometallic Complexes

5.1.1.1 [Pt(H_2bpydc)Cl_2]

[Pt(H_2bpydc)Cl_2] alias **Pt ligand** (see Figure 9a) was synthesized based on reported procedures with minor adaptions.[54,63] 0.27 mmol Zeise´s salt (104 mg for monohydrate) and 0.24 mmol H_2bpydc (59 mg) were mixed and flushed with Ar at a Schlenk line. 3.5 mL MeOH (HPLC grade) were added with a syringe and the mixture was heated to reflux within approx. 25 min. After refluxing for another 15 min under Ar atmosphere, the resulting orange suspension was separated by vacuum filtration and washed 3 times with 3.5 mL MeOH (technical) each. The product was pre-dried at 50°C for 1 h under vacuum, milled in a mortar and dried at 60°C under vacuum over night. The resulting powder was of red/brown color.

5.1.1.2 [Ni(H_2bpydc)Cl_2]

The synthesis of [Ni(H_2bpydc)Cl_2] alias **Ni ligand** (see Figure 9b) was adapted from literature,[56] as H_2bpydc proved to be not soluble in EtOH at room temperature. $NiCl_2$ was pre-dried under vacuum at 110°C over night. The dried $NiCl_2$ (amount see Table 5 in appendix) was mixed with 0.5 eq. H_2bpydc and 6 mL EtOH (absolute) per 100 mg $NiCl_2$ and flushed with Ar at a Schlenk line. The mixture was heated to reflux and stirred for 4.5 h under Ar atmosphere. Afterwards, the green suspension was separated by vacuum filtration and washed 3 times with the respective reaction volume of EtOH each. The green product was pre-dried at 50°C for 1 h under vacuum, milled in a mortar and dried at 70°C under vacuum over night.

5.1.2 MOF synthesis

5.1.2.1 UiO-67: One-Pot Synthesis and non-functionalized MOFs

The following procedure was used to obtain both pristine UiO-67 and corresponding mixed-ligand MOFs additionally containing bpydc, Pt ligand or Ni ligand as linkers. 0.5 mmol $ZrCl_4$ (116.5 mg) were weighed into an Ar-filled 30 mL microwave vial and 4 mL DMF (technical) and 15 mmol acetic acid (860 µL) were added. The solution was sonicated for 5 min and a mixture of 0.5 mmol MOF linker(s) (either only H_2bpdc or a mixture of H_2bpdc and another linker, see Table 5 in appendix) in 5 mL DMF (technical, sonicated for 5 min) was added. The reaction mixture was sonicated for 1 min and heated in a microwave oven (Anton Paar Monowave 300) at 120°C for 2 h at 600 rpm stirring. The MOF was isolated by vacuum filtration and washed 3 times with 10 mL DMF (technical) each, followed by washing 3 times with 10 mL MeOH (technical) each. The product was pre-dried at 50°C for 1 h under vacuum, milled in a mortar and dried at 100°C under vacuum over night.

5.1.2.2 COK-47: One-Pot Synthesis and non-functionalized MOFs

The following procedure was used to obtain both pristine COK-47 and corresponding mixed-ligand MOFs additionally containing bpydc, Pt ligand or Ni ligand as linkers. A varying amount of MOF linker(s) (either only H_2bpdc or a mixture of H_2bpdc and another linker, see Table 5 in appendix) was flushed with Ar in a 30 mL microwave vial. 9 mL DMF (absolute) and 1 mL MeOH (HPLC grade) were added and the mixture was sonicated for 5 min. Afterwards, 0.5 mmol Titanium(IV) isopropoxide (TTIP, 148 µL) were added under Ar atmosphere. The reaction mixture was then sonicated for 1 min and heated in the microwave oven at 600 rpm stirring (temperature and time see Table 5 in appendix). The MOF was isolated by vacuum filtration and washed 3 times with 10 mL DMF (technical) each, followed by washing 3 times with 10 mL MeOH (technical) each. The product was pre-dried at 50°C for 1 h under vacuum, milled in a mortar and dried at 100°C under vacuum over night.

5.1.2.3 COK-47$_S$

The missing-ligand (i.e. porous) version of COK-47 from Smolders et al., COK-47$_S$,[43] was obtained by an adapted method. 0.619 mmol H_2bpdc (150 mg) were mixed with 0.375 mmol [$Ti(C_5H_5)_2Cl_2$] (93.8 mg) and approx. 300 mg glass beads in a 30 mL microwave vial that was then flushed with Ar. 1.5 mL DMF (absolute), 375 µL mL propylene carbonate and 300 µL acetic acid were added and the reaction mixture was sonicated for 5 min. Afterwards, it was heated to 185°C in the microwave oven within 5.5 min, and kept at this temperature for 15 min at 600 rpm stirring. COK-47$_s$ was then isolated by vacuum filtration under Ar atmosphere and was washed 2 times with 5 mL DMSO (absolute) each, then 4 times with 2.5 mL MeOH (absolute) each. The yellow-brown product was then dried at 200°C under vacuum over night, milled in a mortar and stored in a desiccator under vacuum.

5.1.2.4 Post-Synthetic Ligand Exchange of UiO-67, COK-47 and COK-47$_S$

The general procedure for ligand exchange synthesis was adapted from literature.[58] 50 mg of the pristine MOF (UiO-67, COK-47 or COK-47$_S$) were mixed with the desired functionalized MOF linker (Pt ligand or Ni ligand) so that the functionalized linker would constitute 4 mol-% of the total amount of linkers, assuming a defect-free MOF structure, and 2.5 mL reaction medium (H_2O or technical DMF, see Table 5 in appendix). The suspension was sonicated for 5 min and afterwards stirred for 24 h at 400 rpm at room temperature. The solid was isolated by vacuum filtration and 2.5 mL of washing medium were added (technical DMF or DMSO, see Table 5 in appendix). After 5 min of sonication, the suspension was stirred for 1 h at 400 rpm at room temperature. The functionalized MOF was isolated by vacuum filtration and washed 3 times with 2.5 mL DMF (technical) each, followed by washing 3 times with 2.5 mL MeOH (technical) each. The product was pre-dried at 50°C for 1 h under vacuum, milled in a mortar and dried at 100°C under vacuum over night.

5.2 Evaluation of the Photocatalytic Activity

The activity of prepared MOFs for photocatalytic hydrogen evolution was determined by illuminating a catalyst suspension in a mixture of water (as proton donor) and MeOH (as sacrificial agent) for a defined time and measuring the amount of formed H_2 by gas chromatography (GC). A suspension with a catalyst concentration of 1 mg/mL in a 1:1 mixture of water and MeOH (HPLC grade) was prepared and sonicated for 3 min. 2 mL of this suspension were filled into a 9 mL reactor with a cooling jacket (see Figure 8). In case of cocatalyst photodeposition, a small amount of precursor solution was added in the dark. For Pt photodeposition, a 4.10 mmol/L H_2PtCl_6 solution (1:50 dilution of the 8 wt-% stock solution) was used, of which 50 µL are necessary for 2 wt-% Pt on the catalyst. For Ni photodeposition, a 4.09 mmol/L $NiCl_2$ solution was added, where 50 µL equal 0.6 wt-% Ni. The reactor was closed and purged with 10 mL/min Ar flow for 10 min, the reaction mixture was stirred at 600 rpm and cooled with 15°C water. Headspace samples for GC analyses were collected before illumination, after 30 min illumination and after 60 min illumination. The light source was placed so that the light enters the reactor from the side, using a SOLIS-365C LED (365 nm) from Thorlabs for COK-47-based samples and a Lumatec SUV-DC super pressure Hg lamp in deep UV mode (220 to 400 nm) for UiO-67-based samples, as UiO-67 is not photoactive at 365 nm. For quantifying the formed H_2 amount, illumination was shortly stopped and a 200 µL aliquot of the headspace was injected into a Shimadzu Nexis GC-230 with a split ratio of 4. The GC was equipped with a micropacked ShinCarbon ST column, that was operated at 100°C with 7 mL/min He as carrier gas, and a barrier discharge ionization (BID) detector.

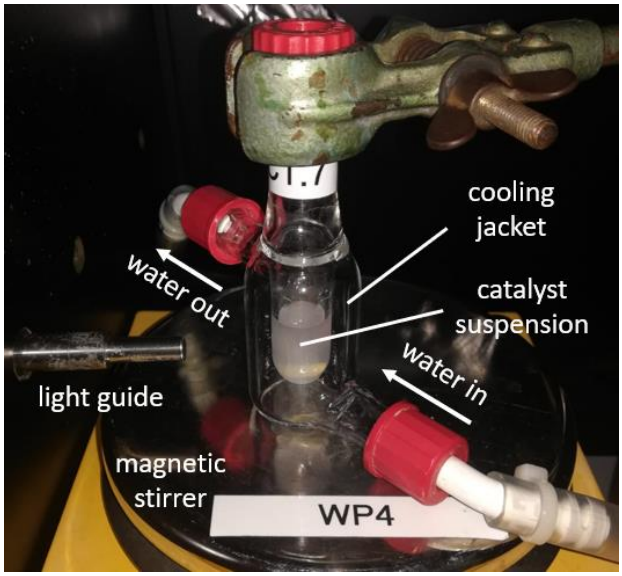

Figure 8: Reactor setup for photocatalytic experiments (illumination with Hg lamp)

6 Results and Discussion

The organometallic complexes [Pt(H_2bpydc)Cl_2] (Pt ligand) and [Ni(H_2bpydc)Cl_2] (Ni ligand) were synthesized and incorporated into the frameworks of UiO-67 and COK-47 by direct one-pot synthesis and post-synthetic ligand exchange as described in the experimental section. In order to keep the structure as close as possible to the pristine MOFs, only a small amount of those functionalized ligands was introduced (up to 4 %) with the initial bpdc making up the remaining linkers. An overview about which parts of the have been reported previously in literature is given in Table 2. Pt single sites on UiO-67 were used as a reference system, as one-pot synthesis of such materials had already been reported before, but new insights into the influence of the cocatalyst loading and a comparison to post-synthetic ligand exchange as an alternative synthesis method were provided nevertheless. The other photocatalytic systems used in this work were more novel. The following chapters will first discuss the characterization of the organometallic complexes, followed by the characterization and activity evaluation of metal-functionalized UiO-67 and COK-47 MOFs. The influence of synthesis method and cocatalyst, comparing single-metal-sites and corresponding nanoparticles, will be explained in detail.

Table 2: Overview about reported and not reported parts of the thesis (PSM = post-synthetic metalation)

		Cocatalyst	
		Pt single sites	Ni single sites
MOF model system	UiO-67	Reported [53]	Only PSM reported [47]
	COK-47	Only PSM reported [51]	Not reported

6.1 Organometallic Complexes

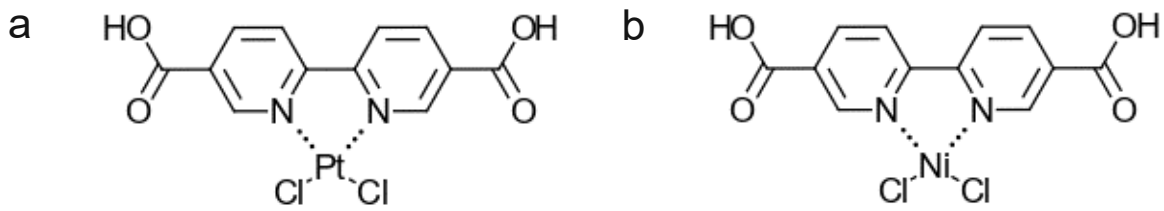

Figure 9: expected structures of (a) Pt ligand and (b) Ni ligand

The intended structures of both Pt ligand and Ni ligand are shown in Figure 9. Both complexes were isolated as crystalline powders, which was proven by powder XRD (see Figure 10a and b). Different batches of the same compound show the same main features, but some peaks appear for certain batches that do not appear for others, which may arise from impurities. One batch of Ni ligand (Ni-bpydc-2) also exhibits shifted peaks at low angles compared to the other two, possibly because of non-ideal alignment in sample preparation.

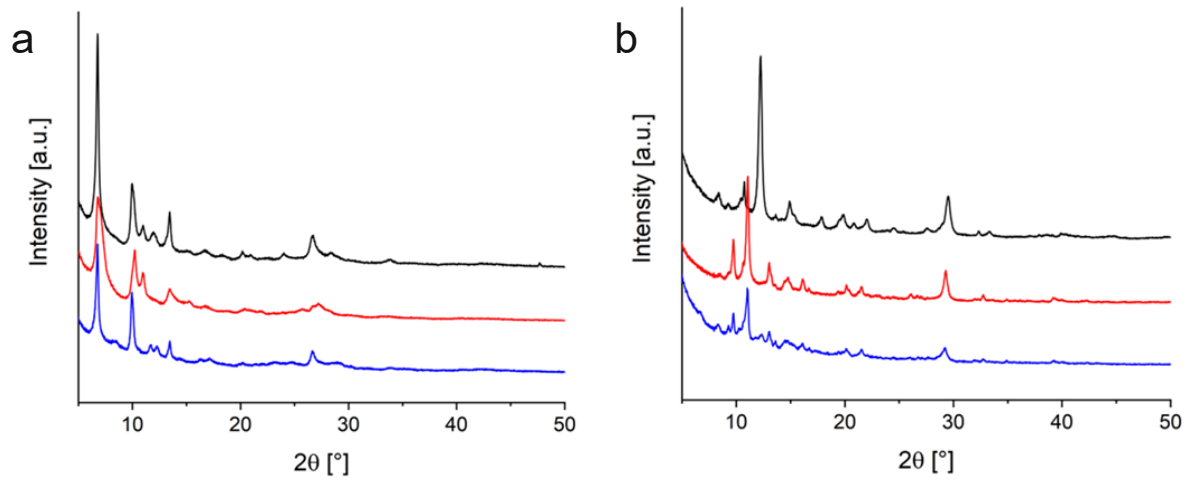

Figure 10: Powder XRD diffractograms of (a) different batches of Pt ligand (Pt-bpydc-1, Pt-bpydc-2, Pt-bpydc-3, top to bottom) and (b) different batches of Ni ligand (Ni-bpydc-2, Ni-bpydc-3, Ni-bpydc-4, top to bottom)

FTIR spectra of Pt ligand and Ni ligand show distinct changes compared to the unfunctionalized organic compound H_2bpydc. There is also a shift of the C=O band at 1682 cm^{-1} [64] to higher wavenumbers as depicted in Figure 11a. This indicates that the carboxylic groups, which constitute the future binding sites to the MOF nodes, are still intact, as carboxylate formation would result in a major shift to lower wavenumbers.[65] Successfully synthesized batches of the same complex (Pt ligand or Ni ligand) all show the same FTIR spectrum which indicates reproducibility of the syntheses when neglecting possible impurities seen in XRD.

An interesting phenomenon occurred when Ni ligand came in contact with water. Its color changed irreversibly from green to turquoise. FTIR was consequently also used to analyze the effect of water on Ni ligand. It can be seen in Figure 11b that the C=O band disappears or possibly strongly shifts to lower wavenumbers after H_2O treatment, which can be attributed to decarboxylation of H_2bpydc or carboxylate formation, respectively. This suggests that Ni ligand is not stable in aqueous suspension. When treating Ni ligand with DMF, the FTIR spectrum changes as well, but the C=O band remains around 1710 cm^{-1}.

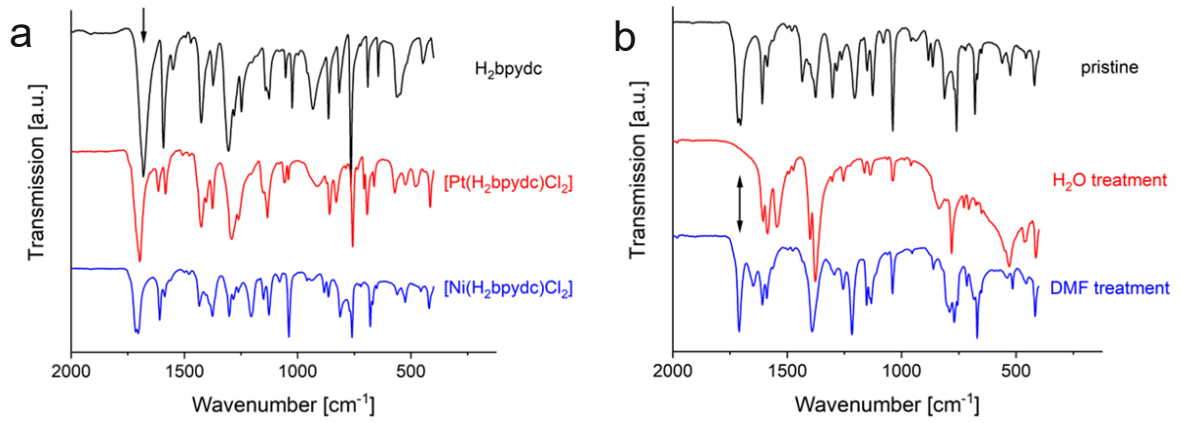

Figure 11: FTIR Spectra comparing (a) Pt ligand (Pt-bpydc-2) and Ni ligand (Ni-bpydc-3) to the unfunctionalized H_2bpydc with the C=O band shifting to higher wavenumbers (see arrow) and (b) Ni ligand (Ni-bpydc-3) as synthesized (pristine) to itself after treatment with H_2O or DMF with the C=O band disappearing for H_2O treatment (see arrow)

UV/Vis DRS spectra of the synthesized organometallic complexes are shown in Figure 12. Successfully synthesized batches of the same complex (Pt ligand or Ni ligand) all show the same DRS spectrum which again indicates reproducibility of the synthetic procedures. Pt ligand absorbs considerably in the visible range, explaining its dark red-brown color which was also reported in literature for the used synthesis method.[54,63] Interestingly, however, other synthesis methods starting from *cis*-$PtCl_2(DMSO)_2$ yield complexes of yellow color,[53,66,67] possibly due to a different coordination environment. For Ni ligand, The bands at 415 nm and 690 nm are well-reported for d-d transitions of octahedral Ni(II) species, with the former corresponding to a $^3A_{2g}(^3F)$ to $^3T_{1g}(^3P)$ and the latter to a $^3A_{2g}(^3F)$ to $^3T_{1g}(^3F)$ transition.[68,69] While this suggests that ionic instead of metallic Ni is present as intended, it also indicates that Ni ligand might not exhibit the targeted coordination number of 4, but rather 6. The additional two bonds might arise from additional coordination of the already present ligands, H_2bpydc or Cl, or by coordination of solvent molecules.

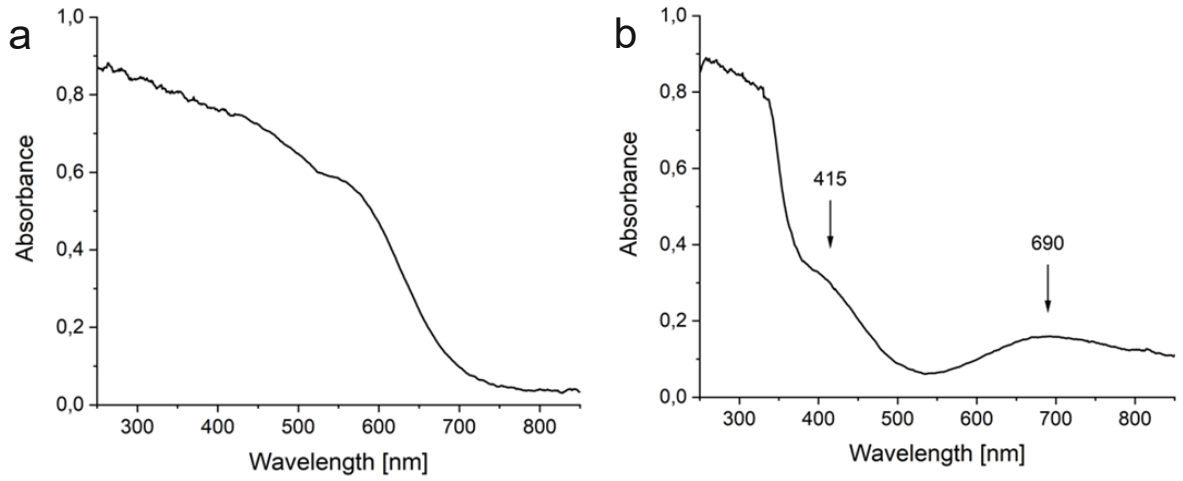

Figure 12: UV/Vis DRS spectra of (a) Pt ligand (Pt-bpydc-2) and (b) Ni ligand (Ni-bpydc-3)

The elemental loadings of Cl and the respective metal, Pt or Ni, were determined by TXRF and compared to the theoretical values (see Figure 13). The absolute loadings fluctuate quite a lot between different batches, which could be attributed to either deviations in sample preparation or impurities. A likely impurity for Pt ligand would be K, as it is contained in the precursor, Zeise´s salt, however, K was only found in very small amounts in samples that were not dissolved in 0.3 M KOH. Deviations from sample preparation are very plausible, as they could stem from weighing errors of the samples themselves, pipetting errors when adding the solvent or internal standard, or inhomogeneity of the sample solution since Pt ligand was not fully soluble in 0.3 M NaOH.

A sandwich complex of two H_2bpydc ligands binding to the metal cation without any Cl ligands is unlikely for both Pt ligand and Ni ligand, as Cl was found for both samples. For Pt ligand, the ratio of Pt to Cl is in reasonable agreement with the theoretical values. Ni ligand on the other hand contains a lot less Cl than expected. This could be explained by Cl ligands either being partially replaced by other ligands like solvent molecules, or by the sample containing a mixture of two complexes, where one of them doesn´t contain any Cl ligands. Figure 13b also compares the measured Ni and Cl loadings of Ni ligand to a possible octahedral complex (as suggested by DRS), but definite clarification of the structure cannot be offered due to the strong fluctuation between different batches.

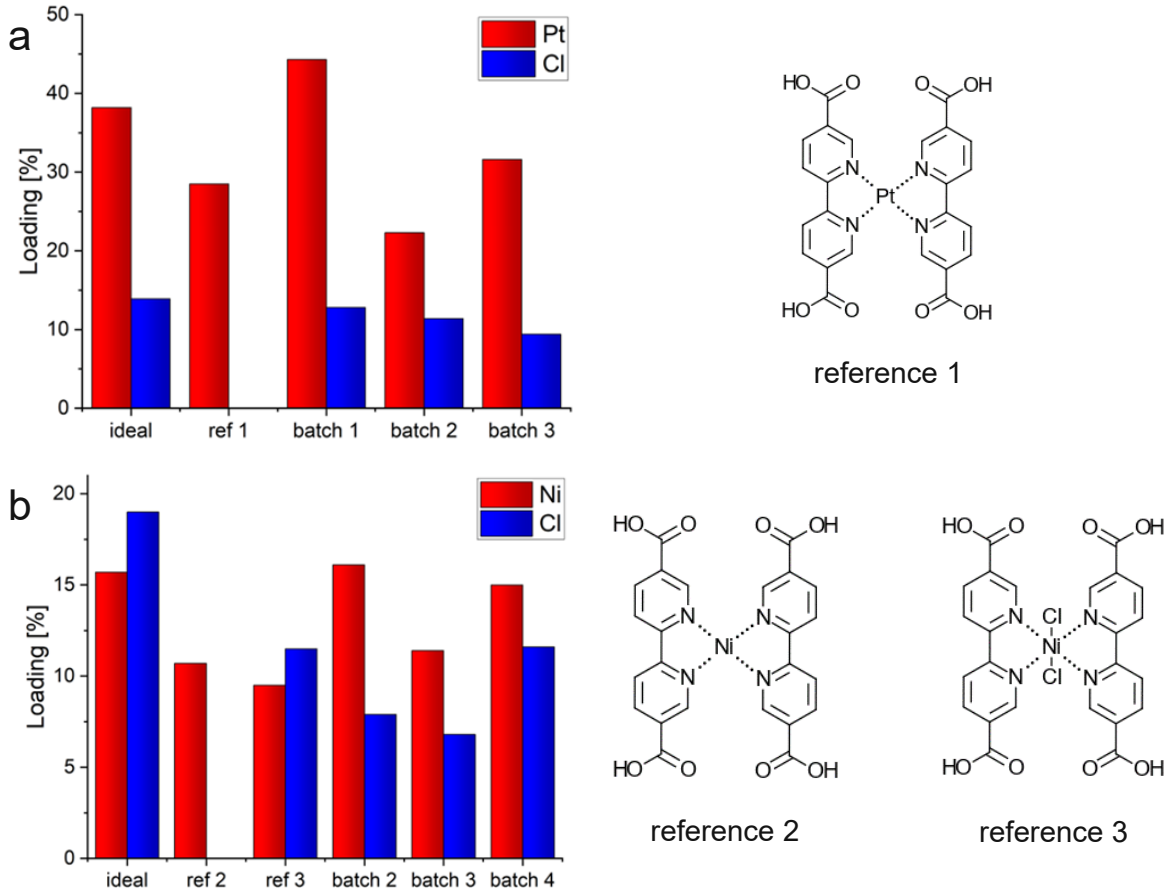

Figure 13: Elemental loadings of (a) Pt ligand batches (Pt-bpydc-1, Pt-bpydc-2, Pt-bpydc-3) and (b) Ni ligand batches (Ni-bpydc-2, Ni-bpydc-3, Ni-bpydc-4) determined by TXRF compared to the theoretical loadings (ideal) and other possible reference structures

To confirm the coordinative bond between a metal cation and an organic ligand, ^{1}H NMR can be used as a simple and reliable method, as donation of electron density from the ligand to the metal will result in deshielding of the organic ligand´s protons which leads to a shift of the corresponding NMR signals to higher ppm values. This phenomenon was observed for Pt ligand as shown in Figure 14a and the shifts were also confirmed by measuring ^{1}H NMR spectra of a physical mixture of Pt ligand and the non-functionalized bpydc^{2-} linker to exclude shifts resulting from other factors (see Figure 33a in appendix). Interestingly, the formation of the complex also led to a decrease in intensity of the proton signals. For Ni ligand, the signals disappeared almost completely after complex formation, which can be explained by considering the expected magnetism of the structures. Pt ligand is expected to be a square planar complex and would therefore be diamagnetic as illustrated in Figure 14b. For Ni ligand, however, the expected lower ligand field split would likely result in a tetrahedral complex for a coordination number of 4. Such a complex would contain unpaired electrons and consequently be paramagnetic. An octahedral d^{8} complex, as DRS spectra suggested Ni ligand to be, would be paramagnetic as well. The absence of ^{1}H NMR signals for Ni ligand can therefore be seen as an indirect indication that a complex did form (either tetrahedral or octahedral).

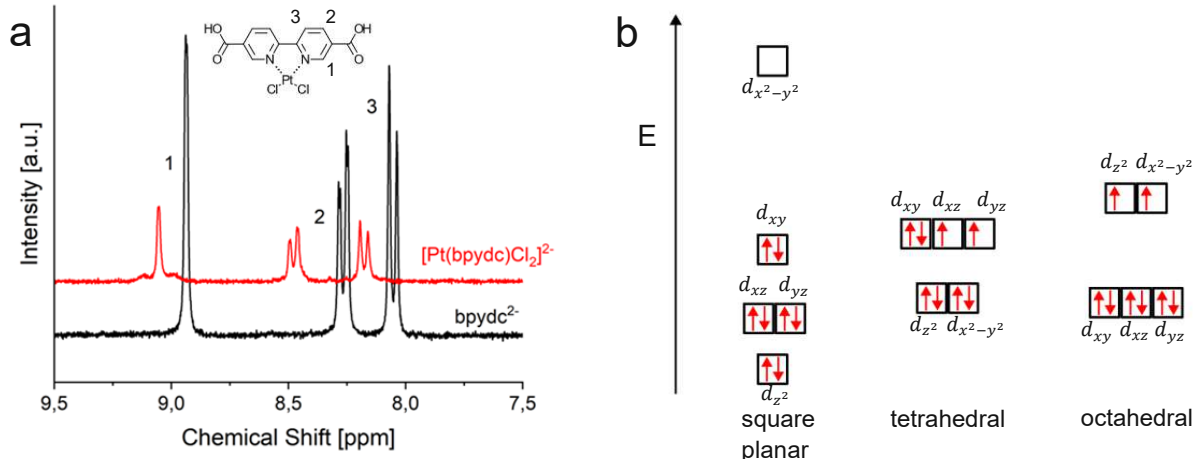

Figure 14: (a) ^{1}H NMR spectrum of Pt ligand (Pt-bpydc-2) compared to non-functionalized bpydc^{2-}, (b) exemplary energy level diagrams of square planar (expected for Pt ligand), tetrahedral (intended for Ni ligand) and octahedral (possible for Ni ligand) d^{8} complexes

To further confirm the coordination bond between the H_2bpydc ligand and the respective metal cation as well as the metal oxidation states, XPS measurements were conducted. The spectra are very noisy, but certain conclusions can still be drawn. The Pt 4f and Ni 2p regions, displayed in Figure 15a and b, show that ionic species of Pt and Ni are present, as signals of metallic Pt or Ni would appear at significantly lower binding energies and with different peak shapes.[53,70–72] Furthermore, the binding energies of the N 1s electrons strongly indicate an interaction between the N-moieties of H_2bpydc with Pt and Ni, as they shift from 399.2 eV to 401.6 eV and 400.2 eV for Pt ligand and Ni ligand, respectively (see Figure 15c). This shift matches well with the NMR results that the N atoms donate electron density to the metal centers, leading to the withdrawal of electron density from the organic linker and a higher binding energy of the N core electrons.[51] The XPS results also suggest that the interaction of H_2bpydc with Pt is stronger than with Ni.

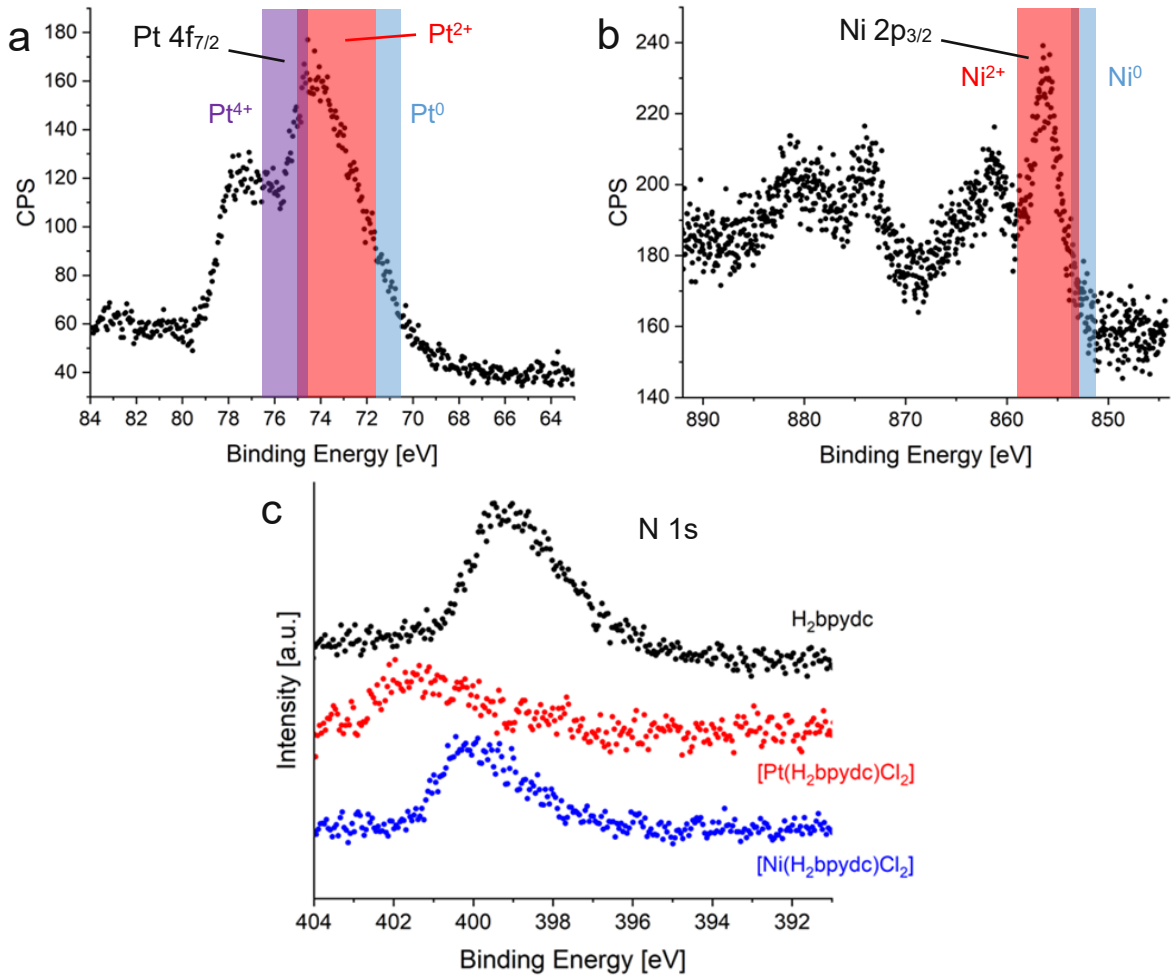

Figure 15: XPS spectra of (a) the Pt 4f region of Pt ligand (Pt-bpydc-2), (b) the Ni 2p region of Ni ligand (Ni-bpydc-2) and (c) the N 1s region of the non-functionalized H_2bpydc, Pt ligand and Ni ligand

The results from XPS, ^{1}H NMR and TXRF analysis in combination with the red-brown color of Pt ligand highly suggest that the intended structure, as shown in Figure 9a, was obtained. The situation was less clear for Ni ligand due to low Cl loadings and DRS spectra suggesting the presence of an octahedral complex. In order to address this, it was tried to grow single crystals of Ni ligand to perform single-crystal XRD. However, solvothermal recrystallization in ethanol or DMF as well as slow solvent evaporation from a solution in 0.3 M KOH (the latter to obtain the potassium salt of the complex) did not yield large enough crystals. Nevertheless, XPS and ^{1}H NMR results indicate the formation of some Ni complex with H_2bpydc which is in principle everything that is needed for the following MOF syntheses. As the exact structure of Ni ligand remains unclear, further calculations were performed assuming the intended structure of Ni ligand as shown in Figure 9b.

6.2 UiO-67-based MOFs

6.2.1 Influence of the Cocatalyst

The incorporation of small amounts of Pt ligand or Ni ligand into the UiO-67 framework didn´t affect its overall structure. This can be seen from the XRD diffractogram of UiO-67 remaining almost unchanged upon introduction of either metalloligand, as shown in Figure 16a. The FTIR spectrum of UiO-67 also didn´t change if Pt ligand or Ni ligand was present (see Figure 16b), as the amount of functionalized linker in the MOF is low. The spectrum contains the asymmetric and symmetric OCO stretching vibrations of the carboxylate groups at 1593 and 1409 cm^{-1}, respectively, the CC stretching vibration of the aromatic ring at 1504 cm^{-1}, the collective mode of the bpdc linker at 1180 cm^{-1}, combination bands of the bpdc linker as well as Zr-μ_3-O stretching between 670 and 770 cm^{-1}, and the Zr-μ_3-OH stretching vibration at 456 cm^{-1}.[73] It does not contain the C=O band of the free ligand´s carboxylic groups at 1674 cm^{-1}, proving the absence of significant amounts of uncoordinated H_2bpdc.

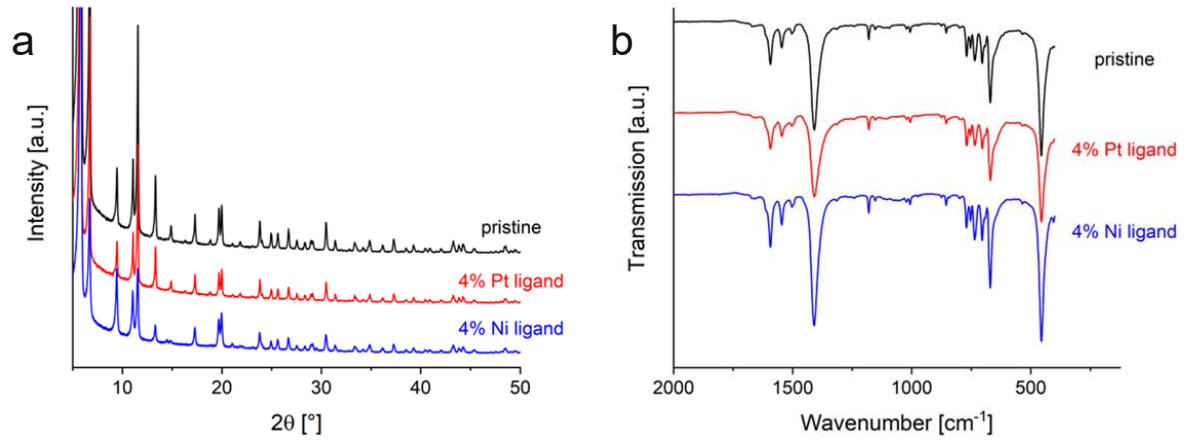

Figure 16: (a) XRD diffractograms of pristine UiO-67 (UiO-67-1) and UiO-67 where 4 % bpdc is exchanged with Pt ligand (UiO-67-4Pt) or Ni ligand (UiO-67-4Ni), obtained by one-pot synthesis and (b) FTIR spectra of the same samples

When Hou et al. reported their functionalization of UiO-67 with the very same Pt ligand as in this thesis, they observed an absorption feature around 410 nm which was ascribed to metal-to-ligand charge transfer (Pt(d_π) to bpydc(π^*)).[53] UV/Vis DRS therefore provides an effective method to proof the integrity of Pt ligand after incorporation into the MOF. Such a feature was indeed found at 405 nm for Pt-functionalized MOFs (see Figure 17a), and it increased in intensity with increasing amount of Pt ligand. In addition to that peak, there was also a shoulder evolving around 340 nm, which could originate for example from Pt states or defects introducing electronic states close to the conduction band. The former would be a desired phenomenon, as it could mean that Pt extracts excited electrons, leading them directly to the active sites for hydrogen evolution from water. The incorporation of Ni ligand into UiO-67 did not lead to any new features compared to the pristine MOF.

The DRS spectra were also used to determine the band gap of synthesized MOFs. Generally, this can be done via the Tauc function $(\alpha \cdot h\nu)^{1/\gamma}$, where α is the absorption coefficient, $h\nu$ is the photon energy and γ is a factor that equals ½ for direct semiconductors and 2 for indirect semiconductors. For UiO-67, the factor of ½ for direct semiconductors needs to be used.[74,75] The absorption coefficient α can be exchanged with the Kubelka-Munk function:

$$F(R_\infty) = \frac{(1 - R_\infty)^2}{2 \cdot R_\infty} \tag{3}$$

Here, R_∞ is the reflectance of a sample (ideally infinitely thick) relative to a standard. This way, the Tauc function can be calculated from the measured reflectance and extrapolating the slope of the Tauc function in the absorption edge to the abscissa gives the band gap value of the material. This method, however, is not applicable anymore for materials with significant absorption below the band gap energy, which is the case for UiO-67-based samples containing Pt ligand. A possible workaround for such materials is intersecting a linear fit of the Tauc function in the absorption edge with a linear fit of the Tauc function before the absorption edge. The energy value where the two fits cross gives a good estimation for the band gap energy.[76] An example for determining the band gap of a sample this way is given in Figure 33b in the appendix. Depending on the presence of electronic states in the band gap, the band gap energies of the samples were determined by the just explained method or the conventional Tauc method (extrapolating a linear fit of the Tauc function in the absorption edge to the abscissa). Due to the fact that two different methods were used here, the resulting band gap energies should be considered estimations rather than exact values. The determined band gaps for UiO-67-based MOFs with increasing content of bpydc, Pt ligand or Ni ligand are plotted in Figure 17b. Pristine UiO-67 exhibited a band gap energy of 3.81 eV. This decreased slightly for mixed-ligand UiO-67 with increasing content of bpydc as linker. A similar trend seemed to occur for increasing content of Pt ligand. For Ni ligand, the trend was not that clear.

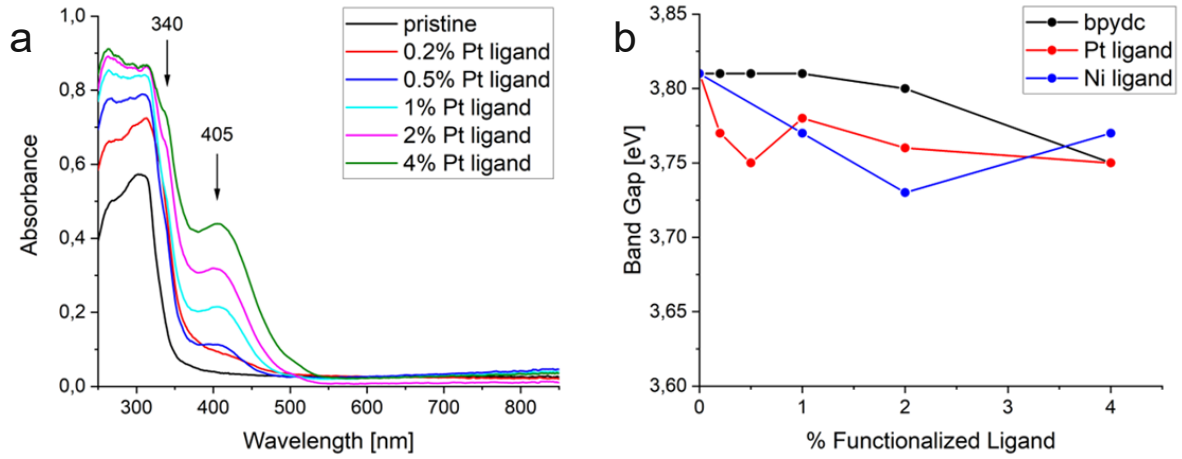

Figure 17: (a) UV/Vis DRS spectra of pristine UiO-67 (UiO-67-1) and UiO-67 with increasing mol-% Pt ligand (UiO-67-0.2Pt-3, UiO-67-0.5Pt, UiO-67-1Pt, UiO-67-2Pt, UiO-67-4Pt) obtained by one-pot synthesis and (b) band gap plot of UiO-67 with increasing mol-% bpydc (UiO-67-1, UiO-67-0.2bpy, UiO-67-0.5bpy, UiO-67-1bpy-3, UiO-67-2bpy, UiO-67-4bpy), increasing mol-% Pt ligand (UiO-67-0.2Pt-3, UiO-67-0.5Pt, UiO-67-1Pt, UiO-67-2Pt, UiO-67-4Pt) and increasing mol-% Ni ligand (UiO-67-1Ni, UiO-67-2Ni, UiO-67-4Ni) obtained by one-pot synthesis

Photoexcited states of UiO-67 can undergo radiative recombination with the emission maximum reported to be around 390 nm.[77] Photoluminescence experiments were therefore performed to gain insights into the charge separation mechanism upon photoexcitation of Pt- and Ni-functionalized UiO-67. PL steady-state spectra acquired for UiO-67 in this thesis showed an emission maximum around 350 nm. The emission spectra for increasing amounts of bpydc, Pt ligand or Ni ligand are shown in Figure 18a, b and c, respectively. Partial exchange of the bpdc linkers with bpydc led to successive quenching of the fluorescence, accompanied by a red shift of the emission maximum up to around 380 nm for 4 % exchange. This shift has been attributed to the decreasing amount of bpdc.[77] When incorporating Pt ligand or Ni ligand instead of bpydc, the quenching effect was even stronger, with Pt ligand showing the largest decrease in intensity as can be seen when plotting the intensity of the emission maximum depending on the amount of second ligand (see Figure 18d). The aforementioned red shift of the emission maximum was however absent for both incorporation of Pt and Ni ligand.

A possible explanation for the appearance of that shift with increasing bpydc content, but its absence for incorporation of a metal-functionalized linker could be the introduction of new electronic states by the bpydc linker which lie close to the conduction band. The observed shift might then actually be the gradual disappearance of the initial peak and the emergence of a new one at a higher wavelength due to charge transfer to those new electronic states. Pt and Ni single sites might then be able to extract electrons from those bpydc-related states, leaving only the initial emission peak with low intensities. It should be noted that the spectra for 1 % bpydc and 0.2 % Pt ligand were acquired during different measurement sessions than the rest and therefore might look a bit different.

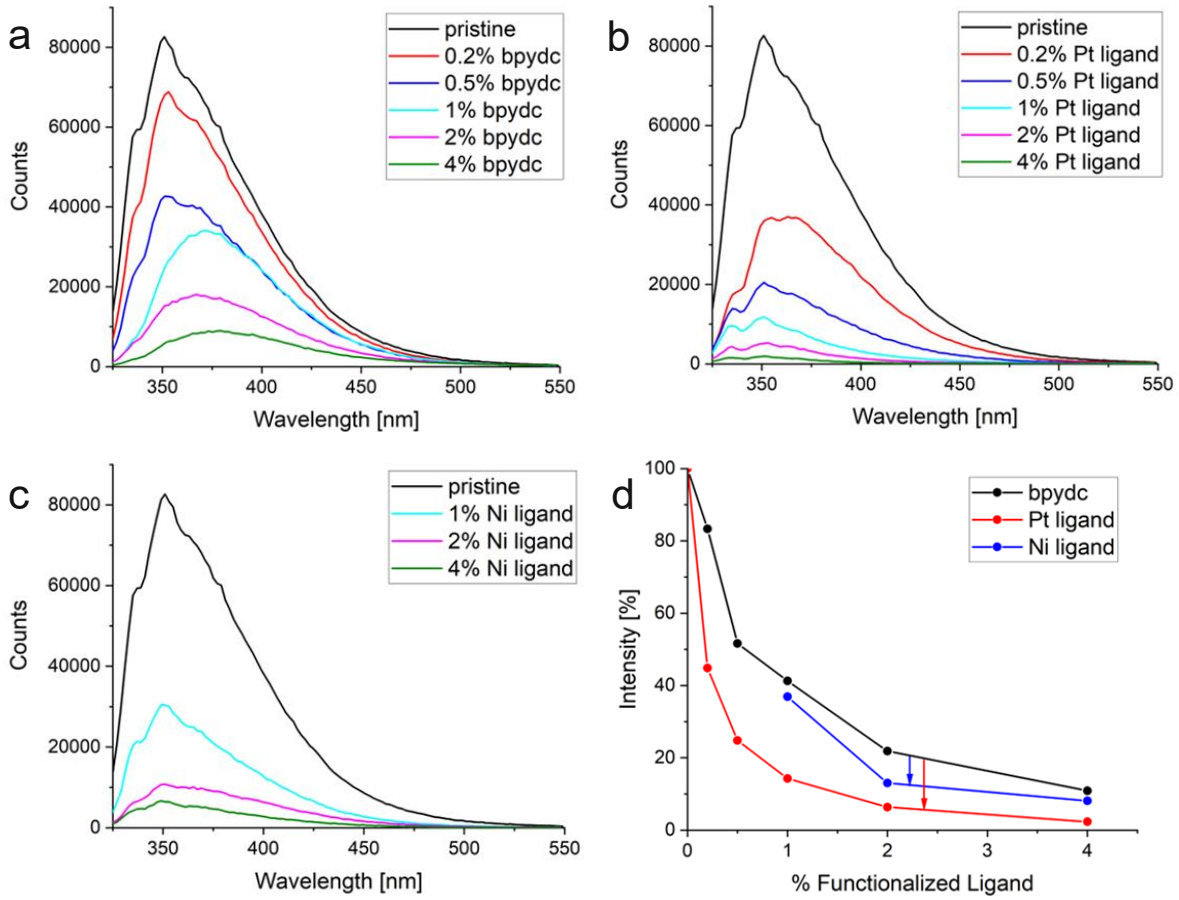

Figure 18: Steady-state PL spectra of pristine UiO-67 (UiO-67-1) compared with (a) increasing mol-% bpydc (UiO-67-0.2bpy, UiO-67-0.5bpy, UiO-67-1bpy-3, UiO-67-2bpy, UiO-67-4bpy), (b) increasing mol-% Pt ligand (UiO-67-0.2Pt-3, UiO-67-0.5Pt, UiO-67-1Pt, UiO-67-2Pt, UiO-67-4Pt) and (c) increasing mol-% Ni ligand (UiO-67-1Ni, UiO-67-2Ni, UiO-67-4Ni) obtained by one-pot synthesis and (d) decrease of the intensity at the emission maximum for the same samples

Time-resolved measurements were acquired at an emission wavelength of 400 nm and the photoluminescence decays were fitted using a biexponential function, as a monoexponential fit proved to be insufficient. The necessity of multiexponential functions has been ascribed to different microenvironments of the excited species.[77,78] It becomes evidently clear that more than a single exponential fit is needed when looking at the decay curve of UiO-67-based MOFs with higher loadings of Pt or Ni ligand (see Figure 19a). The short and long lifetimes (τ_1 and τ_2, respectively) for varying amounts of second linker are plotted in Figure 19b and c. For an increasing amount of Pt ligand or Ni ligand in the MOF structure, τ_1 is reduced significantly. A decrease in lifetime in combination with an emission intensity decrease is characteristic for dynamic quenching, meaning that the excited state forms without being hindered, but then interacts with a quencher resulting in deactivation to the ground state.[79] This is in good agreement with the hypothesis that Pt or Ni single sites take up the electrons after photoexcitation of the MOF. It should be noted that this dynamic quenching and therefore the decrease in fluorescence does not necessarily mean a decrease in recombination, since decay to the ground state can also take place by non-radiative deactivation. Increasing amounts of unfunctionalized bpydc did not lead to a decrease of τ_1 but rather the opposite,

highlighting that quenching by bpydc follows another mechanism as for Pt ligand and Ni ligand. The longer lifetime τ_2 changed less pronounced and with an inverse trend compared to τ_1 (slightly decreasing with bpydc, slightly increasing with Pt ligand or Ni ligand). Those longer lifetimes seem to correspond to excited states that are unavailable for electron transfer with the Pt or Ni single sites as already speculated by Hou et al.[53]

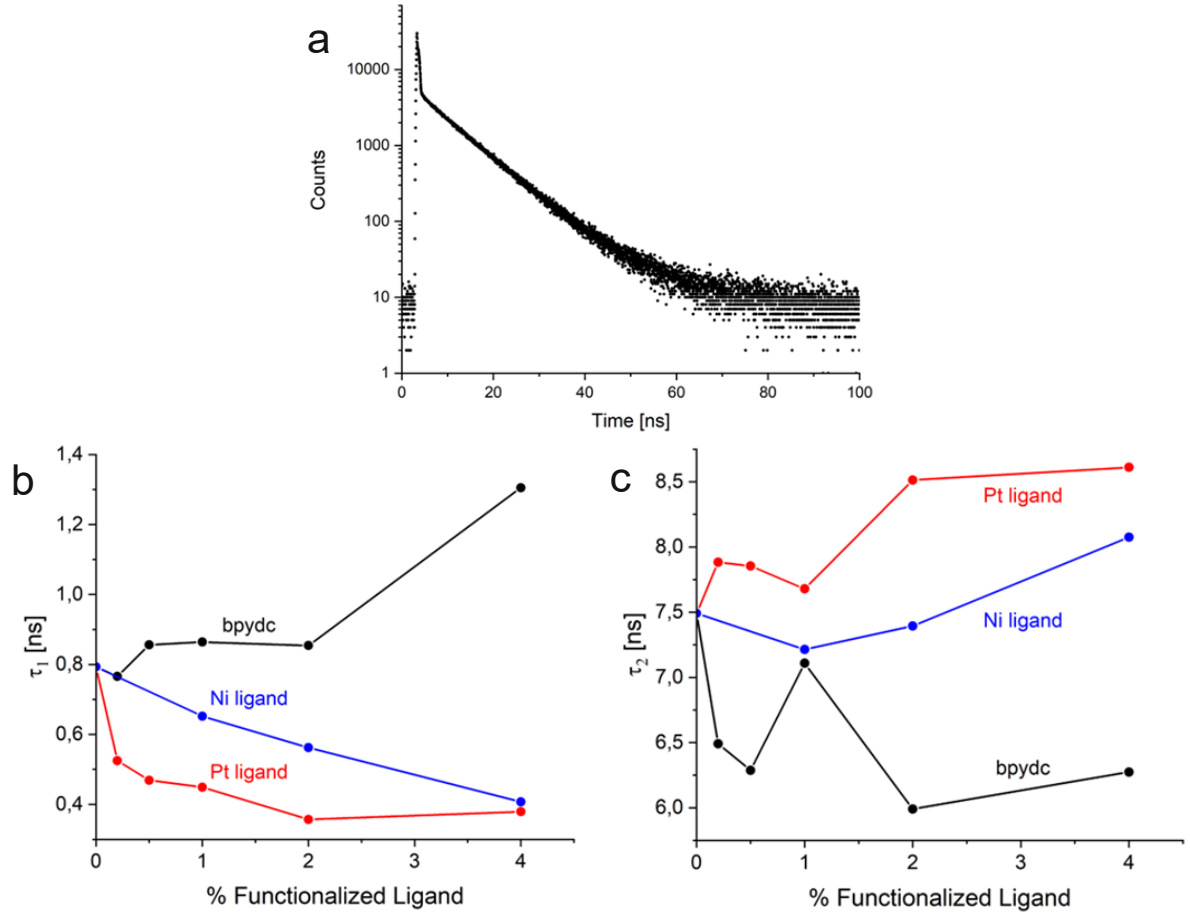

Figure 19: (a) Photoluminescence decay curve of UiO-67 where 4 % bpdc is exchanged with Pt ligand (UiO-67-4Pt) and changes in the (b) short and (c) long lifetime for increasing mol-% of bpydc (UiO-67-1, UiO-67-0.2bpy, UiO-67-0.5bpy, UiO-67-1bpy-3, UiO-67-2bpy, UiO-67-4bpy), Pt ligand (UiO-67-0.2Pt-3, UiO-67-0.5Pt, UiO-67-1Pt, UiO-67-2Pt, UiO-67-4Pt) and Ni ligand (UiO-67-1Ni, UiO-67-2Ni, UiO-67-4Ni), all obtained by one-pot synthesis

Pt and Ni loadings of the synthesized MOFs were determined with TXRF and were in relatively good agreement with theoretical values. They will be shown later in Figure 24 when discussing the TGA data, as TGA enabled refining of the TXRF data. To analyze the catalytic activity of synthesized samples, hydrogen evolution experiments under UV illumination were performed and compared to suitable references with photodeposited Pt or Ni. A suitable reference was considered a UiO-67-based MOF with the same molar amount of bpydc as Pt ligand or Ni ligand in the to be compared MOF. The chosen precursors for photodeposition were H_2PtCl_6 for Pt[80] and $NiCl_2$ for Ni.[81,82] The precursors were used in appropriate concentrations, so that the resulting Pt or Ni loading would match the one of the to be compared MOF. The results of these photocatalytic tests for various Pt or Ni loadings are summarized in Figure 20a and b.

UiO-67 itself without any cocatalyst proved to be an active photocatalyst with 0.34 µmol H_2/mg catalyst formed after 60 min. The presence of Pt sites led to a steep increase in activity for already small loadings, with the activity peaking around 0.25 wt-% Pt for both single sites and photodeposition. At higher loadings, the amount of formed H_2 decreased again, which in the case of photodeposition is expected because more Pt will most likely also result in larger nanoparticles, which take up electrons, but can only form hydrogen if the electron is located at the nanoparticle surface. For Pt single sites, the decrease for loadings above 0.25 wt-% could be attributed to different factors. One relevant effect is definitely the increasing amount of bpydc that is anchoring the Pt sites. UiO-67 with 4 % of the bpdc linkers exchanged with bpydc and photodeposition of 2 wt-% Pt has only approximately half the HER activity of pristine UiO-67 with 2 wt-% Pt photodeposition. Another effect possibly playing a role is the expected decrease in accessible pore volume due to the bulky nature of the metalloligand.[29,52,53] Unfortunately, adequate techniques to determine the pore volume of the synthesized MOFs like Brunauer-Emmett-Teller (BET) analysis would have gone beyond the scope of this thesis. The dependence of the photocatalytic activity on the Ni loading was far less pronounced than for Pt. Already a small loading of 0.15 wt-% Ni single sites led to an increase of the HER activity after 60 min by a factor of 2.3. A strong decrease at higher loadings like for Pt was not observed, possibly because the Ni loading was generally smaller than the Pt loading due to the lower molar mass of Ni. An interesting observation was a strong activation effect for higher Ni loadings for both single sites and photodeposition. While the amount of formed H_2 after 30 min was very low for 0.6 wt-% Ni, even lower than for UiO-67 without any Ni, the amount of H_2 after 60 min was more than 4 times the one after 30 min. For photodeposition, this might stem from Ni nanoparticles taking time to form. A report on photocatalytic water splitting with MO_x cocatalysts on TiO_2 nanoparticles showed that illumination of NiO_x-TiO_2 slowly led to photoreduction of Ni^{2+} to Ni^0 which resulted in continuous activation of the catalyst.[83] Whether a similar effect takes place for Ni single sites remains unclear. Overall, MOFs with Pt or Ni single sites as cocatalyst were more active for photocatalytic HER than their counterparts with photodeposition. Unsurprisingly, Pt turned out to be a better cocatalyst than Ni, but being worse by only a factor of 3 can be considered a success for an earth-abundant element like Ni.

So far, the metal single sites were always considered to be the active species for the reduction reaction. However, the possibility of them functioning as oxidation catalyst for MeOH should not automatically be discarded, as the acceleration of the other half reaction would also increase H_2 production. To clarify their role in the reaction, some UiO-67-based MOFs containing Pt or Ni single sites were additionally combined with 2 wt-% Pt nanoparticles introduced by photodeposition. If the single sites worked as an oxidation catalyst, the addition

of HER active Pt nanoparticles would further increase the amount of formed H_2. In fact, the opposite effect was observed, with the amount of produced H_2 decreasing strongly for additional photodeposition (see Figure 20c). This rather suggests that both metal single sites and Pt nanoparticles act as proton reduction catalyst and the existence of both leads to competitive charge carrier extraction between the two. Since Pt nanoparticles in such large amounts are less active than Pt or Ni single sites, they reduce the overall catalytic activity by taking electrons away from more active sites. Combining these results from the HER activity evaluation and the results from PL, the following reaction mechanism seems plausible for UiO-67 containing Pt or Ni single sites. The bpdc linkers absorb radiation of the suitable wavelength, followed by the electrons being transferred to the inorganic nodes by LMCT, while the holes stay at the bpdc linkers where they will be scavenged by MeOH. The electrons travel through the framework to a Pt ligand or Ni ligand where they stay and can react with H_2O molecules to form H_2.

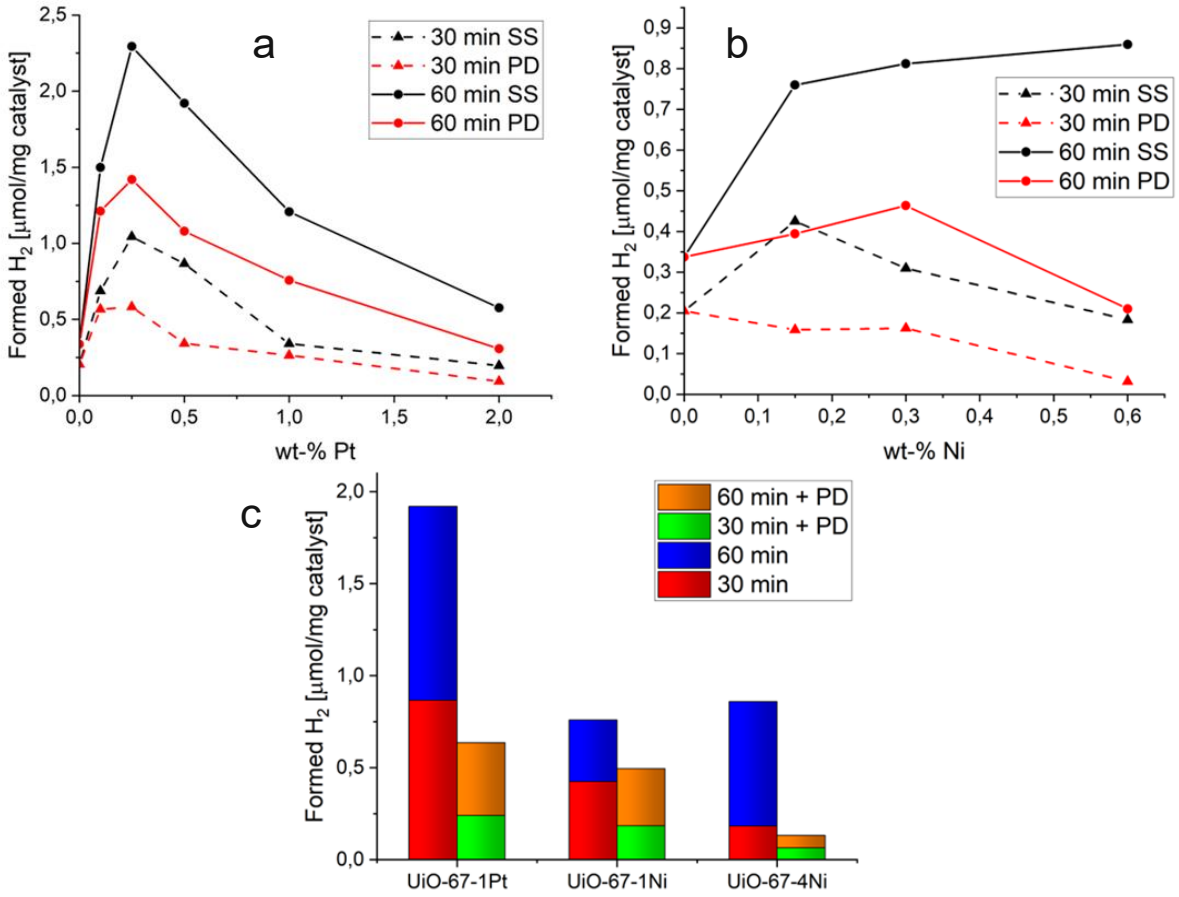

Figure 20: Amounts of formed H_2 comparing single sites and photodeposition of (a) Pt and (b) Ni for various loadings after 30 and 60 min illumination (samples: mean of UiO-67-1 and UiO-67-2, UiO-67-0.2bpy, UiO-67-0.5bpy, UiO-67-1bpy-3, UiO-67-2bpy, UiO-67-4bpy, UiO-67-0.2Pt-3, UiO-67-0.5Pt, UiO-67-1Pt, UiO-67-2Pt, UiO-67-4Pt, UiO-6-1Ni, UiO-67-2Ni, UiO-67-4Ni) and (c) amounts of formed H_2 for selected UiO-67-based single-site catalysts with and without additional photodeposition of 2 wt-% Pt after 30 and 60 min illumination

6.2.2 Influence of the Synthesis Method

So far, all results were presented for UiO-67-based MOFs obtained by one-pot synthesis. Many of the described phenomena also occurred for samples obtained by post-synthetic ligand exchange, but there were also a lot of differences that will be discussed in this chapter. Like one-pot synthesis, the introduction of single-sites via ligand-exchange did not change the FTIR spectra or XRD diffractograms of UiO-67 (for successful batches). DRS spectra also showed the feature at 405 nm of metal-to-ligand charge transfer when Pt ligand was introduced via ligand exchange (see Figure 21a). One possible difference between samples obtained by one-pot synthesis and ligand exchange may be a slightly different band gap. While one-pot synthesis led to a band gap decrease from 3.81 eV to 3.75 or 3.77 eV for 4 % exchanged Pt ligand or Ni ligand, respectively, the determined band gap for comparable samples after ligand exchange was around 3.85 eV. However, it again needs to be considered that the presence of intra-band gap states reduces the accuracy of the Tauc method and the determined band gap values should be treated with caution. Another observation for samples where ligand exchange was applied was a shoulder in the absorption edge around 330 nm in many cases. While a similar shoulder around 340 nm did already appear for MOFs containing Pt ligand, such features were not seen for samples containing Ni ligand obtained by one-pot synthesis as shown in Figure 21b. This may indicate that ligand exchange introduced additional electronic states close to the conduction band.

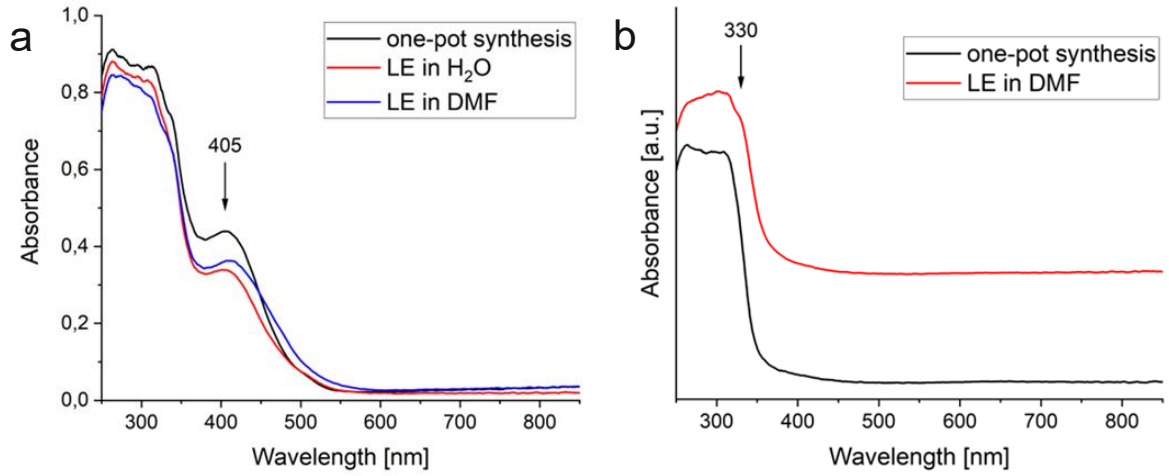

Figure 21: (a) UV/Vis DRS spectra of UiO-67 with 4 % bpdc exchanged with Pt ligand, obtained either via one-pot synthesis or ligand exchange (LE, samples: UiO-67-4Pt, UiO-67-4Pt-LE, UiO-67-4Pt-LE-4) and (b) offset UV/Vis DRS spectra of UiO-67 with 4 % bpdc exchanged with Ni ligand by one-pot synthesis or ligand exchange (LE), indicating intra-band gap states in the case of ligand exchange (samples: UiO-67-4Ni, UiO-67-4Ni-LE-5)

The phenomenon of new electronic states in the band gap was further elucidated by steady-state PL measurements. Ligand exchange with both Pt ligand and Ni ligand caused a strong shift of the emission maximum from around 350 nm to around 380 nm as well as a drastic intensity increase compared to one-pot synthesis, which is displayed in Figure 22a and b, for Pt and Ni ligand, respectively. The emission intensity was higher for ligand exchange in DMF

compared to water while the position of the maximum seemed independent from the reaction medium. These results highlight two things. First, there were indeed new electronic states close to the conduction band introduced by ligand exchange, which led to an emission maximum at higher wavelengths. Second, radiative recombination of electron-hole pairs can take place from these states and incorporated Pt or Ni single sites were not able to quench this process as well as for samples prepared by one-pot synthesis. The new electronic states can therefore be labeled as trap states.

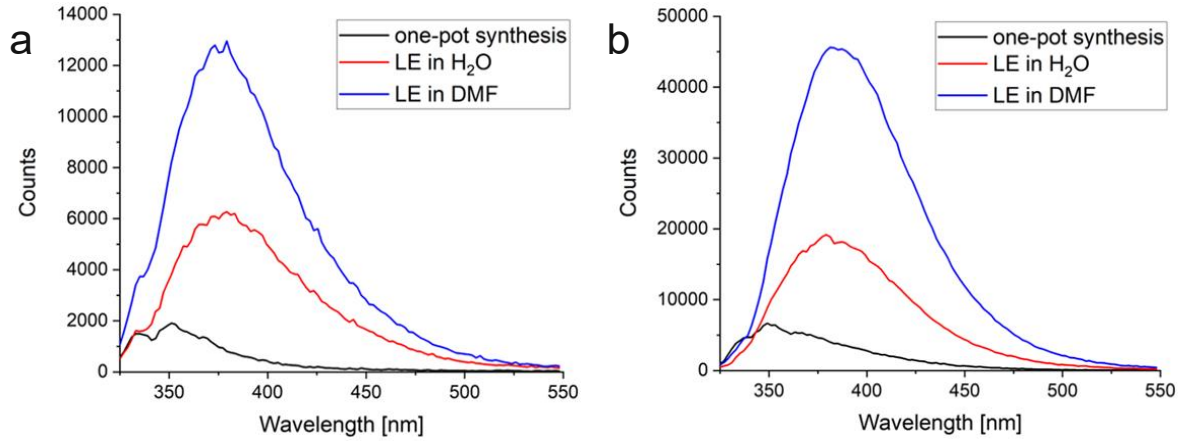

Figure 22: Steady-state PL spectra of UiO-67 with 4 % bpdc exchanged with (a) Pt ligand (UiO-67-4Pt, UiO-67-4Pt-LE, UiO-67-4Pt-LE-4) or (b) Ni ligand (UiO-67-4Ni, UiO-67-4Ni-LE-3, UiO-67-4Ni-LE-5), obtained either via one-pot synthesis or ligand exchange (LE)

As XRD diffractograms were seemingly not affected, the overall crystallinity of such MOFs was not decreased by the ligand exchange procedure. Small amounts of certain defects, however, do not necessarily have to decrease crystallinity and might introduce the observed trap states. A typical type of defects for MOFs in general are missing ligand defects, which in the case of UiO-type MOFs lead to open Zr sites at the nodes.[35] An accomplished method for detecting and quantifying missing ligand defects is TGA. TGA experiments of interesting samples were performed in N_2 and synthetic air atmosphere, whereas only the latter enabled reliable quantification, as the chemical composition of the residue after heating in N_2 is hard to predict. The initial sample composition was assumed to be $Zr_6O_6(bpdc_{1-y}L_y)_{6\cdot(1-x)}$, where the second ligand L constituted either bpydc, Pt ligand or Ni ligand, y being the fraction of the second ligand and x being the fraction of missing ligands. The assumed residue after temperature treatment in air was 6 ZrO_2 [35] and potentially 6·(1-x)·y Pt [84] or NiO. For the initial structure, the dehydroxylated state of UiO-67 is taken, because this one is formed at lower temperatures than the ligand removal.[35] An example of a TGA curve including the temperature limits for which the weight loss was calculated is shown in Figure 23a. The TGA results revealed that the introduction of Pt ligand or Ni ligand reduced the thermal stability of UiO-67, as can be seen in Figure 23b, with the stability loss being more pronounced for Pt ligand. The decomposition temperature was not noticeably affected by the synthesis method. More

importantly, the TGA results proved that post-synthetic ligand exchange indeed introduced missing ligand defects. Pristine UiO-67, the way it was synthesized in this thesis, already had 20 % ligands missing, but this value increased to up to 34 % for ligand exchange with Pt ligand in water. Samples containing Ni ligand exhibited fewer missing ligand defects than Pt-functionalized UiO-67, but samples obtained by ligand exchange again exhibited more missing ligand defects than samples obtained by one-pot synthesis. The exact results are listed in Table 3.

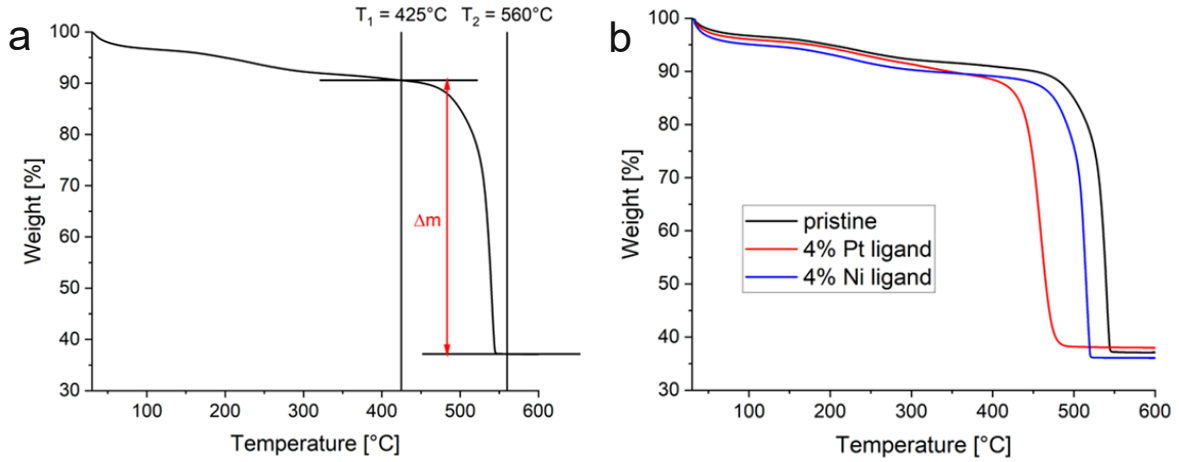

Figure 23: TGA curves for (a) pristine UiO-67 (UiO-67-5) showing the temperature limits for the weight loss calculation and (b) pristine UiO-67 (UiO-67-5) compared to UiO-67 with 4 % bpdc exchanged with Pt ligand (UiO-67-4Pt) or Ni ligand (UiO-67-4Ni), obtained by one-pot synthesis

Table 3: Determined amounts of missing ligands for UiO-67-based samples from TGA

Sample	Description	% Missing Ligands
UiO-67-5	Pristine UiO-67	20
UiO-67-4bpy	4 % bpydc One-pot synthesis	22
UiO-67-4Pt	4 % Pt ligand One-pot synthesis	22
UiO-67-4Pt-LE	4 % Pt ligand Ligand exchange in H_2O	34
UiO-67-4Pt-LE-4	4 % Pt ligand Ligand exchange in DMF	29
UiO-67-4Ni	4 % Ni ligand One-pot synthesis	17
UiO-67-4Ni-LE-3	4 % Ni ligand Ligand exchange in H_2O	22
UiO-67-4Ni-LE-5	4 % Ni ligand Ligand exchange in DMF	24

The TGA results were used to refine the Pt and Ni loadings obtained by TXRF. Because the fraction of present bpdc linkers that are exchanged with functionalized linkers is expected to be unchanged, missing ligands lower the expected Pt or Ni loading, due to the overall amount of linkers decreasing. Missing ligand defects also increase the Zr content of the MOF, which is needed to calculate the cocatalyst loading, as TXRF actually determined the ratio of Zr and Pt or Ni. The correction of TXRF data was performed using the determined amount of missing ligands or by making an educated guess based on the TGA results, which was 20 % missing ligands for samples prepared by one-pot synthesis. For the sample with the lowest Ni loading (UiO-67-1Ni, 0.15 wt-% Ni expected), quantification of Ni was not possible, however, overall, the determined Pt and Ni loadings were in relatively good agreement with calculated values, as can be seen in Figure 24a, b and c. Interestingly, post-synthetic ligand exchange with Pt ligand led to even higher Pt loadings than expected (see Figure 24b). Ligand exchange in MOFs is considered to be facilitated by polar solvents and water would be expected to lead to more incorporation of the second ligand.[52] This effect could not be observed here, as the use of both solvents resulted in cocatalyst loadings close to the intended values.

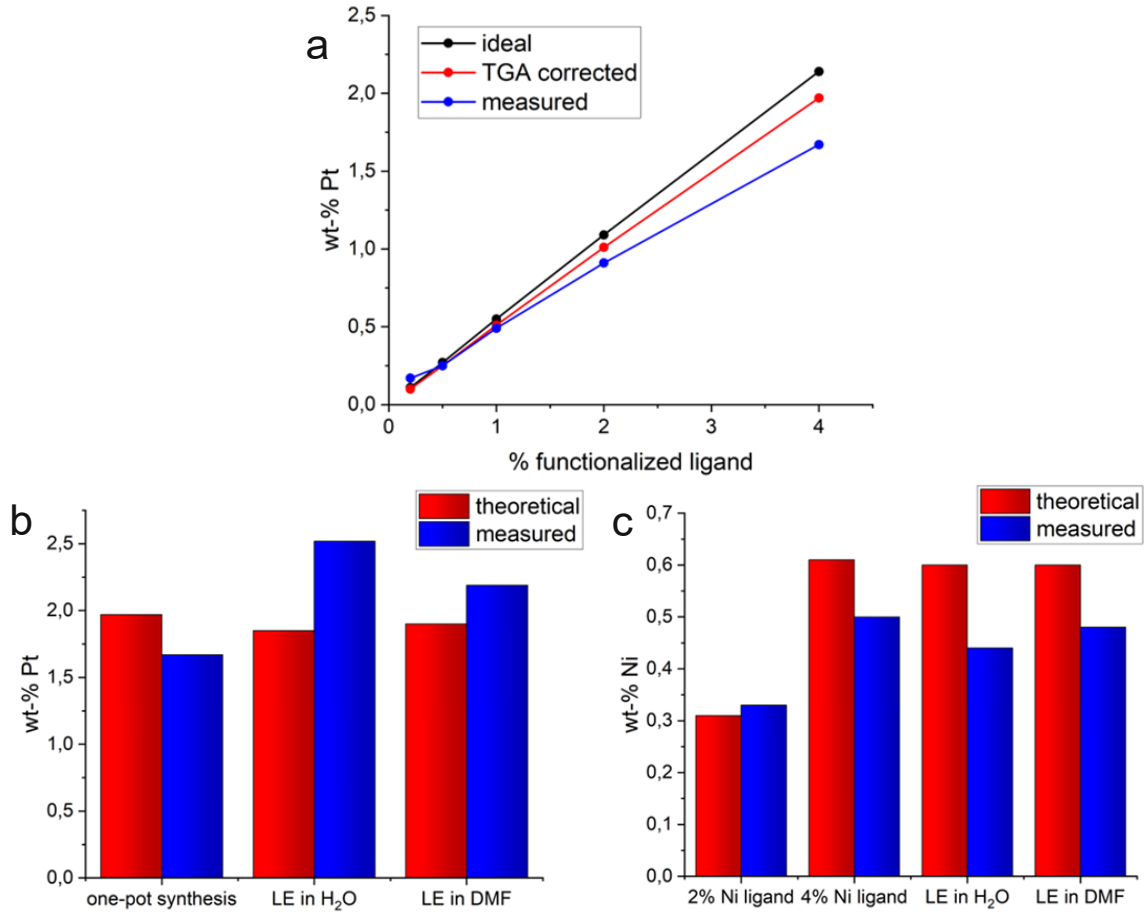

Figure 24: (a) Pt loadings as measured by TXRF of UiO-67 with increasing mol-% Pt ligand, obtained by one-pot synthesis (UiO-0.2Pt-3, UiO-67-0.5Pt, UiO-67-1Pt, UiO-67-2Pt, UiO-67-4Pt; Zr content corrected by TGA) compared to the theoretical Pt loadings of a defect-free (ideal) structure and the theoretical loadings corrected by TGA; cocatalyst loadings as measured by TXRF of UiO-67 with (b) 4 % bpdc exchanged with Pt ligand or (c) 2 or 4% bpdc exchanged with Ni ligand, obtained either via one-pot synthesis (UiO-67-4Pt, 2% Ni ligand: UiO-67-2Ni, 4% Ni ligand: UiO-67-4Ni) or ligand exchange (LE, samples: UiO-67-4Pt-LE, UiO-67-4Pt-LE-4, UiO-67-4Ni-LE-3, UiO-67-4Ni-LE-5) where the Zr content was corrected by TGA compared to the theoretical loadings corrected by TGA

After unraveling the formation of missing ligand defects and possibly related trap states, their effect on the catalytic properties becomes of high interest. The amounts of formed H_2 after 30 and 60 min illumination for samples prepared by ligand exchange are compared to samples prepared by one-pot synthesis and photodeposition of the cocatalyst in Figure 25a and b, for Pt and Ni as cocatalyst, respectively. Generally, it can be said that ligand exchange seemed to reduce the HER activity compared to samples obtained by one-pot synthesis. Ligand exchange in water yielded only low amounts of H_2 that were similar or even worse than for suitable references with photodeposition of the cocatalyst, while ligand exchange in DMF resulted in higher activities compared to that. In the case of the incorporation of Ni ligand by ligand exchange in DMF, the HER activity was still lower than for a corresponding sample prepared by one-pot synthesis. Interestingly, the amount of H_2 formed by UiO-67 with 4 % bpdc exchanged with Pt ligand was almost the same for both one-pot synthesis and ligand exchange in DMF. This was unexpected, because PL showed more radiative recombination and Pt loadings were even higher for ligand exchange in DMF, which at such high loadings is

expected to result in lower activity as shown in chapter 6.2.1. It has been reported that missing ligand defects in UiO-67 can be beneficial for charge separation and reduce recombination due to induced trap states.[85] While this might be possible, the PL results highlight that the cocatalyst single sites are seemingly not able to extract those trapped electrons sufficiently, so a beneficial effect for catalytic activity due to the trap states seems unlikely. A possible explanation could be a different local distribution of the functionalized linker in the MOF crystals. For example, if ligand exchange preferably leads to surface functionalization of the crystals, the inside of the crystals will have a lower concentration of the bulky metalloligand, which could increase pore accessibility and catalytic activity. As ligand exchange in MOFs is reported to be facilitated by polar solvents [52] and DMF is less polar than water, ligand exchange in DMF could even enhance this effect compared to water, possibly explaining the better resulting catalytic activity. Another possible explanation for the different activity depending on the solvent during synthesis could be the stability of the functionalized linkers in water. At least for Ni ligand, FTIR results and an irreversible color change indicated that water stability is an issue as discussed in chapter 6.1.

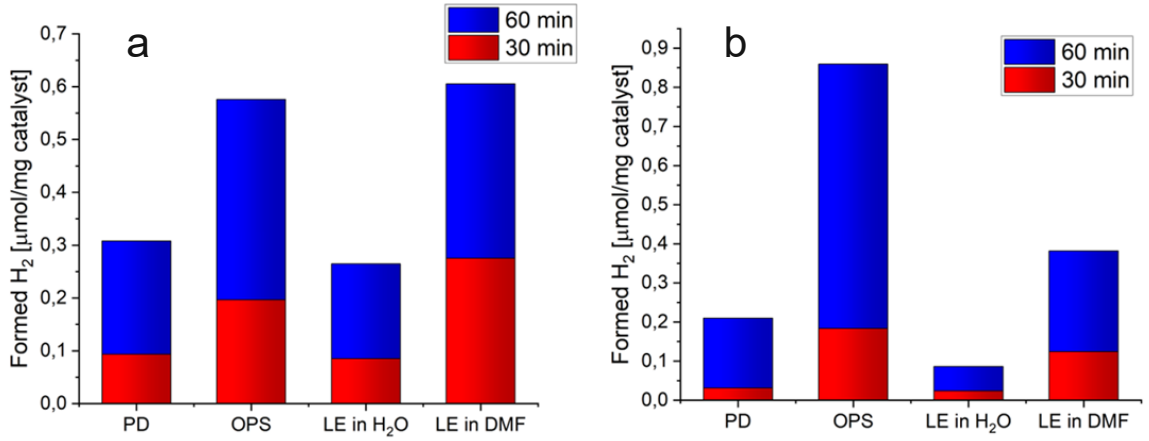

Figure 25: Amounts of formed H_2 after 30 and 60 min illumination for UiO-67 with 4 % bpdc exchanged with (a) Pt ligand (UiO-67-4Pt, UiO-67-4Pt-LE, UiO-67-4Pt-LE-4) or (b) Ni ligand (UiO-67-4Ni, UiO-67-4Ni-LE-3, UiO-67-4Ni-LE-5), obtained either via one-pot synthesis (OPS) or ligand exchange (LE), compared to UiO-67 with 4 % bpdc exchanged with bpydc (UiO-67-4bpy) and photodeposition (PD) of the same amount of cocatalyst as the to be compared samples (2 wt-% Pt or 0.6 wt-% Ni)

6.3 COK-47-based MOFs

The previous chapter dealt with the well-studied MOF UiO-67, where the introduction of metal single-sites has been reported multiple times. In this section, the application of this concept to the lesser-known COK-47 will be discussed, for which functionalization with single sites has only been reported recently.[51] The version of COK-47 mainly used in this thesis has previously been developed in the group and was labeled COK-47_{ISO}.[62] When the term COK-47 is used in the following without any subscript, it refers to COK-47_{ISO}.

6.3.1 One-Pot Synthesis

Previous studies in the group found a reaction temperature of 150°C to yield good results for microwave synthesis of COK-47.[62] When the same procedure was applied to the synthesis of COK-47 with parts of Pt ligand, the organometallic complex decomposed and Pt nanoparticles were produced. This becomes evident from the XRD diffractograms (see Figure 26a) with peaks at 2θ values of 40° and 46°, corresponding to Pt(111) and Pt(200) diffractions, demonstrating the presence of Pt nanoparticles.[86] The nanoparticle formation also led to Pt loadings 2-3 times higher than the targeted due to nanoparticles also being formed from excess ligand (see Figure 26b). An adaption of the synthesis procedure by lowering the temperature to 120°C and reducing the amount of excess ligand prevented the decomposition of Pt ligand, proven by the absence of the Pt peaks in XRD. This is also reflected by the TXRF results of samples obtained by the adapted synthesis procedure, with Pt loadings, while still slightly too high, matching quite well with calculated values. The color of synthesized samples was affected as well, as ones with Pt nanoparticles were dark grey and samples obtained at 120°C were yellow, corresponding more to the expected color. COK-47 containing Ni ligand never showed any XRD peaks of Ni nanoparticles which would be expected to lie at 45° and 52°,[87] neither for the high nor for the low temperature synthesis. Interestingly however, the Ni loadings for both procedures where drastically higher than the expected ones (shown later in Figure 29c when comparing to ligand exchange), indicating that all Ni species were bound to the MOF structure and not just an aliquot of the deployed Ni ligand. Whether those Ni species were present as Ni ligand or in another form could not be clarified, but the presence of Ni nanoparticles can most likely be excluded. Besides preventing the formation of Pt nanoparticles, the low temperature synthesis also had another effect on COK-47, namely the intensity loss of XRD peaks for all samples (Pt ligand, Ni ligand or non-functionalized). This could either be attributed to a loss of crystallinity or to smaller crystallites, with the latter having been reported by Smolders et al.[43]

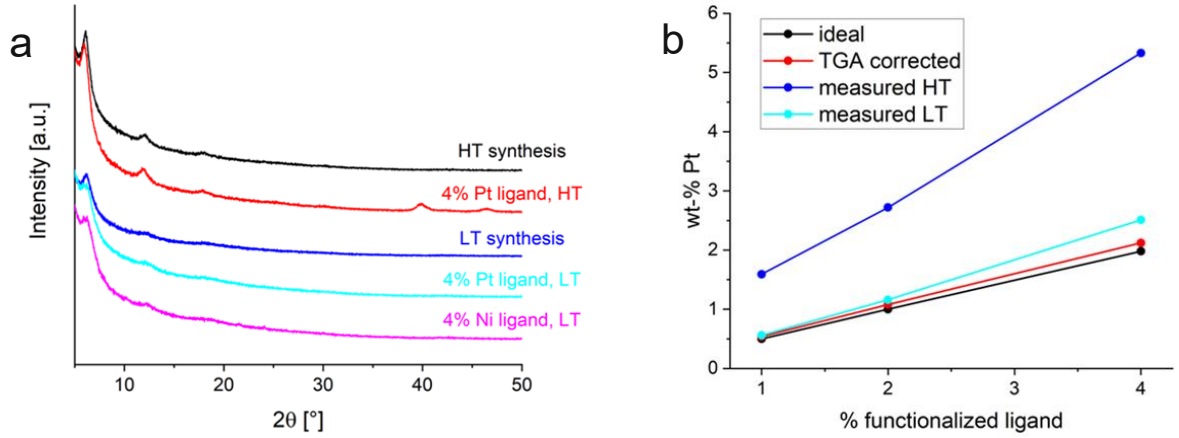

Figure 26: (a) XRD diffractograms of pristine COK-47 synthesized at 150°C (HT, COK-47-7) and 120°C (LT, COK-47-6) and COK-47 with 4 % bpdc exchanged with Pt ligand (COK-47-4Pt synthesized at 150°C, COK-47-4Pt-2 synthesized at 120°C) or Ni ligand (COK-47-4Ni-2 synthesized at 120°C); (b) Pt loadings as measured by TXRF of COK-47 with increasing mol-% Pt ligand, synthesized at 150°C (HT: COK-47-1Pt, COK-47-2Pt, COK-47-4Pt) or 120°C (LT: COK-47-1Pt-2, COK-47-2Pt-2, COK-47-4Pt-2) where the Ti content was corrected by TGA compared to the theoretical Pt loadings of the nominal (ideal) structure and the theoretical loadings corrected by TGA

As discussed in chapter 6.2.2 for UiO-67, TGA was used to quantify missing ligand defects of selected samples. The initial sample composition was assumed to be $Ti_2O_3(bpdc_{1-y}L_y)_{(1-x)}(OCH_3)_{2x}$,[43] with L being either bpydc, Pt ligand or Ni ligand, y being the fraction of the second ligand L and x being the fraction of missing ligands. The assumed residue after temperature treatment was TiO_2 and potentially (1-x)·y Pt or NiO. In contrary to the results for UiO-67-based MOFs, the introduction of Pt ligand or Ni ligand into COK-47 did not lead to a clear change of the decomposition temperature. An exemplary TGA curve is shown in Figure 27a. The calculations of the amounts of missing ligands yielded negative values, meaning that the MOFs actually contained excess ligands. A possible explanation for this is the small particle size of COK-47 and the crystallites being capped by ligands. The methoxy groups capping open Ti sites due to missing linkers were then omitted in the calculations and the determined amounts of excess ligands are listed in Table 4. It seems, that samples synthesized by the adapted procedure contained tendentially fewer ligands than ones synthesized by the original procedure. Whether this occured because of the lower reaction temperature or the smaller excess of ligands cannot be stated with certainty. For refining the TXRF data, 15 % excess ligands were assumed for samples where TGA was not measured. As it has already been the case for UiO-67, the presence of Pt ligand or Ni ligand did not change the FTIR spectrum of COK-47 (see Figure 27b). UV/Vis DRS spectra of Pt-functionalized COK-47 show a shoulder around 450 nm for increasing Pt loading as can be seen in Figure 27c, reminiscent of the metal-to-ligand charge transfer within Pt ligand in UiO-67 at 405 nm. Band gaps of the materials were determined with the adapted Tauc method explained in chapter 6.2.1. Batches of pristine COK-47 exhibited band gaps between 2.91 and 2.96 eV (with the exception of one batch: COK-47-1), significantly lower than UiO-67, explaining its photoactivity for illumination at 365 nm. Opposite to UiO-67, the band gap of

COK-47 seemed to increase with higher content of Pt ligand as shown in Figure 27d. The band gap of COK-47 with 4 % bpdc exchanged with Ni ligand (COK-47-4Ni-2) was with 2.99 eV higher than that of the pristine MOF as well, but when 4 % bpdc were exchanged with the unfunctionalized bpydc linker (COK-47-4bpy) the band gap decreased to 2.85 eV.

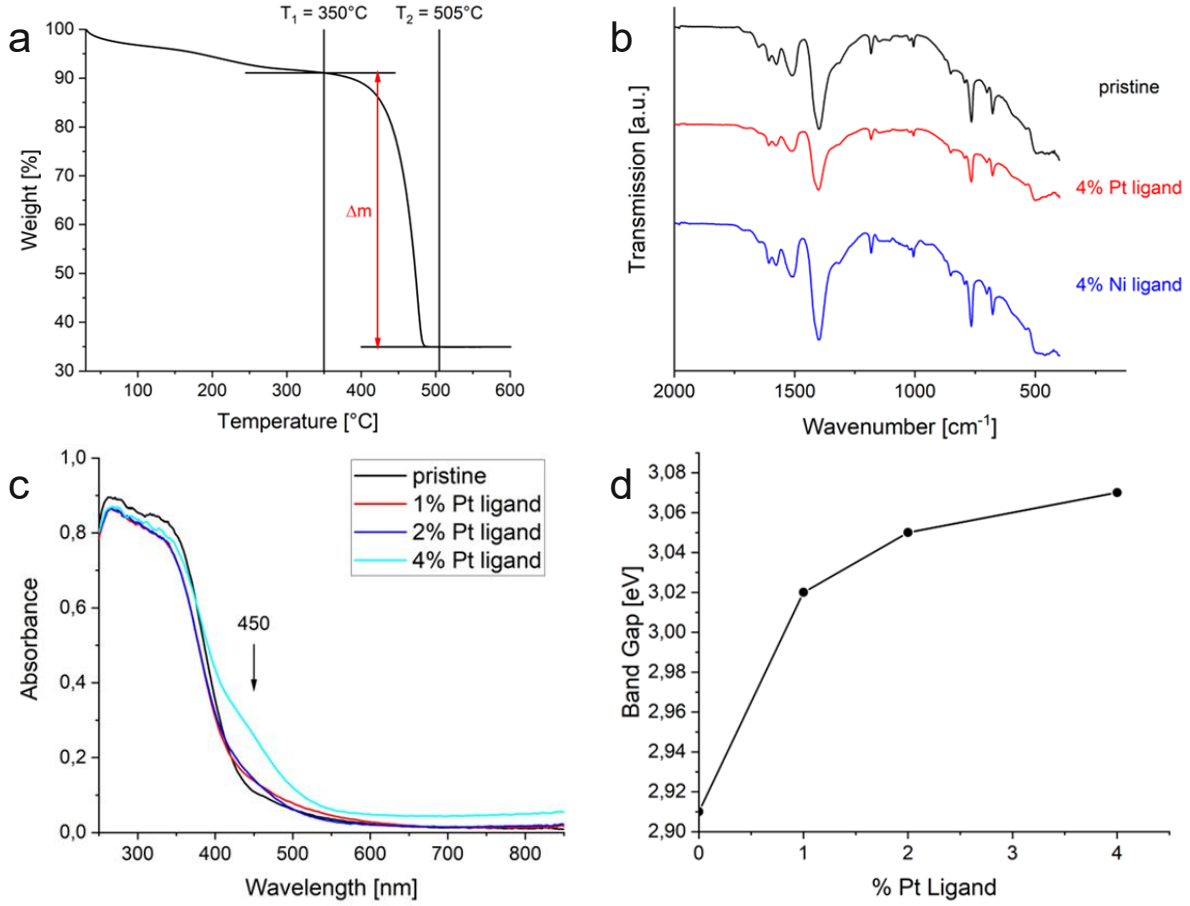

Figure 27: (a) TGA curve for pristine COK-47 (COK-47-5) showing the temperature limits for the weight loss calculation; (b) FTIR spectra of pristine COK-47 (COK-47-6) and COK-47 where 4 % bpdc is exchanged with Pt ligand (COK-47-4P-2t) or Ni ligand (COK-47-4Ni-2), all synthesized at 120°C; (c) UV/Vis DRS spectra and (d) band gaps of pristine COK-47 (COK-47-6) and COK-47 with increasing mol-% Pt ligand (COK-47-1Pt-2, COK-47-2Pt-2, COK-47-4Pt-2), all synthesized at 120°C

Table 4: Determined amounts of excess ligands for COK-47-based samples from TGA

Sample	Description	% Excess Ligands
COK-47-5	Pristine COK-47 150°C	14
COK-47-6	Pristine COK-47 120°C	6
COK-47-4bpy	4 % bpydc 150°C	19
COK-47-4Pt-2	4 % Pt ligand 120°C	15
COK-47-4Pt-LE-3	4 % Pt ligand Ligand exchange in DMF	1
COK-47-4Ni-2	4 % Ni ligand 120°C	7
COK-47-4Ni-LE-3	4 % Ni ligand Ligand exchange in DMF	1

The synthesized samples were again tested on their photocatalytic activity for hydrogen evolution from water. Because of the smaller band gap of COK-47 compared to UiO-67, a 365 nm LED could be used for illumination. COK-47 without any cocatalyst proved to be almost not active, which highlights the importance of a suitable cocatalyst. The combination of COK-47 with Ni seems to be incompatible for photocatalytic HER, as neither functionalization with Ni ligand, nor photodeposition of Ni nanoparticles from $NiCl_2$ solution yielded meaningful activity. The highest measured activity in that case was 0.09 µmol H_2/mg catalyst after 60 min illumination for the sample obtained by one-pot synthesis at 150°C with a very high Ni loading (COK-47-4Ni).

Photodeposition of Pt from H_2PtCl_6 solution onto COK-47 synthesized at 150°C gave excellent HER activity of around 10 µmol H_2/mg catalyst after 60 min illumination, while COK-47 synthesized at 120°C and less excess ligand already showed less than half of that. Pt single sites as cocatalyst were active as well, but H_2 formation rates weren´t able to compete with the ones after photodeposition. An obvious activity trend depending on the Pt loading could not be observed as can be seen in Figure 28a. The lower HER activity of COK-47 with Pt single sites can be correlated with another phenomenon, namely a color change of the catalyst suspension to dark grey upon illumination, which is ascribed to Ti^{3+} states [40] and also occurs for pristine COK-47, but is absent after photodeposition of Pt nanoparticles. The color change is reversible after shaking the suspension in air (see Figure 28c and d) and indicates that

electrons are trapped in the SBUs and cannot react with protons to form hydrogen. This highlights that the limiting factor of such COK-47-based catalysts with Pt single sites is not light absorption or charge separation, but rather the active sites themselves. Possibly they are mainly embedded within the crystallites and simply not available for protons, as COK-47 synthesized by the here applied method is non-porous.[62]

Additional photodeposition of 2 wt-% Pt onto single-site-functionalized samples regained catalytic activity. While the amounts of formed H_2 were still lower than for pristine COK-47 synthesized at 150°C and photodeposition of Pt, they exceeded the amounts for pristine COK-47 synthesized at 120°C and photodeposition of Pt (shown in Figure 28b), which should constitute a better reference for the single-site-functionalized samples. In the case of competitive charge carrier extraction, an activity in between the original single-site functionalized catalyst and the reference of pristine COK-47 with photodeposited Pt would be expected. If the higher activity does not stem from coincidental deviations from the syntheses, it could be a hint for Pt or Ni single sites potentially catalyzing methanol oxidation rather than proton reduction. This would explain the low activity of single-site functionalized COK-47 without Pt photodeposition, as methanol oxidation is not considered to be the bottleneck of the overall reaction, as well as the improved activity when combining single sites (as an oxidation catalyst) and photodeposited Pt nanoparticles (as a reduction catalyst). It should be noted, however, that the chosen reference catalyst only contained bpdc linkers. A linker composition of 96 % bpdc and 4 % bpydc would compare better to the single-site functionalized MOFs, but such a sample was not synthesized and activity evaluation of COK-47 synthesized at 150°C did not show a meaningful change in performance in the presence of 4 % bpydc which likely translates to synthesis at 120°C as well.

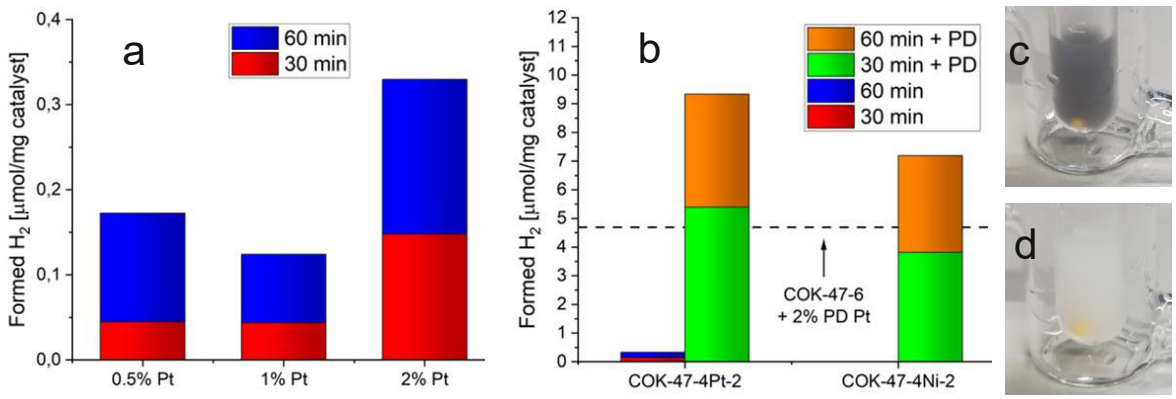

Figure 28: Amounts of formed H_2 after 30 and 60 min illumination for (a) COK-47 with increasing wt-% of Pt single sites, synthesized at 120°C (COK-47-1Pt-2, COK-47-2Pt-2, COK-47-4Pt-2) and (b) selected COK-47-based single-site catalysts with and without additional photodeposition of 2 wt-% Pt (activity of COK-47 without Pt ligand or Ni ligand, but with photodeposition of 2 wt-% Pt showed as dotted line); pictures of a sample suspension (COK-47-5) with trapped electrons (c) before and (d) after shaking in air

6.3.2 Post-Synthetic Ligand Exchange

The adaption of the synthesis procedure for one-pot synthesis of single-site functionalized COK-47 demonstrated that the ideal synthesis conditions for the MOF can be incompatible with the metalloligand, as a temperature of 150°C led to the formation of Pt nanoparticles. Post-synthetic ligand exchange could offer a possibility to combine the ideal conditions for the MOF synthesis with the introduction of any chosen metalloligand. Like for one-pot synthesis, FTIR spectra of COK-47 did not change when Pt ligand or Ni ligand were incorporated and XRD diffractograms of the pristine MOF were also not affected by the ligand exchange procedure (for successful batches, see Figure 31a later). The UV/Vis DRS feature around 450 nm emerged as well for COK-47 functionalized with Pt ligand (see Figure 29a).

A difference between one-pot synthesis and ligand exchange were the amounts of excess ligands measured by TGA (listed in Table 4 before). The results of COK-47-based MOFs after ligand exchange suggested an almost perfect framework without missing or excess ligands. However, considering the presence of excess ligands for other COK-47-based samples and the introduction of missing ligand defects by ligand exchange in UiO-67 imply that missing ligand defects could actually be present for COK-47-based MOFs after ligand exchange and simply even out with excess ligands that are possibly capping the crystallites. The TGA results were again used to correct the cocatalyst loadings determined by TXRF that are shown in Figure 29b and c. If samples were not measured by TGA, ligand excess of 15 % was assumed for MOFs obtained by one-pot synthesis and 1 % for MOFs obtained by post-synthetic ligand exchange. While one-pot synthesis of Pt-functionalized COK-47 at 120°C resulted in Pt loadings slightly higher than the theoretical ones, ligand exchange with Pt ligand yielded a bit less Pt than calculated. The Ni loading after ligand exchange with Ni ligand in DMF was higher than the theoretical value, but a lot closer than for one-pot synthesis of Ni-functionalized COK-47. Ligand exchange with Ni ligand in water resulted in degradation or amorphization of the framework, visible by the disappearance of all XRD peaks, but this might rather be due to a failed synthesis than such a synthesis not being possible in general.

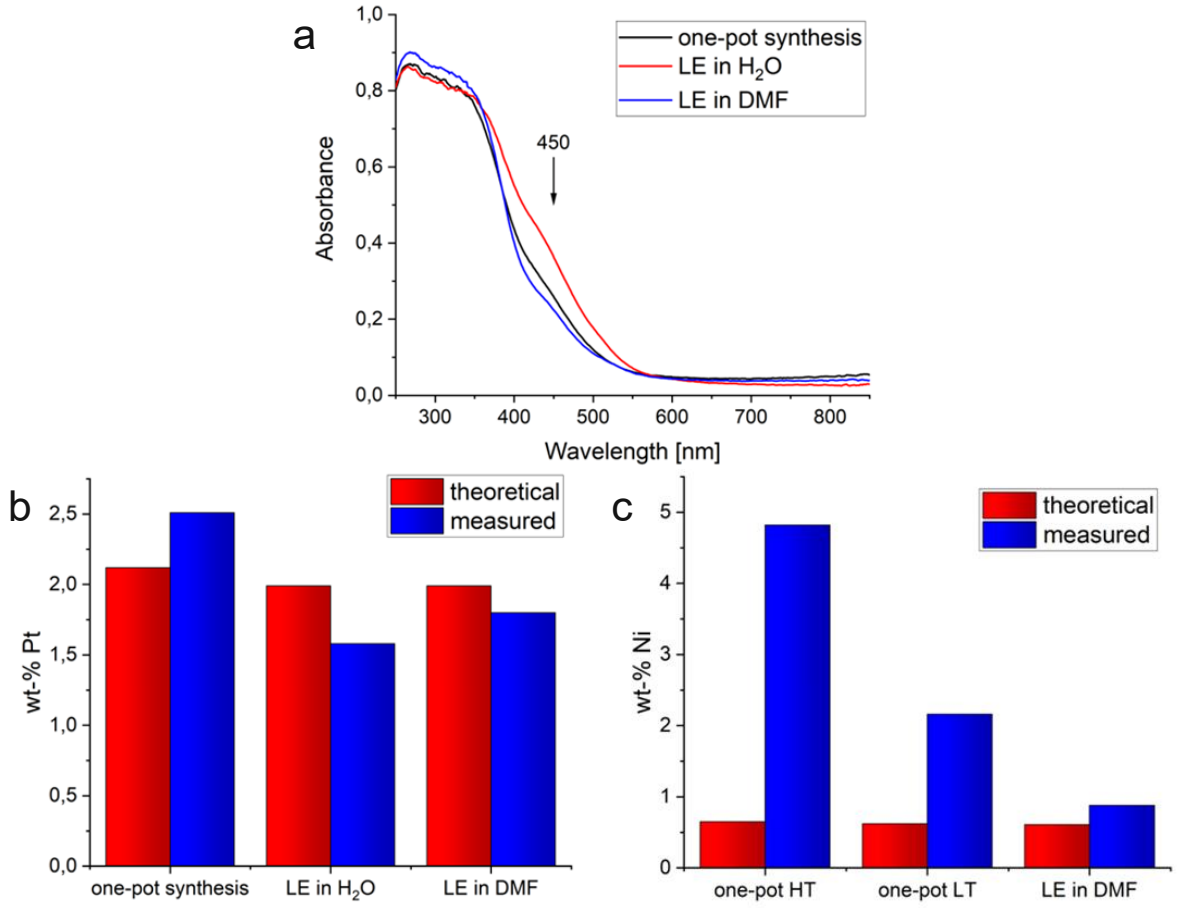

Figure 29: (a) UV/Vis DRS spectra of COK-47 with 4 % bpdc exchanged with Pt ligand, obtained either via one-pot synthesis at 120°C (COK-47-4Pt-2) or ligand exchange (LE, samples: COK-47-4Pt-LE-2, COK-47-4Pt-LE-3); (b) Pt loadings as measured by TXRF of the same samples (Ti content corrected by TGA) compared to the theoretical loadings corrected by TGA; (c) Ni loadings as measured by TXRF of COK-47 with 4 % bpdc exchanged with Ni ligand, obtained via one-pot synthesis at 150°C (HT, COK-47-4Ni) or 120°C (LT, COK-47-4Ni-2) or ligand exchange (LE, COK-47-4Ni-LE-3) where the Ti content was corrected by TGA compared to the theoretical loadings corrected by TGA

The functionalization of COK-47 with Ni single sites by ligand exchange did not result in any meaningful activity for photocatalytic hydrogen evolution, just as it has been the case for one-pot synthesis. Introducing Pt single sites by these means yielded HER activity as shown in Figure 30, but the amounts of formed hydrogen were lower than for a corresponding sample obtained by one-pot synthesis and the dark grey color after illumination due to charge carrier trapping was observed again. A potentially beneficial effect due to higher temperature during the MOF synthesis or preferential surface functionalization by ligand exchange and subsequent accessibility of the Pt sites could therefore not be observed. The used solvent for the ligand exchange procedure did not seem to have a strong effect on the catalytic activity.

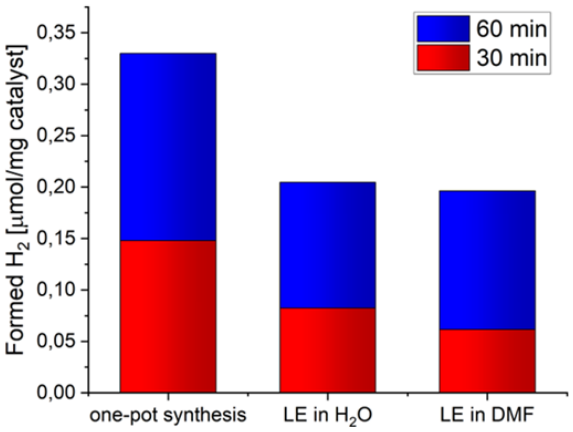

Figure 30: Amounts of formed H_2 after 30 and 60 min illumination for COK-47 with 4 % bpdc exchanged with Pt ligand, obtained either via one-pot synthesis (COK-47-4Pt-2) or ligand exchange (LE, samples: COK-47-4Pt-LE-2, COK-47-4Pt-LE-3)

6.3.2.1 Post-Synthetic Ligand Exchange with Porous COK-47

The importance of post-synthetic procedures to obtain certain single-site functionalized MOFs can be demonstrated by the version of COK-47, that Smolders et al. originally reported and called COK-47$_S$.[43] Their synthesis relies on a short reaction time of 15 min at a high temperature of 185°C. When functionalizing this material with Pt single sites, a one-pot synthesis at this temperature would lead to the formation of Pt nanoparticles. However, when synthesizing the pristine MOF and applying ligand exchange afterwards, this problem can be avoided. COK-47$_S$ has the potential to be beneficial for single-site catalysis, because the material is porous, other than the COK-47$_{ISO}$ that was mainly used for this thesis, which could enhance accessibility of the active sites for protons. Therefore, COK-47$_S$ was synthesized and functionalized with Pt ligand post-synthesis via ligand exchange in water. XRD diffractograms of COK-47$_{ISO}$ and COK-47$_S$ before and after ligand exchange are displayed in Figure 31a. Comparing pristine COK-47$_{ISO}$ of this thesis and COK-47$_S$, peaks at 6°, 12° and 18° appear for both, but COK-47$_S$ also shows a subtle reflection at 26° that remains after ligand exchange which has been ascribed to larger crystallite sizes parallel to the Ti sheets.[43] This peak was completely or almost absent for COK-47$_{ISO}$, besides for one batch (COK-47-1). This batch and COK-47$_S$ also showed more absorption of visible light and therefore a darker color, indicating a correlation between crystallite dimensions and electronic structure. Introduction of Pt ligand into COK-47$_S$ again led to a feature around 450 nm in UV/Vis DRS as can be seen in Figure 31b.

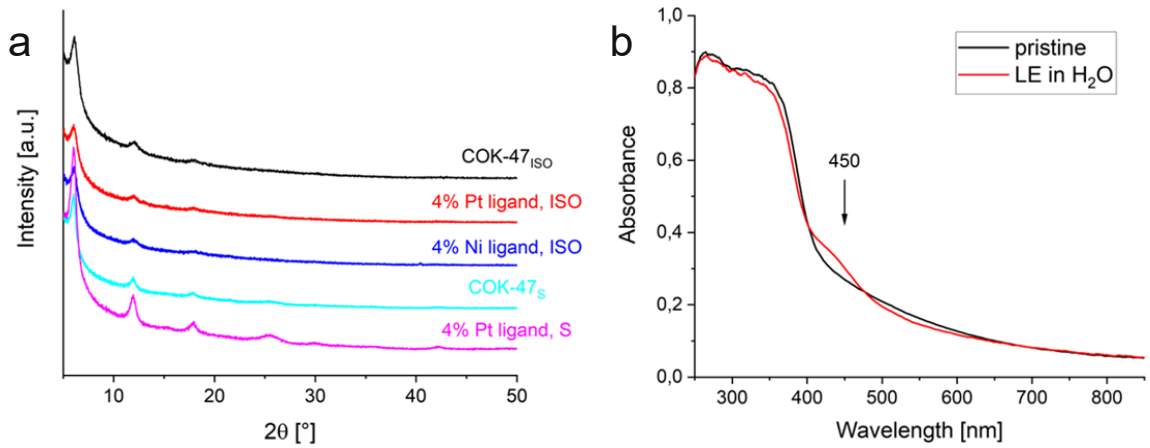

Figure 31: (a) XRD diffractograms of pristine COK-47$_{ISO}$ synthesized at 150°C (COK-47-7), COK-47$_{ISO}$ with 4 % bpdc exchanged with Pt ligand (COK-47-4Pt-LE-3) or Ni ligand (COK-47-4Ni-LE-3) via ligand exchange and COK-47$_S$ before (COK-47-S-1) and after (COK-47-S-4Pt-LE) ligand exchange with 4 % Pt ligand; (b) UV/Vis DRS spectra of COK-47$_S$ before (COK-47-S-1) and after (COK-47-S-4-Pt-LE) ligand exchange with 4 % Pt ligand

The photocatalytic activities of catalysts based on COK-47$_s$ are compared to COK-47$_{ISO}$ in Figure 32. While photodeposition of Pt onto pristine COK-47$_S$ showed lower HER activity than the same for COK-47$_{ISO}$, ligand exchange of COK-47$_S$ with Pt ligand yielded a better catalyst than COK-47$_{ISO}$ after the same procedure. This effect is further highlighted by the absence of a color change after illumination of Pt-functionalized COK-47$_S$, indicating that electrons were not trapped in the SBUs, but migrated to the Pt single sites where they reacted with protons. The use of COK-47$_S$ as a platform for Pt single sites did therefore turn out to be beneficial compared to COK-47$_{ISO}$, possibly because its porosity and therefore better accessibility of the active sites.

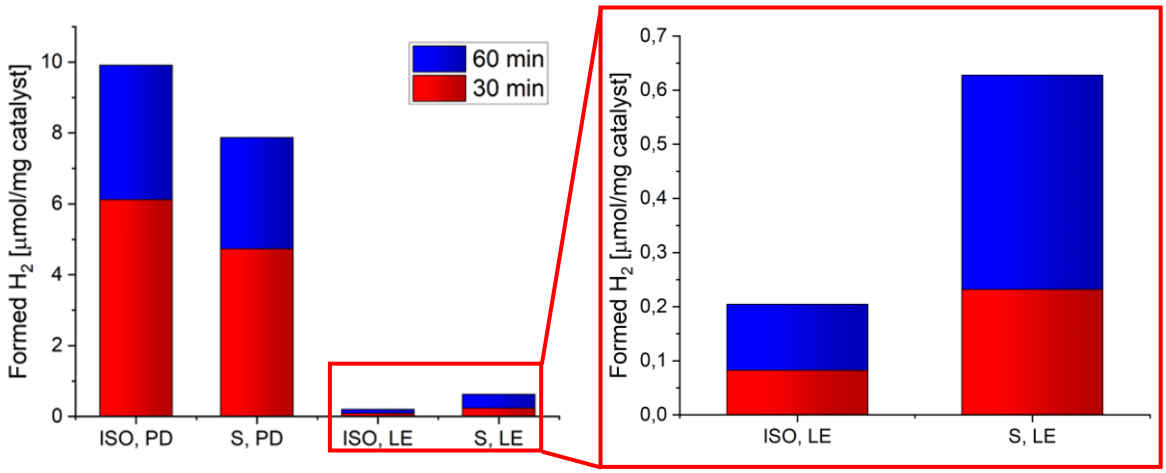

Figure 32: Amounts of formed H_2 after 30 and 60 min illumination for COK-47$_{ISO}$ and COK-47$_S$ with 2 wt-% Pt as cocatalyst, introduced either via photodeposition (PD, samples: mean of COK-47-5, COK-47-7 and COK-47-8, COK-47-S-1) or ligand exchange in H_2O (LE, samples: COK-47-4Pt-LE-2, COK-47-S-4Pt-LE)

7 Conclusions

Organometallic complexes of Pt and Ni with H_2bpydc as ligand were synthesized successfully and incorporated into the metal-organic frameworks UiO-67 and COK-47, either via direct one-pot synthesis or post-synthetic ligand exchange of the pristine MOF. The obtained hybrid materials were characterized with multiple techniques and tested on their activity for photocatalytic hydrogen production from water.

The successful synthesis of Pt ligand was proven by ^{1}H NMR and XPS. The characterization of Ni ligand was harder, as it was a paramagnetic complex, and even though the exact structure of the compound remains unclear (UV/Vis DRS suggests an octahedral rather than a tetrahedral complex) the formation of a dative bond between H_2bpydc and Ni is highly suggested by the combination of ^{1}H NMR and XPS results. The integrity of the carboxylic groups after complex formation was demonstrated by FTIR for both Pt ligand and Ni ligand.

The formation of a UiO-67-type framework was proven by XRD and FTIR. A reported metal-to ligand charge transfer of Pt ligand in the framework was confirmed by UV/Vis DRS and TGA showed a decrease of the thermal stability of UiO-67 after incorporation of Pt ligand or Ni ligand. Steady-state and time-resolved PL measurements indicated an electron transfer to the Pt or Ni single sites after photoexcitation, which resulted in excellent HER activity of the functionalized UiO-67-based materials. Single sites of Pt or Ni as cocatalyst outperformed their nanoparticle counterparts obtained by photodeposition, with Pt exhibiting better activity than Ni, but Ni single sites still being a promising cocatalyst considering the low cost. It turned out that exchanging only small portions of the original ligand with Pt ligand yielded an activity optimum at Pt loadings of approximately 0.25 wt-%, which was lower than what was even studied in previous works, where an increasing activity was observed for increasing Pt loading.[53] The HER activity of Ni-functionalized UiO-67 did not show a high dependency on the Ni loading. Combining Ni or Pt single sites with Pt photodeposition demonstrated that the single sites work as a reduction catalyst and competitive charge carrier extraction took place between the two species. Post-synthetic ligand exchange of UiO-67 led to the introduction of missing ligand defects as shown by TGA and electron trap states close to the conduction band (observed by UV/Vis DRS and PL) that facilitated radiative recombination of electron-hole pairs seen in PL. This reduced the HER activity of catalysts obtained by ligand exchange compared to one-pot synthesis. Even though water as a very polar solvent is expected to promote ligand exchange better, DMF also proved to incorporate functionalized ligands into the framework well as could be seen from the metal loadings determined by TXRF. In fact, samples prepared by ligand exchange of UiO-67 in DMF turned out to exhibit even higher

HER activities than samples synthesized in water, possibly because of limited water stability of the metalloligands.

For single-site-functionalized COK-47-based MOFs, the formation of the intended framework was proven by XRD and FTIR, while UV/Vis DRS showed a similar feature as for UiO-67 after the introduction of Pt ligand. In contrary to UiO-67, the thermal stability remained unchanged after incorporation of the metalloligands. The combination of COK-47 and Ni as cocatalyst turned out to be almost inactive for photocatalytic hydrogen production. The functionalization of COK-47 with Pt single sites was only possible by adapting the synthesis conditions for one-pot synthesis or by post-synthetic ligand exchange, as the original procedure at 150°C produced Pt nanoparticles. However, XRD measurements showed that the adapted synthesis at 120°C yielded MOFs with lower crystallinity or smaller particles which can reduce HER activity. Ligand exchange, on the other hand, probably introduced missing ligand defects that reduced activity like for UiO-67, just that they were likely compensated by ligands capping the COK-47 crystallites, as TGA of pristine COK-47 showed excess ligands in the structure. The HER activity of COK-47 containing Pt single sites was a lot lower than after photodeposition of Pt, highlighted by a reversible color change after illumination due to Ti^{3+} states, indicating trapped electrons that are unable to react with protons. One of the problems with single-site functionalization of the COK-47 version mainly used for this thesis was its lack of porosity. When Pt ligand was introduced into COK-47_S, a porous version of COK-47, the HER activity was significantly improved compared to the non-porous version.

Comparing the two utilized synthesis procedures, post-synthetic ligand exchange enables more MOF-cocatalyst combinations, as the functionalized ligands do not need to withstand the synthesis conditions of the MOF. However, the ligand exchange procedure also introduces missing ligand defects and electron trap states that lower the activity of obtained catalysts.

8 Outlook

The utilized characterization methods were not sufficient to determine the exact structure of Ni ligand. Single crystal growth was tried, but all attempts were unsuccessful. The application of other solvents and different growth conditions to obtain large enough crystals would be worthwhile for proper characterization. Mass spectrometry (MS) could also help to identify all present ligands, in case the molecular ion peak can be detected.

The effect of bulky functionalized ligands on the pore volume of MOFs and the accessibility of active sites was not studied during this thesis. BET analysis would show possible pore blockage and deepen the understanding of the correlation between the amount of exchanged linkers and catalytic activity. The energy levels of the MOF conduction band and electronic states of the cocatalyst could be determined by density-functional theory (DFT) calculations and explain the ability of cocatalysts to extract photoexcited electrons. In combination with OER experiments, the question whether Pt single sites on COK-47 act as oxidation or reduction catalyst could be clarified. DFT would also be useful to understand the thermodynamic driving force for ligand exchange with the applied metalloligands by calculating the charge on the carboxylic group´s oxygen atoms of both unfunctionalized and functionalized linkers.

The catalytic activity of UiO-67 was possibly decreased by missing ligand defects. Those were introduced by ligand exchange, but were also present after one-pot synthesis. Therefore, finding a method to prevent the formation of such defects or heal them post synthesis seems promising. In the case of COK-47, the synthesis conditions for the MOF can have a strong effect on porosity and particle size which are affecting the catalytic performance. The adapted one-pot synthesis procedure in this thesis only served the purpose of preventing nanoparticle formation, but adapting the synthesis to optimize activity could yield better catalysts. As Ni-functionalized ligands in COK-47 did not produce significant amounts of hydrogen, the utilization of other earth-abundant cocatalysts like Cu single sites on COK-47 becomes interesting as well. The conducted experiments on ligand exchange showed the importance of the solvent. Optimizing solvent and reaction time could significantly improve the catalytic activity by finding the ideal conditions for a sufficient ligand exchange rate, high stability of the organometallic complex and a small amount of introduced missing ligand defects. Lastly, stability under reaction conditions is a general issue for MOF-based catalysts, but was not studied at all during this thesis. Besides the stability of the framework, stability of the cocatalyst can be problematic as well for MOFs containing single-metal-sites due to leaching and subsequent nanoparticle formation.[54] The incorporation of additional bpydc linkers could offer a valuable tradeoff between activity and stability of such catalysts.

9 List of References

(1) *The Paris Agreement | UNFCCC*. https://unfccc.int/process-and-meetings/the-paris-agreement/the-paris-agreement (accessed 2022-10-03).

(2) Jackson, R. B.; Quéré, C. L.; Andrew, R. M.; Canadell, J. G.; Korsbakken, J. I.; Liu, Z.; Peters, G. P.; Zheng, B. Global Energy Growth Is Outpacing Decarbonization. *Environ. Res. Lett.* **2018**, *13* (12), 120401. https://doi.org/10.1088/1748-9326/aaf303.

(3) Kabir, E.; Kumar, P.; Kumar, S.; Adelodun, A. A.; Kim, K.-H. Solar Energy: Potential and Future Prospects. *Renewable and Sustainable Energy Reviews* **2018**, *82*, 894–900. https://doi.org/10.1016/j.rser.2017.09.094.

(4) Dutta, S. Review on Solar Hydrogen: Its Prospects and Limitations. *Energy Fuels* **2021**, *35* (15), 11613–11639. https://doi.org/10.1021/acs.energyfuels.1c00823.

(5) Howarth, R. W.; Jacobson, M. Z. How Green Is Blue Hydrogen? *Energy Science & Engineering* **2021**, *9* (10), 1676–1687. https://doi.org/10.1002/ese3.956.

(6) Fujishima, A.; Honda, K. Electrochemical Photolysis of Water at a Semiconductor Electrode. *Nature* **1972**, *238* (5358), 37–38. https://doi.org/10.1038/238037a0.

(7) Hyun Kim, J.; Hansora, D.; Sharma, P.; Jang, J.-W.; Sung Lee, J. Toward Practical Solar Hydrogen Production – an Artificial Photosynthetic Leaf-to-Farm Challenge. *Chemical Society Reviews* **2019**, *48* (7), 1908–1971. https://doi.org/10.1039/C8CS00699G.

(8) Qu, Y.; Duan, X. Progress, Challenge and Perspective of Heterogeneous Photocatalysts. *Chemical Society Reviews* **2013**, *42* (7), 2568–2580. https://doi.org/10.1039/C2CS35355E.

(9) Hisatomi, T.; Kubota, J.; Domen, K. Recent Advances in Semiconductors for Photocatalytic and Photoelectrochemical Water Splitting. *Chemical Society Reviews* **2014**, *43* (22), 7520–7535. https://doi.org/10.1039/C3CS60378D.

(10) Wang, Z.; Li, C.; Domen, K. Recent Developments in Heterogeneous Photocatalysts for Solar-Driven Overall Water Splitting. *Chemical Society Reviews* **2019**, *48* (7), 2109–2125. https://doi.org/10.1039/C8CS00542G.

(11) Ibhadon, A. O.; Fitzpatrick, P. Heterogeneous Photocatalysis: Recent Advances and Applications. *Catalysts* **2013**, *3* (1), 189–218. https://doi.org/10.3390/catal3010189.

(12) Nishiyama, H.; Yamada, T.; Nakabayashi, M.; Maehara, Y.; Yamaguchi, M.; Kuromiya, Y.; Nagatsuma, Y.; Tokudome, H.; Akiyama, S.; Watanabe, T.; Narushima, R.; Okunaka, S.; Shibata, N.; Takata, T.; Hisatomi, T.; Domen, K. Photocatalytic Solar Hydrogen Production from Water on a 100-M2 Scale. *Nature* **2021**, *598* (7880), 304–307. https://doi.org/10.1038/s41586-021-03907-3.

(13) Qin, D.-D.; Tang, Y.; Ma, G.; Qin, L.; Tao, C.-L.; Zhang, X.; Tang, Z. Molecular Metal Nanoclusters for ORR, HER and OER: Achievements, Opportunities and Challenges. *International Journal of Hydrogen Energy* **2021**, *46* (51), 25771–25781. https://doi.org/10.1016/j.ijhydene.2021.05.096.

(14) Chun, W.-J.; Ishikawa, A.; Fujisawa, H.; Takata, T.; Kondo, J. N.; Hara, M.; Kawai, M.; Matsumoto, Y.; Domen, K. Conduction and Valence Band Positions of Ta2O5, TaON, and Ta3N5 by UPS and Electrochemical Methods. *J. Phys. Chem. B* **2003**, *107* (8), 1798–1803. https://doi.org/10.1021/jp027593f.

(15) Hong Mak, C.; Han, X.; Du, M.; Kai, J.-J.; Fung Tsang, K.; Jia, G.; Cheng, K.-C.; Shen, H.-H.; Hsu, H.-Y. Heterogenization of Homogeneous Photocatalysts Utilizing Synthetic and Natural Support Materials. *Journal of Materials Chemistry A* **2021**, *9* (8), 4454–4504. https://doi.org/10.1039/D0TA08334H.

(16) Klahn, M.; Beweries, T. Organometallic Water Splitting – from Coordination Chemistry to Catalysis. *Reviews in Inorganic Chemistry* **2014**, *34* (3), 177–198. https://doi.org/10.1515/revic-2013-0019.

(17) Kärkäs, M. D.; Verho, O.; Johnston, E. V.; Åkermark, B. Artificial Photosynthesis: Molecular Systems for Catalytic Water Oxidation. *Chem. Rev.* **2014**, *114* (24), 11863–12001. https://doi.org/10.1021/cr400572f.

(18) Matheu, R.; Ertem, M. Z.; Gimbert-Suriñach, C.; Sala, X.; Llobet, A. Seven Coordinated Molecular Ruthenium–Water Oxidation Catalysts: A Coordination Chemistry Journey. *Chem. Rev.* **2019**, *119* (6), 3453–3471. https://doi.org/10.1021/acs.chemrev.8b00537.
(19) Pelletier, J. D. A.; Basset, J.-M. Catalysis by Design: Well-Defined Single-Site Heterogeneous Catalysts. *Acc. Chem. Res.* **2016**, *49* (4), 664–677. https://doi.org/10.1021/acs.accounts.5b00518.
(20) Wang, B.; Cai, H.; Shen, S. Single Metal Atom Photocatalysis. *Small Methods* **2019**, *3* (9), 1800447. https://doi.org/10.1002/smtd.201800447.
(21) Xing, J.; Chen, J. F.; Li, Y. H.; Yuan, W. T.; Zhou, Y.; Zheng, L. R.; Wang, H. F.; Hu, P.; Wang, Y.; Zhao, H. J.; Wang, Y.; Yang, H. G. Stable Isolated Metal Atoms as Active Sites for Photocatalytic Hydrogen Evolution. *Chemistry – A European Journal* **2014**, *20* (8), 2138–2144. https://doi.org/10.1002/chem.201303366.
(22) Cui, X.; Li, W.; Ryabchuk, P.; Junge, K.; Beller, M. Bridging Homogeneous and Heterogeneous Catalysis by Heterogeneous Single-Metal-Site Catalysts. *Nat Catal* **2018**, *1* (6), 385–397. https://doi.org/10.1038/s41929-018-0090-9.
(23) Yamashita, H.; Mori, K.; Kuwahara, Y.; Kamegawa, T.; Wen, M.; Verma, P.; Che, M. Single-Site and Nano-Confined Photocatalysts Designed in Porous Materials for Environmental Uses and Solar Fuels. *Chemical Society Reviews* **2018**, *47* (22), 8072–8096. https://doi.org/10.1039/C8CS00341F.
(24) Qian, Y.; Zhang, F.; Pang, H. A Review of MOFs and Their Composites-Based Photocatalysts: Synthesis and Applications. *Advanced Functional Materials* **2021**, *31* (37), 2104231. https://doi.org/10.1002/adfm.202104231.
(25) Li, Y.; Xu, H.; Ouyang, S.; Ye, J. Metal–Organic Frameworks for Photocatalysis. *Physical Chemistry Chemical Physics* **2016**, *18* (11), 7563–7572. https://doi.org/10.1039/C5CP05885F.
(26) Hong-Cai "Joe" Zhou; Kitagawa, S. Metal–Organic Frameworks (MOFs). *Chemical Society Reviews* **2014**, *43* (16), 5415–5418. https://doi.org/10.1039/C4CS90059F.
(27) Cheetham, A. K.; Kieslich, G.; Yeung, H. H.-M. Thermodynamic and Kinetic Effects in the Crystallization of Metal–Organic Frameworks. *Acc. Chem. Res.* **2018**, *51* (3), 659–667. https://doi.org/10.1021/acs.accounts.7b00497.
(28) Zhang, J.; Bai, T.; Huang, H.; Yu, M.-H.; Fan, X.; Chang, Z.; Bu, X.-H. Metal–Organic-Framework-Based Photocatalysts Optimized by Spatially Separated Cocatalysts for Overall Water Splitting. *Advanced Materials* **2020**, *32* (49), 2004747. https://doi.org/10.1002/adma.202004747.
(29) Zhao, W.; Li, G.; Tang, Z. Metal-Organic Frameworks as Emerging Platform for Supporting Isolated Single-Site Catalysts. *Nano Today* **2019**, *27*, 178–197. https://doi.org/10.1016/j.nantod.2019.05.007.
(30) Wen, M.; Mori, K.; Kuwahara, Y.; An, T.; Yamashita, H. Design of Single-Site Photocatalysts by Using Metal–Organic Frameworks as a Matrix. *Chemistry – An Asian Journal* **2018**, *13* (14), 1767–1779. https://doi.org/10.1002/asia.201800444.
(31) Zhang, H.; Wei, J.; Dong, J.; Liu, G.; Shi, L.; An, P.; Zhao, G.; Kong, J.; Wang, X.; Meng, X.; Zhang, J.; Ye, J. Efficient Visible-Light-Driven Carbon Dioxide Reduction by a Single-Atom Implanted Metal–Organic Framework. *Angewandte Chemie International Edition* **2016**, *55* (46), 14310–14314. https://doi.org/10.1002/anie.201608597.
(32) Zhang, Y.; Yang, X.; Zhou, H.-C. Synthesis of MOFs for Heterogeneous Catalysis via Linker Design. *Polyhedron* **2018**, *154*, 189–201. https://doi.org/10.1016/j.poly.2018.07.021.
(33) Carson, F.; Martínez-Castro, E.; Marcos, R.; Miera, G. G.; Jansson, K.; Zou, X.; Martín-Matute, B. Effect of the Functionalisation Route on a Zr-MOF with an Ir–NHC Complex for Catalysis. *Chem. Commun.* **2015**, *51* (54), 10864–10867. https://doi.org/10.1039/C5CC03934G.
(34) Dhakshinamoorthy, A.; Santiago-Portillo, A.; Asiri, A. M.; Garcia, H. Engineering UiO-66 Metal Organic Framework for Heterogeneous Catalysis. *ChemCatChem* **2019**, *11* (3), 899–923. https://doi.org/10.1002/cctc.201801452.

(35) Winarta, J.; Shan, B.; Mcintyre, S. M.; Ye, L.; Wang, C.; Liu, J.; Mu, B. A Decade of UiO-66 Research: A Historic Review of Dynamic Structure, Synthesis Mechanisms, and Characterization Techniques of an Archetypal Metal–Organic Framework. *Crystal Growth & Design* **2020**, *20* (2), 1347–1362. https://doi.org/10.1021/acs.cgd.9b00955.
(36) Feng, Y.; Chen, Q.; Jiang, M.; Yao, J. Tailoring the Properties of UiO-66 through Defect Engineering: A Review. *Ind. Eng. Chem. Res.* **2019**, *58* (38), 17646–17659. https://doi.org/10.1021/acs.iecr.9b03188.
(37) Fei, H.; Cohen, S. M. A Robust, Catalytic Metal–Organic Framework with Open 2,2′-Bipyridine Sites. *Chem. Commun.* **2014**, *50* (37), 4810–4812. https://doi.org/10.1039/C4CC01607F.
(38) Lee, S.; Bürgi, H.-B.; Alshmimri, S. A.; Yaghi, O. M. Impact of Disordered Guest–Framework Interactions on the Crystallography of Metal–Organic Frameworks. *J. Am. Chem. Soc.* **2018**, *140* (28), 8958–8964. https://doi.org/10.1021/jacs.8b05271.
(39) Abdul Mubarak, N. S.; Foo, K. Y.; Schneider, R.; Abdelhameed, R. M.; Sabar, S. The Chemistry of MIL-125 Based Materials: Structure, Synthesis, Modification Strategies and Photocatalytic Applications. *Journal of Environmental Chemical Engineering* **2022**, *10* (1), 106883. https://doi.org/10.1016/j.jece.2021.106883.
(40) Fu, Y.; Sun, D.; Chen, Y.; Huang, R.; Ding, Z.; Fu, X.; Li, Z. An Amine-Functionalized Titanium Metal–Organic Framework Photocatalyst with Visible-Light-Induced Activity for CO2 Reduction. *Angewandte Chemie International Edition* **2012**, *51* (14), 3364–3367. https://doi.org/10.1002/anie.201108357.
(41) Yan, Y.; Li, C.; Wu, Y.; Gao, J.; Zhang, Q. From Isolated Ti-Oxo Clusters to Infinite Ti-Oxo Chains and Sheets: Recent Advances in Photoactive Ti-Based MOFs. *Journal of Materials Chemistry A* **2020**, *8* (31), 15245–15270. https://doi.org/10.1039/D0TA03749D.
(42) Wang, S.; Kitao, T.; Guillou, N.; Wahiduzzaman, M.; Martineau-Corcos, C.; Nouar, F.; Tissot, A.; Binet, L.; Ramsahye, N.; Devautour-Vinot, S.; Kitagawa, S.; Seki, S.; Tsutsui, Y.; Briois, V.; Steunou, N.; Maurin, G.; Uemura, T.; Serre, C. A Phase Transformable Ultrastable Titanium-Carboxylate Framework for Photoconduction. *Nat Commun* **2018**, *9* (1), 1660. https://doi.org/10.1038/s41467-018-04034-w.
(43) Smolders, S.; Willhammar, T.; Krajnc, A.; Sentosun, K.; Wharmby, M. T.; Lomachenko, K. A.; Bals, S.; Mali, G.; Roeffaers, M. B. J.; De Vos, D. E.; Bueken, B. A Titanium(IV)-Based Metal–Organic Framework Featuring Defect-Rich Ti-O Sheets as an Oxidative Desulfurization Catalyst. *Angewandte Chemie* **2019**, *131* (27), 9258–9263. https://doi.org/10.1002/ange.201904347.
(44) Masoomi, M. Y.; Morsali, A.; Dhakshinamoorthy, A.; Garcia, H. Mixed-Metal MOFs: Unique Opportunities in Metal–Organic Framework (MOF) Functionality and Design. *Angewandte Chemie International Edition* **2019**, *58* (43), 15188–15205. https://doi.org/10.1002/anie.201902229.
(45) Stanley, P. M.; Haimerl, J.; Shustova, N. B.; Fischer, R. A.; Warnan, J. Merging Molecular Catalysts and Metal–Organic Frameworks for Photocatalytic Fuel Production. *Nat. Chem.* **2022**, *14* (12), 1342–1356. https://doi.org/10.1038/s41557-022-01093-x.
(46) Toyao, T.; Miyahara, K.; Fujiwaki, M.; Kim, T.-H.; Dohshi, S.; Horiuchi, Y.; Matsuoka, M. Immobilization of Cu Complex into Zr-Based MOF with Bipyridine Units for Heterogeneous Selective Oxidation. *J. Phys. Chem. C* **2015**, *119* (15), 8131–8137. https://doi.org/10.1021/jp512749y.
(47) Gonzalez, M. I.; Oktawiec, J.; Long, J. R. Ethylene Oligomerization in Metal–Organic Frameworks Bearing Nickel(Ii) 2,2'-Bipyridine Complexes. *Faraday Discussions* **2017**, *201*, 351–367. https://doi.org/10.1039/C7FD00061H.
(48) An, Y.; Liu, Y.; An, P.; Dong, J.; Xu, B.; Dai, Y.; Qin, X.; Zhang, X.; Whangbo, M.-H.; Huang, B. NiII Coordination to an Al-Based Metal–Organic Framework Made from 2-Aminoterephthalate for Photocatalytic Overall Water Splitting. *Angewandte Chemie International Edition* **2017**, *56* (11), 3036–3040. https://doi.org/10.1002/anie.201612423.
(49) Canivet, J.; Aguado, S.; Schuurman, Y.; Farrusseng, D. MOF-Supported Selective Ethylene Dimerization Single-Site Catalysts through One-Pot Postsynthetic Modification. *J. Am. Chem. Soc.* **2013**, *135* (11), 4195–4198. https://doi.org/10.1021/ja312120x.

(50) Zhang, X.; Llabrés i Xamena, F. X.; Corma, A. Gold(III) – Metal Organic Framework Bridges the Gap between Homogeneous and Heterogeneous Gold Catalysts. *Journal of Catalysis* **2009**, *265* (2), 155–160. https://doi.org/10.1016/j.jcat.2009.04.021.
(51) He, X.; Ding, Y.; Huang, Z.; Liu, M.; Chi, M.; Wu, Z.; Segre, C. U.; Song, C.; Wang, X.; Guo, X. Engineering a Self-Grown TiO2/Ti-MOF Heterojunction with Selectively Anchored High-Density Pt Single-Atomic Cocatalysts for Efficient Visible-Light-Driven Hydrogen Evolution. *Angewandte Chemie* **2023**, *135* (25), e202217439. https://doi.org/10.1002/ange.202217439.
(52) Deria, P.; E. Mondloch, J.; Karagiaridi, O.; Bury, W.; T. Hupp, J.; K. Farha, O. Beyond Post-Synthesis Modification: Evolution of Metal–Organic Frameworks via Building Block Replacement. *Chemical Society Reviews* **2014**, *43* (16), 5896–5912. https://doi.org/10.1039/C4CS00067F.
(53) Hou, C.-C.; Li, T.-T.; Cao, S.; Chen, Y.; Fu, W.-F. Incorporation of a [Ru(Dcbpy)(Bpy)2]2+ Photosensitizer and a Pt(Dcbpy)Cl2 Catalyst into Metal–Organic Frameworks for Photocatalytic Hydrogen Evolution from Aqueous Solution. *J. Mater. Chem. A* **2015**, *3* (19), 10386–10394. https://doi.org/10.1039/C5TA01135C.
(54) Kim, D.; Whang, D. R.; Park, S. Y. Self-Healing of Molecular Catalyst and Photosensitizer on Metal–Organic Framework: Robust Molecular System for Photocatalytic H2 Evolution from Water. *J. Am. Chem. Soc.* **2016**, *138* (28), 8698–8701. https://doi.org/10.1021/jacs.6b04552.
(55) Song, Y.; Li, Z.; Zhu, Y.; Feng, X.; Chen, J. S.; Kaufmann, M.; Wang, C.; Lin, W. Titanium Hydroxide Secondary Building Units in Metal–Organic Frameworks Catalyze Hydrogen Evolution under Visible Light. *J. Am. Chem. Soc.* **2019**, *141* (31), 12219–12223. https://doi.org/10.1021/jacs.9b05964.
(56) Kyogoku, K.; Yamada, C.; Suzuki, Y.; Nishiyama, S.; Fukumoto, K.; Yamamoto, H.; Indo, S.; Sano, M.; Miyake, T. Syntheses of Metal-Organic Framework Compounds Containing Ni-Bipyridyl Complex for Oligomerization of Ethylene. *Journal of the Japan Petroleum Institute* **2010**, *53* (5), 308–312. https://doi.org/10.1627/jpi.53.308.
(57) Kim, M.; F. Cahill, J.; Su, Y.; A. Prather, K.; M. Cohen, S. Postsynthetic Ligand Exchange as a Route to Functionalization of 'Inert' Metal–Organic Frameworks. *Chemical Science* **2012**, *3* (1), 126–130. https://doi.org/10.1039/C1SC00394A.
(58) Chambers, M. B.; Wang, X.; Elgrishi, N.; Hendon, C. H.; Walsh, A.; Bonnefoy, J.; Canivet, J.; Quadrelli, E. A.; Farrusseng, D.; Mellot-Draznieks, C.; Fontecave, M. Photocatalytic Carbon Dioxide Reduction with Rhodium-Based Catalysts in Solution and Heterogenized within Metal–Organic Frameworks. *ChemSusChem* **2015**, *8* (4), 603–608. https://doi.org/10.1002/cssc.201403345.
(59) Chen, X.-H.; Wei, Q.; Hong, J.-D.; Xu, R.; Zhou, T.-H. Bifunctional Metal–Organic Frameworks toward Photocatalytic CO2 Reduction by Post-Synthetic Ligand Exchange. *Rare Met.* **2019**, *38* (5), 413–419. https://doi.org/10.1007/s12598-019-01259-6.
(60) Deria, P.; Mondloch, J. E.; Tylianakis, E.; Ghosh, P.; Bury, W.; Snurr, R. Q.; Hupp, J. T.; Farha, O. K. Perfluoroalkane Functionalization of NU-1000 via Solvent-Assisted Ligand Incorporation: Synthesis and CO2 Adsorption Studies. *J. Am. Chem. Soc.* **2013**, *135* (45), 16801–16804. https://doi.org/10.1021/ja408959g.
(61) Stanley, P. M.; Su, A. Y.; Ramm, V.; Fink, P.; Kimna, C.; Lieleg, O.; Elsner, M.; Lercher, J. A.; Rieger, B.; Warnan, J.; Fischer, R. A. Photocatalytic CO2-to-Syngas Evolution with Molecular Catalyst Metal-Organic Framework Nanozymes. *Advanced Materials* **2023**, *35* (6), 2207380. https://doi.org/10.1002/adma.202207380.
(62) Ayala, P.; Naghdi, S.; Nandan, S. P.; Myakala, S. N.; Rath, J.; Saito, H.; Guggenberger, P.; Lakhanlal, L.; Kleitz, F.; Toroker, M. C.; Cherevan, A.; Eder, D. The Emergence of 2D Building Units in Metal-Organic Frameworks for Photocatalytic Hydrogen Evolution: A Case Study with COK-47. *Advanced Energy Materials n/a* (n/a), 2300961. https://doi.org/10.1002/aenm.202300961.
(63) Szeto, K. C.; Kongshaug, K. O.; Jakobsen, S.; Tilset, M.; Lillerud, K. P. Design, Synthesis and Characterization of a Pt–Gd Metal–Organic Framework Containing

Potentially Catalytically Active Sites. *Dalton Trans.* **2008**, No. 15, 2054–2060. https://doi.org/10.1039/B719766G.
(64) Prashanth, J.; Konakanchi, R.; Venkatram Reddy, B. Barrier Potentials, Molecular Structure, Force Filed Calculations and Quantum Chemical Studies of Some Bipyridine Di-Carboxylic Acids Using the Experimental and Theoretical Using (DFT, IVP) Approach. *Molecular Simulation* **2019**, *45* (16), 1353–1383. https://doi.org/10.1080/08927022.2019.1634807.
(65) DeCoste, J. B.; Peterson, G. W.; Jasuja, H.; Glover, T. G.; Huang, Y.; Walton, K. S. Stability and Degradation Mechanisms of Metal–Organic Frameworks Containing the Zr6O4(OH)4 Secondary Building Unit. *J. Mater. Chem. A* **2013**, *1* (18), 5642. https://doi.org/10.1039/c3ta10662d.
(66) Li, J.; E, Y.; Lian, L.; Ma, W. Visible Light Induced Dye-Sensitized Photocatalytic Hydrogen Production over Platinized TiO2 Derived from Decomposition of Platinum Complex Precursor. *International Journal of Hydrogen Energy* **2013**, *38* (25), 10746–10753. https://doi.org/10.1016/j.ijhydene.2013.02.121.
(67) Ozawa, H.; Haga, M.; Sakai, K. A Photo-Hydrogen-Evolving Molecular Device Driving Visible-Light-Induced EDTA-Reduction of Water into Molecular Hydrogen. *J. Am. Chem. Soc.* **2006**, *128* (15), 4926–4927. https://doi.org/10.1021/ja058087h.
(68) Liu, W.; Migdisov, A.; Williams-Jones, A. The Stability of Aqueous Nickel(II) Chloride Complexes in Hydrothermal Solutions: Results of UV–Visible Spectroscopic Experiments. *Geochimica et Cosmochimica Acta* **2012**, *94*, 276–290. https://doi.org/10.1016/j.gca.2012.04.055.
(69) Mikuriya, M.; Schumacher, M.; Kawano, C.; Akihara, T.; Ono, K.; Yoshioka, D.; Sakiyama, H.; Handa, M. Dinuclear Nickel(II) Pivalate with M-Aqua and Di-M-Pivalato Bridges Showing a Ferromagnetic Interaction. *ChemJMold* **2014**, *9* (2), 62–66. https://doi.org/10.19261/cjm.2014.09(2).09.
(70) *Nickel (Ni), Z=28, & Nickel Compounds*. https://xps-database.com/nickel-ni-z28-chemicals/ (accessed 2023-06-01).
(71) *Platinum | XPS Periodic Table - HU*. https://www.thermofisher.com/uk/en/home/materials-science/learning-center/periodic-table/transition-metal/platinum.html (accessed 2023-06-01).
(72) *X-ray Photoelectron Spectroscopy (XPS) Reference Pages*. http://www.xpsfitting.com/search/label/Platinum (accessed 2023-06-01).
(73) Chavan, S.; G. Vitillo, J.; Gianolio, D.; Zavorotynska, O.; Civalleri, B.; Jakobsen, S.; H. Nilsen, M.; Valenzano, L.; Lamberti, C.; Petter Lillerud, K.; Bordiga, S. H 2 Storage in Isostructural UiO-67 and UiO-66 MOFs. *Physical Chemistry Chemical Physics* **2012**, *14* (5), 1614–1626. https://doi.org/10.1039/C1CP23434J.
(74) Flage−Larsen, E.; Røyset, A.; Cavka, J. H.; Thorshaug, K. Band Gap Modulations in UiO Metal–Organic Frameworks. *J. Phys. Chem. C* **2013**, *117* (40), 20610–20616. https://doi.org/10.1021/jp405335q.
(75) Cao, C.-S.; Wang, J.; Yu, X.; Zhang, Y.; Zhu, L. Photodegradation of Seven Bisphenol Analogues by Bi5O7I/UiO-67 Heterojunction: Relationship between the Chemical Structures and Removal Efficiency. *Applied Catalysis B: Environmental* **2020**, *277*, 119222. https://doi.org/10.1016/j.apcatb.2020.119222.
(76) Makuła, P.; Pacia, M.; Macyk, W. How To Correctly Determine the Band Gap Energy of Modified Semiconductor Photocatalysts Based on UV–Vis Spectra. *J. Phys. Chem. Lett.* **2018**, *9* (23), 6814–6817. https://doi.org/10.1021/acs.jpclett.8b02892.
(77) Ling, K.; Ogle, M. M.; Flores, E.; Godoy, F.; Martí, A. A. Exploring the Photophysical Properties of UiO-67 MOF Doped with Rhenium Carbonyl Complexes. *Journal of Photochemistry and Photobiology* **2022**, *11*, 100127. https://doi.org/10.1016/j.jpap.2022.100127.
(78) Maza, W. A.; Morris, A. J. Photophysical Characterization of a Ruthenium(II) Tris(2,2′-Bipyridine)-Doped Zirconium UiO-67 Metal–Organic Framework. *J. Phys. Chem. C* **2014**, *118* (17), 8803–8817. https://doi.org/10.1021/jp501140r.

(79) Lakowicz, J. R.; Masters, B. R. *Principles of Fluorescence Spectroscopy*, 3rd ed.; Springer: Boston, MA, 2006.
(80) Haselmann, G. M.; Baumgartner, B.; Wang, J.; Wieland, K.; Gupta, T.; Herzig, C.; Limbeck, A.; Lendl, B.; Eder, D. In Situ Pt Photodeposition and Methanol Photooxidation on Pt/TiO2: Pt-Loading-Dependent Photocatalytic Reaction Pathways Studied by Liquid-Phase Infrared Spectroscopy. *ACS Catal.* **2020**, *10* (5), 2964–2977. https://doi.org/10.1021/acscatal.9b05588.
(81) Cebada, S.; Soto, E.; Mota, N.; García Fierro, J. L.; Navarro, R. M. Effect of Photodeposition Conditions on Ni–CdS Photocatalysts and Its Role in the Photoactivity for H2 Production from Ethanolic Solutions. *International Journal of Hydrogen Energy* **2020**, *45* (40), 20536–20548. https://doi.org/10.1016/j.ijhydene.2020.01.169.
(82) Kochev, S. Yu.; Bubnov, Y. N.; Abramchuk, S. S.; Antonova, O. Yu.; Valetsky, P. M.; Kabachii, Y. A. Photocatalytic Activity of CdS Nanocrystals Doped with Ni and Stabilized by Polymer Shell. *Mendeleev Communications* **2017**, *27* (3), 310–312. https://doi.org/10.1016/j.mencom.2017.05.032.
(83) S. Schubert, J.; Popovic, J.; M. Haselmann, G.; P. Nandan, S.; Wang, J.; Giesriegl, A.; S. Cherevan, A.; Eder, D. Immobilization of Co, Mn, Ni and Fe Oxide Co-Catalysts on TiO 2 for Photocatalytic Water Splitting Reactions. *Journal of Materials Chemistry A* **2019**, *7* (31), 18568–18579. https://doi.org/10.1039/C9TA05637H.
(84) Chaston, J. C. The Oxidation of the Platinum Metals. *Platinum Metals Review* **1975**, *19* (4), 135–140.
(85) Zhao, X.; Xu, M.; Song, X.; Liu, X.; Zhou, W.; Wang, H.; Huo, P. Tailored Linker Defects in UiO-67 with High Ligand-to-Metal Charge Transfer toward Efficient Photoreduction of CO2. *Inorg. Chem.* **2022**, *61* (3), 1765–1777. https://doi.org/10.1021/acs.inorgchem.1c03690.
(86) Mavukkandy, M.; Chakraborty, S.; Abbasi, T.; Abbasi, S. A. A Clean-Green Synthesis of Platinum Nanoparticles Utilizing a Pernicious Weed Lantana (Lantana Camara). **2016**, *9*, 84–90. https://doi.org/10.3844/ajeassp.2016.84.90.
(87) Taghizadeh, F. The Study of Structural and Magnetic Properties of NiO Nanoparticles. *Optics and Photonics Journal* **2016**, *6* (8B), 164–169. https://doi.org/10.4236/opj.2016.68B027.

Acknowledgements

First and foremost, I want to express my gratitude to Prof. Dominik Eder for giving me the opportunity to conduct my thesis in his research group. I am amazed by the working atmosphere he built there and consider him an excellent example for transparent leadership. I really appreciate how his creativity and endless pool of ideas helped me to leave every conversation with some new thoughts on my project.

I also want to thank Assistant Prof. Alexey Cherevan for guiding me through my thesis and always being available for any question I had. His passion for science as well as his ability to switch between being a strategic and efficient leader in meetings and a grounded and humorous colleague during coffee breaks were very inspiring.

I want to express my thanks to the AK Eder group as a whole. I sincerely appreciate all members both as competent scientists and great colleagues. I will always be grateful for the personal relationships I was able to form there. I especially want to highlight Pablo Ayala, who was usually my first contact for practical issues or problems in the lab and met them with his continuously patient and kind temper. He always found some time for me, openly shared his experiences with MOFs and photocatalytic HER and acquired many TXRF measurements for me. Stephen Myakala, who always has a smile on his face, thinks of his colleagues when coming across interesting literature and measured TGA for me, Jasmin Schubert, who acquired XPS spectra and helped me with their interpretation and Dr. Dogukan Apaydin, who recorded my NMR spectra. Thank you all so much!

Lastly, I want to thank my family for their unconditional love. I know that I would not be the person I am today without the exemplary upbringing of my parents and I will always be grateful for that. The emotional and financial support of my family means so much to me and only this even enabled me to conduct my studies. I consider myself a lucky man to get to know my girlfriend, Eszter Brhlik, three years ago. Her enthusiasm in life gives me so much inspiration and motivation and she has always been so loving and understanding, even when some working days happened to be longer than planned.

Appendix

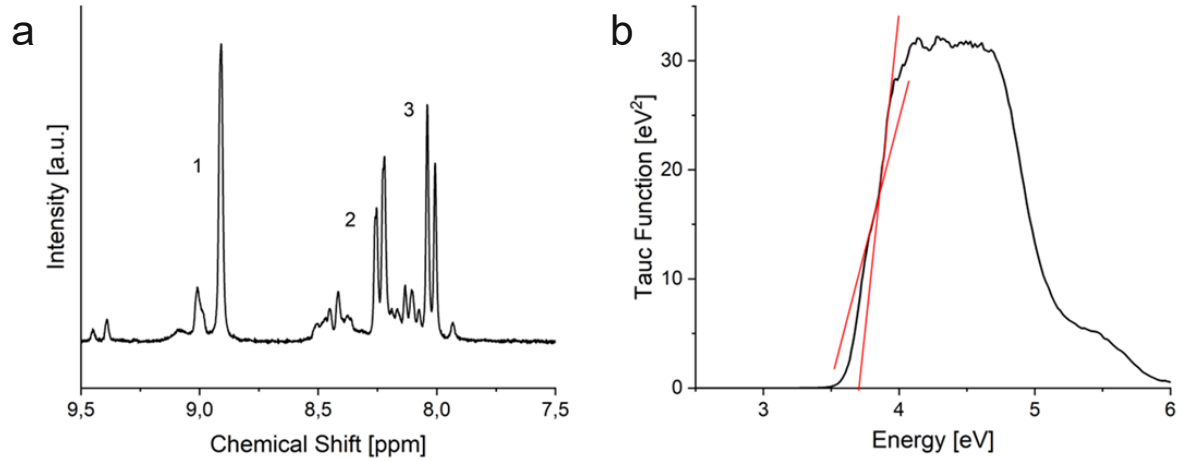

Figure 33: (a) ^{1}H NMR spectrum of a physical mixture of Pt ligand (Pt-bpydc-3) and non-functionalized bpydc^{2-}, (b) example of how to determine the band gap if absorption also occurs below the absorption edge; the band gap energy equals the energy where the two red lines intersect (sample: UiO-67-4Ni-LE-5)

Table 5: List of synthesized samples including synthesis details and performed characterization and tests

Sample Name	Synthesis Procedure	Synthesis Details	Charact. / Catalytic Tests	Remarks
Pt-bpydc-1	5.1.1.1		NMR, DRS, FTIR, XRD, XRF	Red-brown
Pt-bpydc-2	5.1.1.1		NMR, DRS, FTIR, XRD, XRF	Red-brown
Pt-bpydc-3	5.1.1.1		NMR, DRS, FTIR, XRD, XRF	Brown
Ni-bpydc-1	Literature [56]	1.53 mmol $NiCl_2$ 1.53 mmol H_2bpydc 110 mL abs. EtOH	NMR, DRS, FTIR	Green, H_2bpydc did not dissolve in EtOH at room temperature, product soluble after reaction (recovered by rotary evaporation)
Ni-bpydc-2	5.1.1.2	1.09 mmol $NiCl_2$	NMR, DRS, FTIR, XRD, XRF	Green
Ni-bpydc-3	5.1.1.2	1.69 mmol $NiCl_2$	NMR, DRS, FTIR, XRD, XRF	Green

Ni-bpydc-4	5.1.1.2	1.76 mmol $NiCl_2$	DRS, FTIR, XRD, XRF	Green
UiO-67-1	5.1.2.1		DRS, FTIR, XRD, PL, HER (no PD, 2% PD Pt, 0.3% PD Ni)	White
UiO-67-2	5.1.2.1		DRS, FTIR, XRD, HER (no PD, 1% PD Pt, 2% PD Pt, 0.3% PD Ni)	White
UiO-67-3	5.1.2.1		DRS, FTIR, XRD, HER (2% PD Pt)	White
UiO-67-4	5.1.2.1		DRS, FTIR, XRD, HER (2% PD Pt)	White, HER activity bad, DRS shows intra-band gap states
UiO-67-5	5.1.2.1		DRS, FTIR, XRD, TGA, HER (2% PD Pt)	White
UiO-67-0.2bpy	5.1.2.1	0.2 mol-% bpydc	DRS, FTIR, XRD, PL, HER (0.1% PD Pt)	White
UiO-67-0.5bpy	5.1.2.1	0.5 mol-% bpydc	DRS, FTIR, XRD, PL, HER (0.25% PD Pt)	White
UiO-67-1bpy	5.1.2.1	1 mol-% bpydc	DRS, FTIR, XRD, TGA, PL, HER (0.5% PD Pt, 0.15% PD Ni)	White, HER activity bad, DRS and PL show intra-band gap states
UiO-67-1bpy-2	5.1.2.1	1 mol-% bpydc	DRS, FTIR, PL, HER (0.5% PD Pt)	White

UiO-67-1bpy-3	5.1.2.1	1 mol-% bpydc	DRS, FTIR, XRD, PL, HER (0.5% PD Pt, 0.15% PD Ni)	White
UiO-67-2bpy	5.1.2.1	2 mol-% bpydc	DRS, FTIR, XRD, TGA, PL, HER (1% PD Pt, 0.3% PD Ni)	White
UiO-67-4bpy	5.1.2.1	4 mol-% bpydc	DRS, FTIR, XRD, TGA, PL, HER (2% PD Pt, 0.3% PD Ni, 0.6% PD Ni)	White
UiO-67-0.2Pt	5.1.2.1	0.2 mol-% Pt-bpydc-2	DRS, FTIR, XRD, TGA, PL, HER (no PD)	Light yellow, HER activity bad, PL shows intra-band gap states
UiO-67-0.2Pt-2	5.1.2.1	0.2 mol-% Pt-bpydc-3	DRS, FTIR, PL, HER (no PD)	Light yellow, HER activity bad, PL shows intra-band gap states
UiO-67-0.2Pt-3	5.1.2.1	0.2 mol-% Pt-bpydc-3	DRS, FTIR, XRD, XRF, PL, HER (no PD)	Light yellow
UiO-67-0.5Pt	5.1.2.1	0.5 mol-% Pt-bpydc-2	DRS, FTIR, XRD, XRF, TGA, PL, HER (no PD)	Light yellow
UiO-67-1Pt	5.1.2.1	1 mol-% Pt-bpydc-2	DRS, FTIR, XRD, XRF, PL, HER (no PD, 2% PD Pt)	Yellow
UiO-67-2Pt	5.1.2.1	2 mol-% Pt-bpydc-2	DRS, FTIR, XRD, XRF, PL, HER (no PD)	Yellow

UiO-67-4Pt	5.1.2.1	4 mol-% Pt-bpydc-2	DRS, FTIR, XRD, XRF, TGA, PL, Raman, HER (no PD)	Yellow
UiO-67-4Pt-LE	5.1.2.4	4 mol-% Pt-bpydc-2 Pristine: UiO-67-1 Reaction in H_2O Washing in DMF	DRS, FTIR, XRD, XRF, TGA, PL, HER (no PD)	Yellow
UiO-67-4Pt-LE-2	5.1.2.4	4 mol-% Pt-bpydc-2 Pristine: UiO-67-2 Reaction in H_2O Washing in DMF Dried before washing	DRS, FTIR, XRD	Yellow, XRD shows loss of crystallinity, FTIR signals broadened
UiO-67-4Pt-LE-3	5.1.2.4	4 mol-% Pt-bpydc-2 Pristine: UiO-67-4 Reaction in DMF Washing in DMF	DRS, FTIR, XRD	Yellow
UiO-67-4Pt-LE-4	5.1.2.4	4 mol-% Pt-bpydc-2 Pristine: UiO-67-4 Reaction in DMF Washing in DMF	DRS, FTIR, XRD, XRF, TGA, PL, HER (no PD)	Yellow
UiO-67-1Ni	5.1.2.1	1 mol-% Ni-bpydc-2	DRS, FTIR, XRD, XRF, PL, HER (no PD, 2% PD Pt)	White
UiO-67-2Ni	5.1.2.1	2 mol-% Ni-bpydc-3	DRS, FTIR, XRD, XRF, PL, HER (no PD)	White
UiO-67-4Ni	5.1.2.1	4 mol-% Ni-bpydc-3	DRS, FTIR, XRD, XRF, TGA, PL, HER (no PD, 2% PD Pt)	White

UiO-67-4Ni-LE	5.1.2.4	4 mol-% Ni-bpydc-3 Pristine: UiO-67-1 Reaction in H_2O Washing in DMF Dried before washing	DRS, FTIR, XRD, XRF, HER (no PD)	White, XRD shows loss of crystallinity, FTIR signals broadened
UiO-67-4Ni-LE-2	5.1.2.4	4 mol-% Ni-bpydc-3 Pristine: UiO-67-3 Reaction in H_2O Washing in DMSO	DRS, FTIR, XRD, HER (no PD)	White, XRD signals less intense, FTIR signals broadened
UiO-67-4Ni-LE-3	5.1.2.4	4 mol-% Ni-bpydc-3 Pristine: UiO-67-3 Reaction in H_2O Washing in DMF	DRS, FTIR, XRD, XRF, TGA, PL, HER (no PD)	White
UiO-67-4Ni-LE-4	5.1.2.4	4 mol-% Ni-bpydc-3 Pristine: UiO-67-4 Reaction in DMF Washing in DMF	DRS, FTIR, XRD	White
UiO-67-4Ni-LE-5	5.1.2.4	4 mol-% Ni-bpydc-3 Pristine: UiO-67-5 Reaction in DMF Washing in DMF	DRS, FTIR, XRD, XRF, TGA, PL, HER (no PD)	White
COK-47-1	5.1.2.2	1.0 mmol H_2bpdc 150°C, 1 h	DRS, FTIR, XRD, HER (2% PD Pt)	Yellow, XRD and HER activity more like COK-47$_S$, red shift of band gap in DRS
COK-47-2	5.1.2.2	1.0 mmol H_2bpdc 150°C, 1 h	DRS, FTIR, XRD, HER (2% PD Pt)	Light yellow
COK-47-3	5.1.2.2	1.0 mmol H_2bpdc 150°C, 1 h	DRS, FTIR, XRD, HER (2% PD Pt, 0.6% PD Ni)	Light yellow, XRD signals less intense
COK-47-4	5.1.2.2	0.5 mmol H_2bpdc 150°C, 1 h	DRS, FTIR, XRD, HER (2% PD Pt)	Yellow

COK-47-5	5.1.2.2	1.0 mmol H_2bpdc 150°C, 1 h	DRS, FTIR, XRD, TGA, HER (2% PD Pt)	Light yellow
COK-47-6	5.1.2.2	0.5 mmol H_2bpdc 120°C, 2 h	DRS, FTIR, XRD, TGA, HER (2% PD Pt)	Light yellow
COK-47-7	5.1.2.2	1.0 mmol H_2bpdc 150°C, 1 h	DRS, FTIR, XRD, HER (2% PD Pt)	Light yellow
COK-47-8	5.1.2.2	1.0 mmol H_2bpdc 150°C, 1 h	DRS, FTIR, XRD, HER (2% PD Pt)	Light yellow
COK-47-4bpy	5.1.2.2	1.0 mmol ligands 4 mol-% H_2bpydc 150°C, 1 h	DRS, FTIR, XRD, TGA, HER (2% PD Pt)	Yellow
COK-47-1Pt	5.1.2.2	1.0 mmol ligands 1 mol-% Pt-bpydc-2 150°C, 1 h	DRS, FTIR, XRD, XRF, HER (no PD)	Dark grey, XRD shows Pt nanoparticles
COK-47-2Pt	5.1.2.2	1.0 mmol ligands 2 mol-% Pt-bpydc-3 150°C, 1 h	DRS, FTIR, XRD, XRF, HER (no PD)	Dark grey, XRD shows Pt nanoparticles
COK-47-4Pt	5.1.2.2	1.0 mmol ligands 4 mol-% Pt-bpydc-3 150°C, 1 h	DRS, FTIR, XRD, XRF, Raman, HER (no PD)	Dark grey, XRD shows Pt nanoparticles
COK-47-1Pt-2	5.1.2.2	0.6 mmol ligands 1 mol-% Pt-bpydc-3 120°C, 2 h	DRS, FTIR, XRD, XRF, HER (no PD)	Light yellow
COK-47-2Pt-2	5.1.2.2	0.6 mmol ligands 2 mol-% Pt-bpydc-3 120°C, 2 h	DRS, FTIR, XRD, XRF, HER (no PD)	Light yellow
COK-47-4Pt-2	5.1.2.2	0.6 mmol ligands 4 mol-% Pt-bpydc-3 120°C, 2 h	DRS, FTIR, XRD, XRF, TGA, HER (no PD, 2% PD Pt)	Yellow
COK-47-4Pt-LE	5.1.2.4	4 mol-% Pt-bpydc-2 Pristine: COK-47-2 Reaction in H_2O Washing in DMSO	DRS, FTIR, XRD, HER (no PD)	Yellow-brown, XRD signals almost not present

COK-47-4Pt-LE-2	5.1.2.4	4 mol-% Pt-bpydc-2 Pristine: COK-47-1 Reaction in H_2O Washing in DMF	DRS, FTIR, XRD, XRF, HER (no PD)	Yellow
COK-47-4Pt-LE-3	5.1.2.4	4 mol-% Pt-bpydc-2 Pristine: COK-47-5 Reaction in DMF Washing in DMF	DRS, FTIR, XRD, XRF, TGA, HER (no PD)	Yellow
COK-47-1Ni	5.1.2.2	1.0 mmol ligands 1 mol-% Ni-bpydc-3 150°C, 1 h	DRS, FTIR, XRD	Light yellow
COK-47-2Ni	5.1.2.2	1.0 mmol ligands 2 mol-% Ni-bpydc-3 150°C, 1 h	DRS, FTIR, XRD, HER (no PD)	Light yellow
COK-47-4Ni	5.1.2.2	1.0 mmol ligands 4 mol-% Ni-bpydc-3 150°C, 1 h	DRS, FTIR, XRD, XRF, HER (no PD)	Yellow-green, TXRF shows too high loading
COK-47-4Ni-2	5.1.2.2	0.5 mmol ligands 4 mol-% Ni-bpydc-3 120°C, 2h	DRS, FTIR, XRD, XRF, TGA, HER (no PD, 2% PD Pt)	Light yellow
COK-47-4Ni-LE	5.1.2.4	4 mol-% Ni-bpydc-3 Pristine: COK-47-3 Reaction in H_2O Washing in DMSO	DRS, FTIR, XRD, HER (no PD)	Light yellow, XRD signals almost not present, FTIR signals broadened
COK-47-4Ni-LE-2	5.1.2.4	4 mol-% Ni-bpydc-3 Pristine: COK-47-7 Reaction in H_2O Washing in DMF	DRS, FTIR, XRD, HER (no PD)	Light yellow, XRD signals almost not present, FTIR signals broadened

COK-47-4Ni-LE-3	5.1.2.4	4 mol-% Ni-bpydc-3 Pristine: COK-47-8 Reaction in DMF Washing in DMF	DRS, FTIR, XRD, XRF, TGA, HER (no PD)	Light yellow
COK-47-S-1	5.1.2.3		DRS, FTIR, XRD, HER (2% PD Pt)	Yellow-brown
COK-47-S-2	5.1.2.3		DRS, FTIR, XRD, HER (2% PD Pt)	Yellow-brown
COK-47-S-4Pt-LE	5.1.2.4	4 mol-% Pt-bpydc-2 Pristine: COK-47-S-1 Reaction in H_2O Washing in DMF	DRS, FTIR, XRD, XRF, HER (no PD)	Yellow-brown